Experimental and numerical investigation on dynamic behavior of soft materials with emphasis on tissue simulant materials

DISSERTATION
to obtain the degree of Doctor
of Engineering

submitted by
M.Eng. Sam Aghayan

submitted to the School of Science and Technology
of the University of Siegen
Siegen 2022

Supervisor and first appraiser
Prof. Dr.-Ing. Kesrtin Weinberg
University of Siegen

Second appraiser
Prof. Dr.-Ing. Robert Brandt
University of Siegen

Date of the oral examination
15.12.2022

Abstract

Investigation on the dynamic behavior of soft materials from different kinds of resins to soft biological tissue simulants has became drastically important, due to their vast applications in different sections of industry and material science, particularly in biomedical applications. Such materials have been increasingly used recently for specific-designed biomedical purposes in areas like tissue simulant materials (collagen and agarose). One of the crucial aspect of investigation on these strain-rate dependent materials is related to the impact-induced behaviour. Each of these materials could illustrates different behavior when imposed to high-rate loading condition. In this thesis, two groups of soft materials are studied through experimental and numerical approaches. The investigation initiates with soft 3D printing resins known as standard and tough resins, and will continue as the main course of research on very soft tissue simulant material, known as agarose gel, with the focus on brain tissue simulant agarose. In both cases, the behavior of materials in impact-induced condition is investigated.

Two types of resins, namely a MMA-based resin and an ABS-based tough resin, are subjected to compression tests on a Split Hopkinson pressure bar to deduce their dynamic properties under high strain rate loading. Two Hopkinson bar setups are used, the first one is equipped with aluminum bars and the second one with PMMA bars. From the measured strain waves, dynamic elastic moduli at high strain rates are derived.

The majority of this dissertation presents the experimental and numerical investigations on the dynamic behavior of impact-induced cavitation in agarose gels. The drop tower test was used for the experiments, and agarose samples with three different concentrations similar to soft brain tissue were tested. The acceleration causing the bubble cavitation and the correlated bubble sizes were determined. Such quantitative measurements can be utilized to evaluate brain tissue injuries. In parallel, we present finite element simulations of the drop tower experiment. We model the complete test setup to validate the measurements and derive the relevant pressure fields with simplified models. The numerical solutions are shown to be in excellent agreement with the experimental results of bubble cavitation, enabling substantial simplifications in further investigations of soft tissue under dynamic loading. In addition, to track the volume and pressure variation of the acceleration-induced bubbles after impact, the "Fluid-filled cavity" method is applied in the finite element model, which corresponds well to the experimental outcomes. Our study gives insight into the mechanisms of bubble cavitation in soft tissue. Combined with the numerical simulation, it estimates how impact and pressure waves act and, for example, which areas of the head may be affected by cavitation that induces brain injuries.

Keywords: Split Hopkinson Pressure Bar (SHPB), 3D printing resin, PMMA SHPB, high-strain rate elastic modulus, soft tissue, agarose gel, cavitation, drop tower test, numerical simulation.

Zusammenfassung

Die Erforschung des dynamischen Verhaltens weicher Materialien, von verschiedenen Kunstharzen bis hin zu weichen biologischen Gewebeimmitaten, hat aufgrund ihrer umfangreichen Anwendungen in verschiedenen Bereichen der Industrie und der Materialwissenschaft, insbesondere in der Biomedizin, drastisch an Bedeutung gewonnen. Solche Materialien werden in letzter Zeit zunehmend für spezielle biomedizinische Zwecke verwendet, z. B. für Gewebeimmitate (Kollagen und Agarose). Einer der wichtigsten Aspekte bei der Untersuchung dieser dehnratenabhängigen Materialien ist das stoßinduzierte Verhalten. Jedes dieser Materialien kann ein unterschiedliches Verhalten zeigen, wenn es einer hohen Dehnrate ausgesetzt wird. In dieser Arbeit werden zwei Gruppen weicher Materialien durch experimentelle und numerische Ansätze untersucht. Die Untersuchung beginnt mit weichen 3D gedruckten Kunstharzen, die als Standard- und zähe Harze bekannt sind. Im weiteren Verlauf der Forschung wird ein sehr weiches Gewebeimmitat benutzt, das als Agarosegel bekannt ist. In beiden Fällen wird das Verhalten der Materialien bei stoßinduzierten Zuständen untersucht.

Zwei Arten von Harzen, ein Harz auf MMA-Basis und ein zähes Harz auf ABS-Basis, werden Druckversuchen auf einer Split-Hopkinson-Bar unterzogen, um ihre dynamischen Eigenschaften unter Belastung mit hoher Dehnsrate zu ermitteln. Es werden zwei verschiedene Hopkinson-Stabaufbauten verwendet, eine mit Aluminiumstäben und eine mit PMMA-Stäben. Aus den gemessenen Dehnungswellen werden die dynamischen elastischen Module bei hohen Dehnungsgeschwindigkeiten abgeleitet.

Der Hauptteil dieser Dissertation befasst sich mit den experimentellen und numerischen Untersuchungen zum dynamischen Verhalten der stoßinduzierten Kavitation in Agarosegelen. Ein Fallturmtest wurde mit drei verschiedenen konzentrierten Agaroseproben, die weichem Hirngewebe ähneln, durchgeführt. Es wurden die Beschleunigung, die die Kavitation der Blasen verursacht, und die damit verbundenen Blasengrößen bestimmt. Solche quantitativen Messungen können zur Bewertung von Hirngewebsverletzungen verwendet werden. Parallel dazu werden Finite-Elemente-Simulationen des Fallturmexperiments präsentiert. Der gesamte Versuchsaufbau wird modelliert, um die Messungen zu validieren. Zudem werden die relevanten Druckfelder mit vereinfachten Modellen hergeleitet. Die numerischen Lösungen stimmen hervorragend mit den experimentellen Ergebnissen der Blasenkavitation überein und ermöglichen wesentliche Vereinfachungen bei weiteren Untersuchungen von Weichgewebe unter dynamischer Belastung. Um die Volumen- und Druckschwankungen der beschleunigungsinduzierten Blasen nach dem Aufprall zu verfolgen wird im Finite-Elemente-Modell der so genannte "Fluid-filled cavity" Ansatz verwendet, der gut mit den experimentellen Ergebnissen übereinstimmt.

Diese Studie gibt Aufschluss über die Mechanismen der Kavitation von Blasen in Weichgewebe. In Verbindung mit numerischen Simulationen können die Wirkung von Aufprall- und Druckwellen erklärt werden. Es lassen sich beispielsweise Bereiche des Kopfes identifizieren die von der Kavitation betroffen sein können, welche Hirnverletzungen hervorruft.

Schlüsselwörter: Split Hopkinson Pressure Bar (SHPB), 3D-Druckharz, PMMA SHPB, Elastizitätsmodul mit hoher Dehnsrate, Weichgewebe, Agarosegel, Kavitation, Fallturmtest, Hohlraumdruck, numerische Simulation.

Acknowledgments

I would like to thank everyone who encouraged and helped me during this process from the begining to the final stage of my PhD. My special appreciation to Prof. Dr. Weinberg whom I had a chance to work with and learnt enormously under her supervision. I sincerely thank her for all the knowledge, helps and supports that I recieved. In addition I would like to thank Prof. Dr. Brandt for being the co-refere of my dissertation, Prof. Dr. Peter Kraemer and Prof. Dr. Tamara Reinicke for joining the thesis commitee.

I would like to also thank my fellow colleagues in the group for all the great advices, helps, cooperations and most of all, the friendly atmosphere. Furthermore, I would like to thank Dr. Nötzel for his helps and great suggestions for the required testing parts and instruments. I also appreciate the cooperation of Dr. Marvi Mashhadi, the DAAD visitor in our group, for the fruitful discussions and suggestions.

This work is dedicated to my parents and my sister, who always supported me throughout the whole time.

Contents

1 Introduction – Motivation

Investigation on the dynamic behavior of soft materials from different kinds of resins to soft biological tissue simulants has become drastically important, due to their vast applications in different parts of industry and material science, particularly in biomedical applications. One essential aspect of investigation on these strain-rate dependant materials is related to the impact-induced behavior. Each of these materials could illustrate different behavior when imposed to high-rate loading condition.

During this thesis, we study two groups of soft materials through experimental and numerical approaches. The investigation begins with soft 3D printing resins and will continue as the main course of research on very soft tissue simulant material, known as agarose gel, with the focus on brain tissue simulant agarose. In both cases, the behavior of materials in impact-induced concept is studied.

1.1 Soft 3D printing resins

3D printing, also called additive manufacturing is the construction of a three-dimensional object from a 3D model, including different approaches for material deposition, joining and soildification under the controled defined condition. As of 2019, the precision, repeatability, and material range of 3D printing have increased to the point that some 3D printing processes are considered viable as an industrial-production technology, which includes the advantage of producing very complex shapes or geometries, for instance hollow parts or parts with internal truss structures to reduce weight [1].

Basically polymers have been popular materials for printing, due to the ease of manufacturing and handling [2]. However, the progressive approach of using soft materials has lead to usage of various resin based materials, including plastics and thermoplastics in recent years. Particularly Stereolithography or "SLA" printing is the most common additive manufacturing, using ultraviolet (UV) laser [3], focusing on resin-based materials with wide range of properties such as high heat deflection temperature or impact resistance [4].

These polymeric resins are typical materials for additive manufacturing with a wide range of applications. While their static elastic properties are commonly determined in tension or bending tests, the behaviour of such materials under dynamic loading is mostly unclear. Because of the intrinsic viscosity of the polymeric materials, their

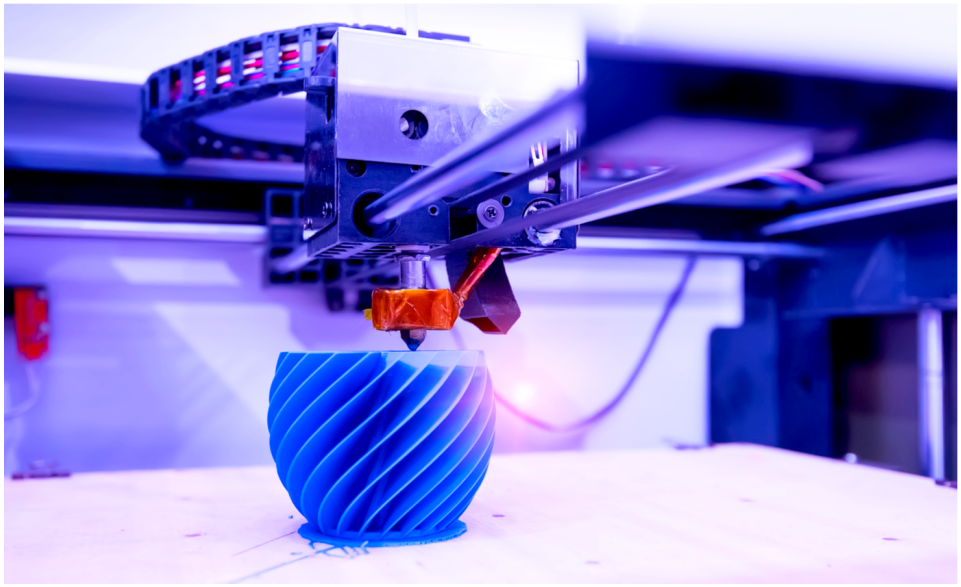

Figure 1.1: 3D printing, using soft resin [5]

response under high speed loading is much stiffer than under slow deformation. The vast applications of additively printed materials, particularly regarding prototyping, repairs and replacements [6, 7, 8, 9], but also high impact-resistant operations [10], encourage us to investigate this aspect more deeply. There have been previous investigations on the dynamic properties of resins in general [11, 12, 13, 14, 15], but only during recent years experiments on 3D printing resin-based materials have been reported [16, 17].

The Split Hopkinson Pressure Bar (SHPB) is a common experimental device to determine the dynamic material properties, mainly capable of subjecting the material to moderate and high strain rates [18, 19, 20, 21, 22, 23, 24, 25]. Because resins are soft materials with a rather high impedance, two SHPB setups are considered in this study. In the first setup, the split Hopkinson bar is equipped with classical aluminum bars and in the second setup the bars are made of PMMA material. With both SHPB setups we test and evaluate two thermoplastic polymers of additive manufacturing. in which we concentrate on thier dynamic elastic modulus in the end.

Elastic modulus describes the relative stiffness or rigidity of a material, which is measured by the slope of the elastic region of the stress-strain diagram. Moreover, it is a function of the whole sample rather than of a weak part or of the surface only [11]. The elastic modulus and other mechanical properties such as tensile strength, fracture toughness etc., are important in determining the resistance to flexural forces [11].

In order to evaluate the effect of the two different SHPB setups we simulate the experiment by means of a finite element analysis (FEA) with the commercial program Abaqus [26]. The main purpose of the simulation is to validate the strain wave propagation assumptions and to evaluate the corresponding wave signals. The FE model was built

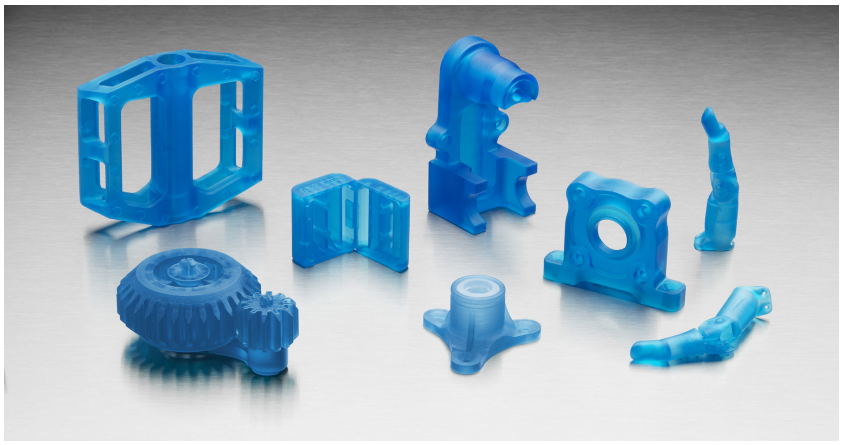

Figure 1.2: 3D printed prototypes using tough resin [5]

for the full SHPB arrangement with the actual geometrical shape and scale of the test components. Through the numerical simulation, the stress and strain wave propagation in bars are validated and compared to the experimental results for both aluminum and PMMA bars.

Here, the elastic modulus at high strain rates, typically referred to as dynamic elastic modulus in SHPB tests, of two printing resins are investigated. The two materials investigated are: a standard printing resin which is a white, methyl methacrylate (MMA) based plastic and a tough resin, thermoplastic resin which corresponds to acrylonitrile butadiene styrene (ABS).

1.2 Soft biological tissue simulant agarose

Knowing the material response of biological tissue under rapid loading is fundamental for understanding trauma and injuries of crash and impact. However, the mechanisms of injuries in collisions and the computational simulation of related accidents challenge both experimental and numerical research. Moreover, by its nature, the dynamic study of brain tissue or internal organs like liver and kidney is only possible to a limited extent. Therefore, soft gels, such as agarose or collagen are readily used for experiments, [27, 28, 29, 30, 31, 32, 33]. Accordingly, understanding the behavior of such soft gels is an essential step towards material modeling of soft biomaterials, which is why we study agarose as a brain-like material under shock loading here.

In a head injury due to impact, the human brain is strongly accelerated (or decelerated) and thus experiences a pressure wave loading. As a result, depending on the strength and duration of the impact, the brain tissue is rapidly deformed, particularly by volumetric expansion with the formation of pores or bubbles. This phenomenon, which is known as cavitation, is essentially responsible for damage to the tissue. Generally, the formation and activity of the bubble in the liquids is callled cavitation. The rapid

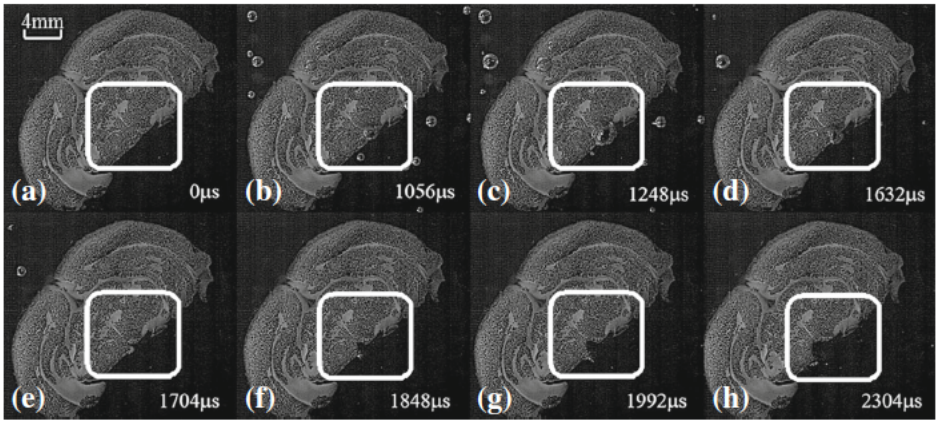

Figure 1.3: Effect of cavitation on a live rat brain tissue slice which was speckled and suspended in artificial cerebrospinal fluid. A simulated blast wave traveled from right to left. PSHPB testing showed bubble initiation (b), growth (b-d) and collapse (f). Cavitation-based damage with bubble collapse was observed in the hypothalamus region (box). The tissue tearing is observed well after bubble collapse (f-h). [27]

changes of pressure in a liquid results in the formation of these small vapor-filled cavities in the spots where the pressure is relatively low. It is well known that in the cavition areas the local pressure is less than the vapor pressure of the liquid. The study and investigation about the cavitaion phenomena has somehow long history, mainly due to the applications in the industrial subjects, e.g. cavitation in pumps or the cavitation effects on the propellers, leading to erosion of the rudder surface, increased noise levels and possible decreases in lift. The minimization of cavitation and erosion is still crucially important not only for propeller design of marine vessels but in many technical applications. In this study, we focus on cavitation dynamics, which is related to the brain tissue.

In particular, frontal impact of the head causes pressure waves and cavitation-induced injuries in the brain. The translational cranial motion leads to relative brain movements and a consequent rapid change in intracranial pressure, which results in a tensional stress state. There is a high potential for the resulting cavitating bubbles to grow and collapse within the cerebrospinal fluid or other fluid compartments within the brain. The cerebrospinal fluid carries dissolved gases which may trigger bubble cavitation [27] but cavitation induced damage is also known in other areas of in the cranium [34, 35].

Injuries to soft tissue resulting from cavitation can also be found in other types of loading. In addition to impact, explosions and associated strong pressure waves play a significant role in traumatic brain injuries [99, 37, 38, 39]. Apart from that, medical treatment and diagnostic techniques also have the potential to cause bubble formation inside a patient, raising the question of possible effects of cavitation on biological systems, e.g., in laser treatments for kidney stone removal [41, 42, 43]. Extracorporeal shock wave lithotripsy the destruction of calculi by focusing shock waves inside a patient, is known

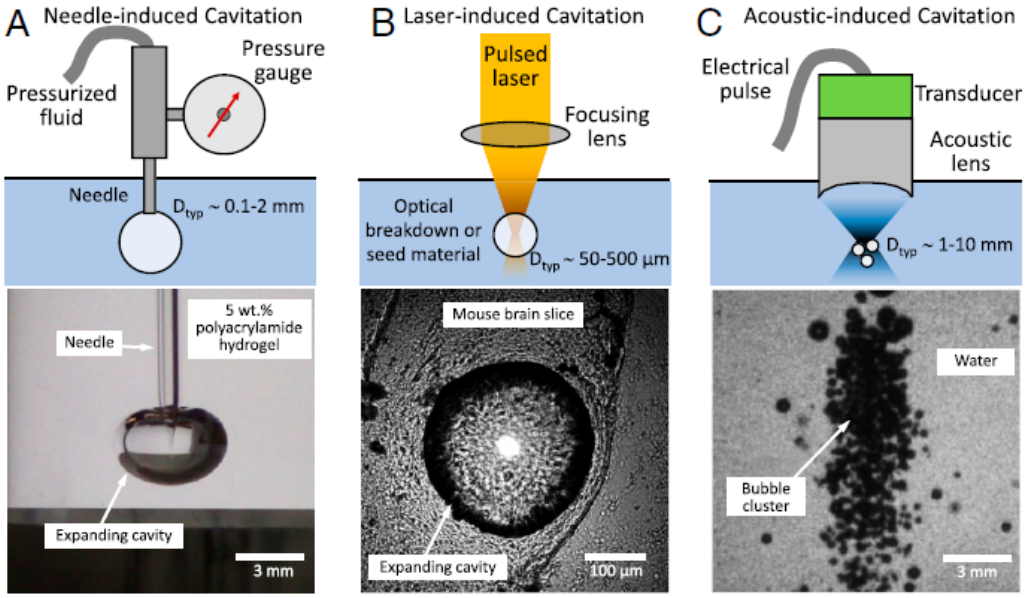

Figure 1.4: Schematic and image of cavity formation in (A) NIC, (B) LIC, and (C) AIC [40]

to be accompanied by cavitation [44]. In ultrasound imaging techniques the use of contrast agents lowers the threshold to create cavitation inside the blood vessels.The laser treatment for kidney stone removal and also optical cavitation may occur during laser surgery by plasma generation for instance in ophthalmology [45].

For mechanical studies of soft biological tissues, ballistic gelatin, agarose gel, or other types of biological hydrogels are commonly used. However, their deformation and damage mechanisms are not yet fully understood, mostly due to the complex coupling of fluid- and solid-like characteristics, their unstable nature [28, 46, 47, 48, 49], their nonlinear response [50, 51, 136, 53, 54], and their strain-rate-dependent material properties [55, 56]. Nevertheless, hydrogels are widely used for the experimental study of soft biomaterials, so their material behavior deserves special attention. We focus here on agarose gel which has a considerably wider range of stiffness than other gels like collagen. Generally, the stiffness of soft bio-materials covers a wide range, e.g., of 0.1 to 10 kPa for brain tissues [57, 58] or about 100 kPa for the human aorta [59]. Because of its concentration-dependent stiffness, agarose can easily be tuned to mimic such different target tissues [28].

Bubble cavitation in agarose gel is hardly optically visible; the bubbles are usually hardly a 1 mm in size and the time of bubble growth and collapse is usually in the μs range. Therefore, dynamic generation methods are needed to investigate the effect of cavitation. Mainly in the recent attempts, the shock wave was originated and progressed by laser light [29, 60] or electrical sparks [61]. Moreover, some groups use the sound field setups, known as acoustic cavitation [62, 63, 64]. Split Hopkinson bar tests have been used for dynamic impact tests to characterize compression materials for rates from 10^2

to $10^5 s^{-1}$, [27, 65]. Other methods such as torsional resonator testing [66], atomic force microscopy [67] and rheological-based testing [48] have been developed to ascertain the dynamic behavior of soft biological materials. Using such methods gives a good chance to test a wide range of soft fluidic and solid materials. However, the lack of the ability to impart high-rate loading and the direct observation of the tested samples during impact limits their potential for cavitation experiments. These considerations lead us to use drop tower tests, as also suggested in [28]. However, in opposite to [28], we use an (almost rigid) metallic cuvette holder and a lighter impactor so that the period of acceleration induced tension is smaller and more focused. Also, in our study there are no existing macro bubbles in samples, and our investigation on bubble behavior starts from nucleation observation.

Furthermore, the progression of the high-speed imaging techniques to capture the fast bubble dyanmics in various experimental setups played a vital role to study the dyanmic behaviour of bubbles, in the recent years [68, 69, 70, 71, 72].

In parallel to the experimental investigations, we perform finite element simulations to validate and support the experimental results. In order to do so, the commercial FEM programm Abaqus is used; all dynamic processes are computed with an implicit time-discretization. During the simulation, the whole test setup with the actual utilized geometrical shape and scales are modeled. Using the built FEM model, we validate the results related to acceleration and more importantly the pressure from the experimental approach.

It is essentially important to investigate the effects of cavitation in medical subjected areas and treatments to recognize the possible hazards. The study and research on the relation of the acceleration-induced cavitation from impact and the biological systems, and their interactions can be helpful to medicine, biology and biomedical applications. The quantitative measurements of this study regarding the acceleration induced pressure changes in agarose gel can be utilized for further development of brain injury investigations.

1.3 Outline of the thesis

In the following, the structure is clarified briefly by chapters:

In chapter 2, the concept of 3D printing and mainly the soft 3D printing resins are described. The basics of 3D printing incuding the employed techniques and types of 3D printings, mainly related to Stereolithograpy (SLA printers) are briefly discussed. In this chapter the usage of different resins in 3D printing is shortly explanied but More importantly we focuse on two types of soft resins of standard and tough resins produced and being used as 3D printing materials by Formlabs. During this chapter the properties and specifications related to MMA-based resin related to standard resin and then the characteristics of ABS-based resin related to tough resin are discussed. At the end of this chapter, we provide a good insight into biomechanical and mechanical applications of

these tested soft resins and their mechanical properties before digging into experimental approach to investigate the dyanmic stress-strain behavior of the mentioned 3D printing resins.

This chapter focuses fully on Split Hopkinson Pressure Bar (SHPB) test as the experimental method to investigate the dynamic behavior of soft resins. In this chapter the main concept of SHPB test is initially explained and the classical setup is described before we deeply concentrate on our own modified test setup, where we in the first section present the two different SHPB setups, using metalic and polymeric incident and transmitted bars and the reason of implementation of such approach, due to the acoustic impedance, which is also fully discussed in this section. In another section the prerequisites of SHPB testing are explained and one by one, we validate our experimental approach, based on one dimensional wave theory and the required parameters such as stress equilibrium and pulse shaping technique. In addition, regarding the PMMA bar setup the signal correction process is explained. The experimental results related to the dynamic stress-strain behavior of standard and tough resins are then indicated and discussed. The results are seperated into two groups of bar setups for metalic aluminum bar setup and polymeric PMMA bars. In parallel to the experiment, in order to evaluate the effect of the two different SHPB setups, we simulate the experiment by means of a finite element model (FEM) with the commercial program Abaqus. The main purpose of the simulation is to validate the strain wave propagation assumptions and to evaluate the corresponding wave signals. In the numerical simulation section, we fully address the total SHPB setup modeling and the parametric studies to validate the test outcome.

In continuation of investigation of the dynamic behavior of soft materials, we concentrate on softer materials mainly known as tissue simulant bio-materials. Chapter 4 concentrate on Soft tissue simulant material, specifically agarose gel, which we focus on as soft tissue simulant, due to its vast biomedical applications. During this chapter, the characteristics of brain tissue are briefly introduced and then brain injury related cavitation is fully described as the principal phenomena in our study, in which the dynamic behavior of soft tissue simulant material is being investigated under accelearion-induced cavitation. In fact, through the cavitation we study and investigate the dynamics of agarose gel response and bubble growth as one of the repercussions of head impact injuries. In a section, the usage of hydogels and the material properties and their implications in biomedical applicaitions are discussed and in next section the preparation process of the agarose gel specimens for the experiment are explained.

Bubble dynamics, including the theoretical background is fully described in this chapter. Since in this study we used the modification of Rayleigh-Plesset model, the background, developments and essential assumptions of the related models are discussed, and in the final step we present our own derivation of the model that we utilize later to deduce the pressure- radius gradient of bubble in the agarose gel samples, corresponding to three different concentration groups of samples.

In chapter 5 "Experimental investigation on cavitation", the full experimental approach regarding implementation of drop tower test is addressed. In the first section of this chapter, the experimental methods used for bubble dynamics, consisting of already-existing micro bubbles and nucleation of bubbles are described and then we focuse on our own drop tower test setup, the concept and mechanical characteristics of this particular experiment to address the way that how the indirect impact on the agarose gel samples are successfully leading us to a better cavitation bubble recording. At the end of this chapter, the cavitation results, including the bubble nucleation, growth and collpase (in frame pictures), amplitude and critical accelerations corresponding to bubble cavitaion and the pressure of the bubble site derived from theoretical-experiment data are represented.

Chapter 6 focuses on the numerical investigation of cavitation test and pressure gradient of bubbles. In parallel to the experiment, FEM in Abaqus is implemented to model the whole drop tower test, which is fully addressed in the first section of the chapter. The detailed simulation of the experiment, including the mild steel made cuvette holder, agarose gel samples and rubber sheet modeling is illustrated and the validation of measured acceleration during the test is done in Abaqus program, which is later used as input to the subtracted model to investigate the pressure profile of the cavitation site.

In this chapter, "fluid cavity pressure" method is applied in FEM to more precisely address the bubble pressure and the corresponding volume gradient of the bubble in order to compare the FEM results with experimental outcome. At the end of the chapter the results are discussed and the conclusion regarding the experimental and numerical approach of this study is presented.

2 Experimental and numerical investigation on dynamic behavior of soft 3D printing resins

This chapter concentrates on the soft 3D printing resins and the experimental and numerical investigation on the dynamic behavior of two specific types of resins. Essential parts of this chapter are already published by us, in [73].

2.1 3D printing resins

Resins has always been popular material for 3D printing and basically one of the initial materials, used for additive manufacturing. The various physical and mechanical properties of resins, beside the simple handling and usage casued the vast consumption of resins in multiple areas. Nowdays, different types of resins including soft resins have vast applications in industry.

In polymer chemistry and materials science, resin is a solid or highly viscous substance of plant or synthetic origin that is typically convertible into polymers [74]. The mejority of the resins used as indutrial material, such as printing, are polymeric based resins with different characteristics. Polymer resin is similar to the industrial counterpart of naturally-occurring plant resins. Polymer resin starts out as a thick and sticky fluid that hardens permanently when left out in the open air for a certain period of time. They are usually produced by soaping organic compounds like thermosetting plastics. Companies that manufacture thermoplastics can make use of substances like methyl methacrylate, which behaves like a casting sort of resin in its liquid state. Once the methyl methacrylate goes through a polymerization process, it then sets into a hard, solid form. The finished product is sometimes used as a kind of acrylic glass [75].

The 3D printing techniques and various resourcing materials for microreactor applications are grouped mostly into two categories. One is light-induced process and photo-curable materials, and the other is heat- induced process and thermosoftening resins and metals [76]. Light-induced process and photo-curable include three types of 3D printing: Stereolithograpy apparatus (SLA), digital light projection (DLP), and

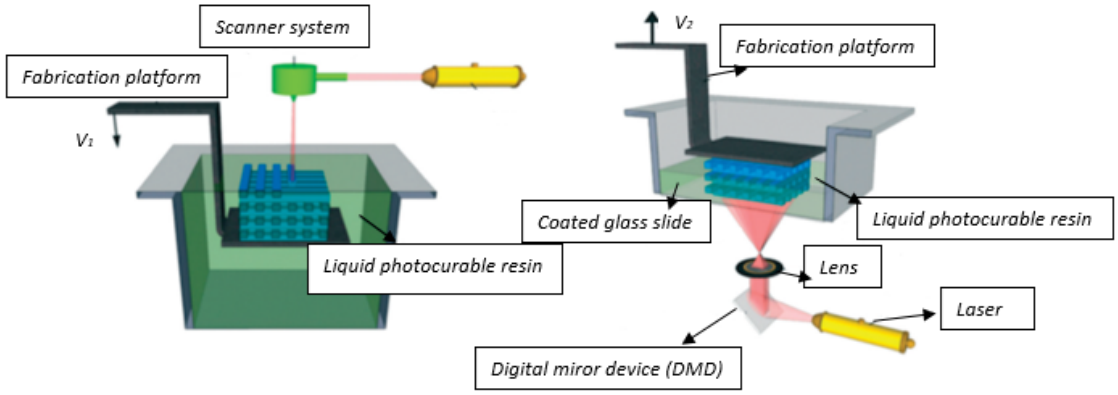

Figure 2.1: Consecpt of SLA-designed 3D printers (adapted from [76])

multiple jet modeling (MJM), utilize ultraviolet (UV) lights and photo-curable resins with low viscosity to build three-dimensional structures [76].

Stereolithography (SLA) 3D printing is the most common resin 3D printing process that has become vastly popular for its ability to produce high-accuracy, isotropic, and watertight prototypes and end-use parts in a range of advanced materials with fine features and smooth surface finish [5]. It belongs to the family of additive manufacturing technologies known as vat photopolymerization, commonly known as "resin 3D printing". The SLA printers use a focused laser beam or light-emitting diode (LED) lights to construct the object [76], see Figure 2.1. In this concept, the spot size of the laser beam and the absorption spectra of pgoto-curable resins play important role. The highest resolution is almost 27 x 27 x 0.25 (x, y, z axis) micrometers [77]. Alternatively, two-photon absorption SLA lithography (TPA-SLA) with infrared femtosecond laser (780 nm wavelength) can fabricate 3D structures a few hundreds of nanometers in size, offering the highest resolution out of available 3D printing techniques [78].

Specifically, the resins are mixed with photo-initiators to form radicals or cations upon exposure to a UV light. These photo-initiators often have phenone groups or phosphine oxide groups [76]. In addition, in order to control the curing depth, absorbers or organic dyes are sometimes added to the resins. The usage of conventional photoresist such as SU-8 is common but it requires a few minutes to solidify more than tens of micrometers of curing depth, while 3D printing resins demand faster curing kinetics due to the shorter light exposure time of several seconds to cure the desired layer a few tens of micrometers deep [76].

Different types of thermoplastic resins are used for SLA 3D printing, such as polylactic acid (PLA), polyethylene terephthalate (PET), acrylonitrilebutadiene styrene (ABS), methyl methacrylate (MMA) and etc. In this study, two type of soft resins, namely a MMA-based resin, known as standard resin, and an ABS-based tough resin, are subjected

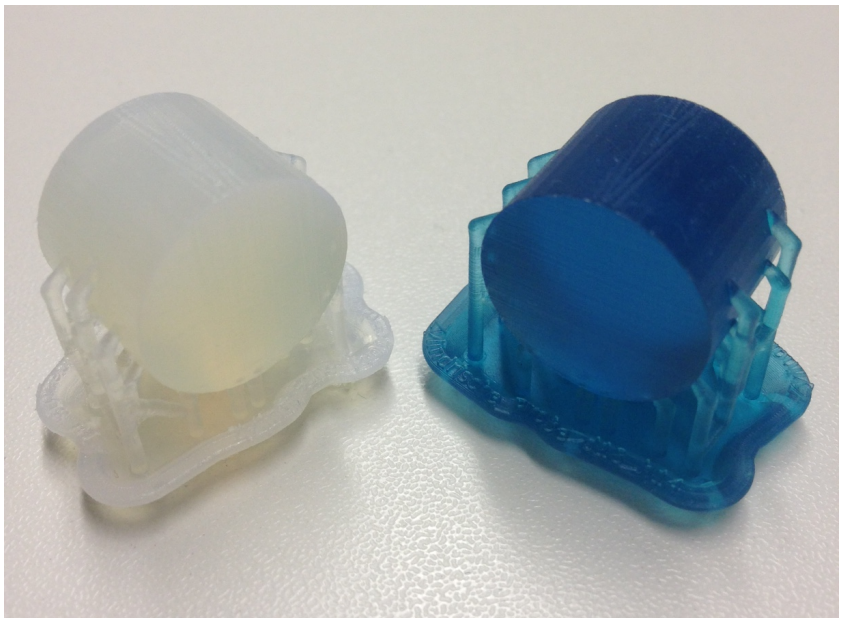

Figure 2.2: TR and SR resins samples after 3D printing

for experimental and numerical investigation for their dynamic behavior.

2.1.1 Standard MMA-based resin

White standard resin (SR) is Neutral, matte tone and represents slight translucency when thin [5]. This resin is a thermoplastic, mainly constists of MMA plastic. MMA is an organic compound, and coulorless liqiud, whch is a monomer used for the production of poly-methyl methacrylate (PMMA) [79]. In standard resins such MMA acts more as adhesives and hardener. They contain rubber and also additive strengthening agents, which have the ability of fast-cure process at room temperature and they are resistant to shear and impact stress. Mechanical properties of SR resin are shown in Table 2.1.

2.1.2 Tough ABS-based resin

Tough resin (TR) is basically designed for prototyping string sturdy parts and is greatly resistant to bending [5]. As the name stands, also huge strength toward impact, which makes this resin a suitable choice for dynamic applications, having the need to handle the impact, compression and stretching [5]. TR resin is ABS- based (Acrylonitrile butadiene styrene), with some flexibility and a comparatively high fracture resistance. ABS is a thermoplastic polymer made by polymerizing styrene and acrylonitrile. The polybutadiene, a rubbery substance, provides toughness and ductility at low temperatures, at the cost of heat resistance and rigidity [80].

Toughness refers to a material's ability to absorb energy before fracturing. When a tough material yields, it will undergo some deformation rather than just shattering.Toughness is also defined as the area under a stress-strain curve. Tough materials generally represent a good balance of strength and ductility. Hence, the area under a tough material's stress-strain curve is much larger than that of a very strong material with low elongation and this has a direct correlation to the amount of energy each material can absorb before failure [5].

ABS provides some mechanical properties related to impact resistance, toughness and also rigidity with respect to other common polymers [80]. The impact resistance property of TR resin can be improved by different modification related to increasing the portion of polybutadiene with respect to two other components. In addition, the toughness and stabilty under limited load is good and changing the portion of each component would turn this resin prepared for diffferent applications and various defined grades. Mechanical properties of TR resin are shown in Table 2.1.

There have been only a few experimental and numerical investigations on the dynamic properties of 3D printed resin based materials, hence rare results regarding dynamic properties of these special resins are available. Therefore, the aim of the current study is to investigate stress-strain behavior and dynamic elastic modulus of the tested resins.

2.2 Split Hopkinson Pressure Bar test (SHPB)

SHPB is a common experiment to determine the dynamic properties of the material for the impact simulated conditions in the dynamic loading regimes cf. [81, 82, 83] introduced by John Hopkinson, later modified by his son Bertram, Herbert Kolsky and others [18, 23]. SHPB experiments are mainly capable of subjecting the material to moderate and high strain rates. The traditional SHPB consists of a gas gun, which open the process by launching the striker, an incident and transmission bar and also a data acquisition system to collect and transfer the required data. The specimen is

resin type	basis polymer	tensile modulus [GPa]	flexural modulus [GPa]	notched IZOD [N/m]	remark
white standard resin (SR)	MMA	2.8	2.2	25	high surface and dimensional quality
blueish tough resin (TR)	ABS	2.7	1.16	51	sturdy prototyping high durability

Table 2.1: Properties of the investigated 3D printing materials [5]

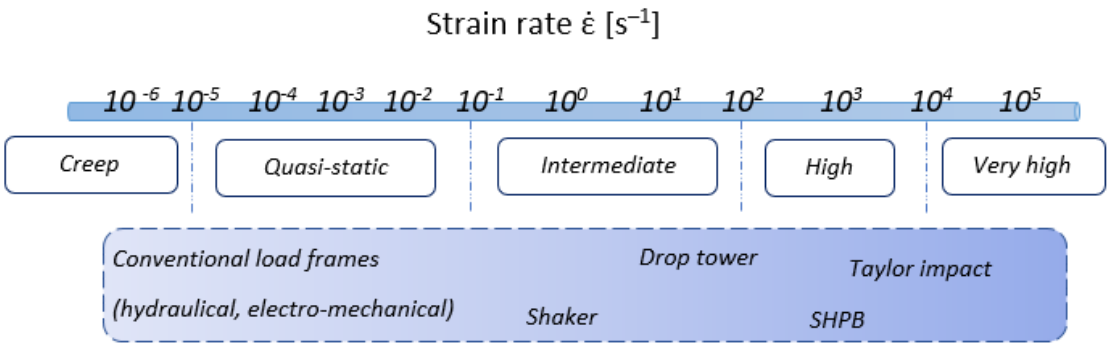

Figure 2.3: Low to very high strain rates and relevant experimental approaches

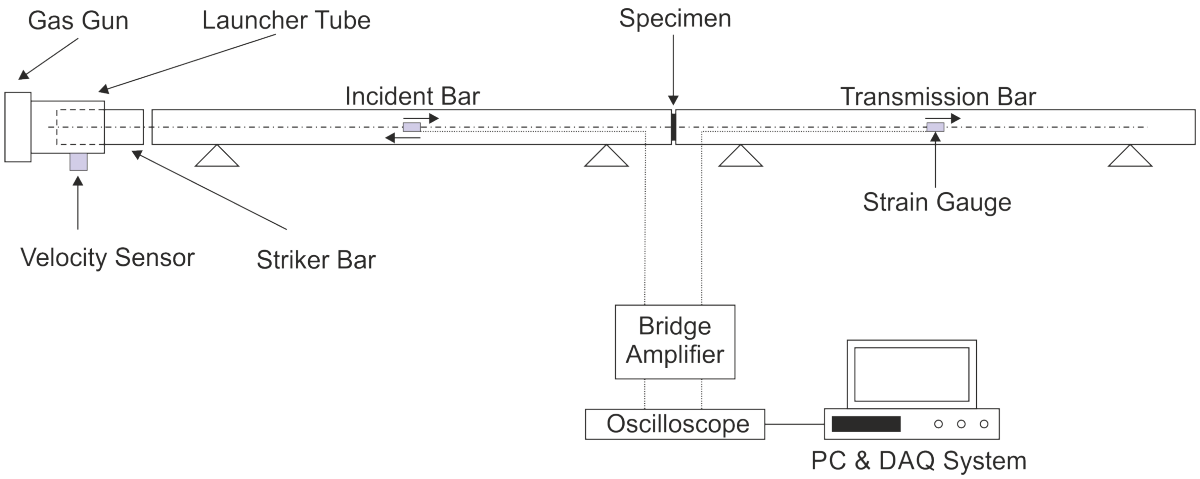

Figure 2.4: Split Hopkinson Pressure bar setup used for the compression tests

placed between the bars. When the striker hits the incident bar, a compressive pulse is generated and at the bar-specimen interface the wave splits, a part is reflected and a part continues to propagate through the specimen and the transmission bar, Figure 2.4.

The impact of the striker would intiate a compressive wave in the striker as well, which is reflected as tension wave back at the free end, then transimtted through the incident bar as an unloading wave. Similarly, a part of this unloading wave transmits into the tranmission bar and a part is reflected back, while the specimen is unloaded. Here, the loading duration T, produced in the experiment can be evaluated by striker length l [19],

$$T = \frac{2l}{C_{st}} \tag{2.1}$$

Where C_{st} is the elastic wave speed of the striker material. In our experiment, the striker has the same material as the incident and tranmission bar, with the same cross section area with the bars.

In this study, two experimental setups are considered for the SHPB test. At the first setup, the Split Hopkinson Bar being used is equipped with an aluminum incident and a transmission bar of 20mm diameter and 1800mm length each and for the second SHPB setup the bars are modified by using PMMA material in order to investigate and compare the wave propagation in the tested resins, Figure 2.6 .

A laser alignment technique is used for the calibaration of the SHPB system. The adjustment of the bars play essential role to obtain precise results. In the absence of the appropriate bar alignment the captured waves would be highly oscilated and could lead to wave dispersion. The laser system consists of a laser bore scope, a detailed machined sleeve that can hold the laser and target point on the center of the bearing holes. The centerline of the sleeve and the laser is aligned with the axis of the bars. The targets with the same diameter as the bars are fit to the linear bearings in blocks. The blocks are precisely adjusted so that the laser beam passes through all pinholes on the targets [19].

2.2.1 Acoustic impedance

In SHPB test, The pulses are determined by the materials' susceptibility to wave propagation. one of the essental elements of susceptibility to wave propagation is related to acoustic impedances $z = A\rho c$ where A, ρ, are cross section and material density, respectively, and c is the wave speed.

At the interface of two material the corresponding wave portions are [19]

$$\sigma_T = \frac{2\,z_2}{z_1 + z_2}\frac{A_1}{A_2}\sigma_I\,, \qquad \sigma_R = \frac{z_2 - z_1}{z_1 + z_2}\sigma_I\,. \tag{2.2}$$

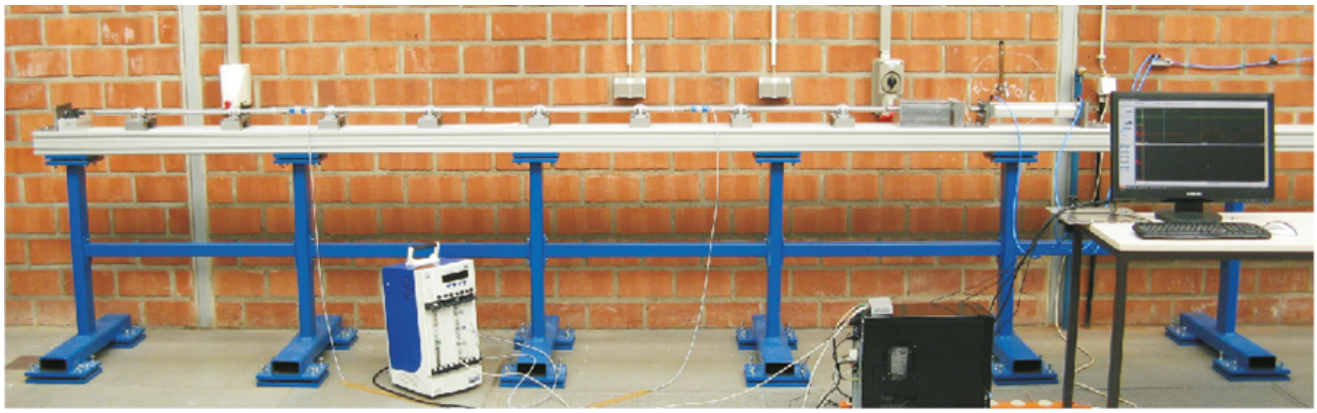

Figure 2.5: Split Hopkinson Bar test setup

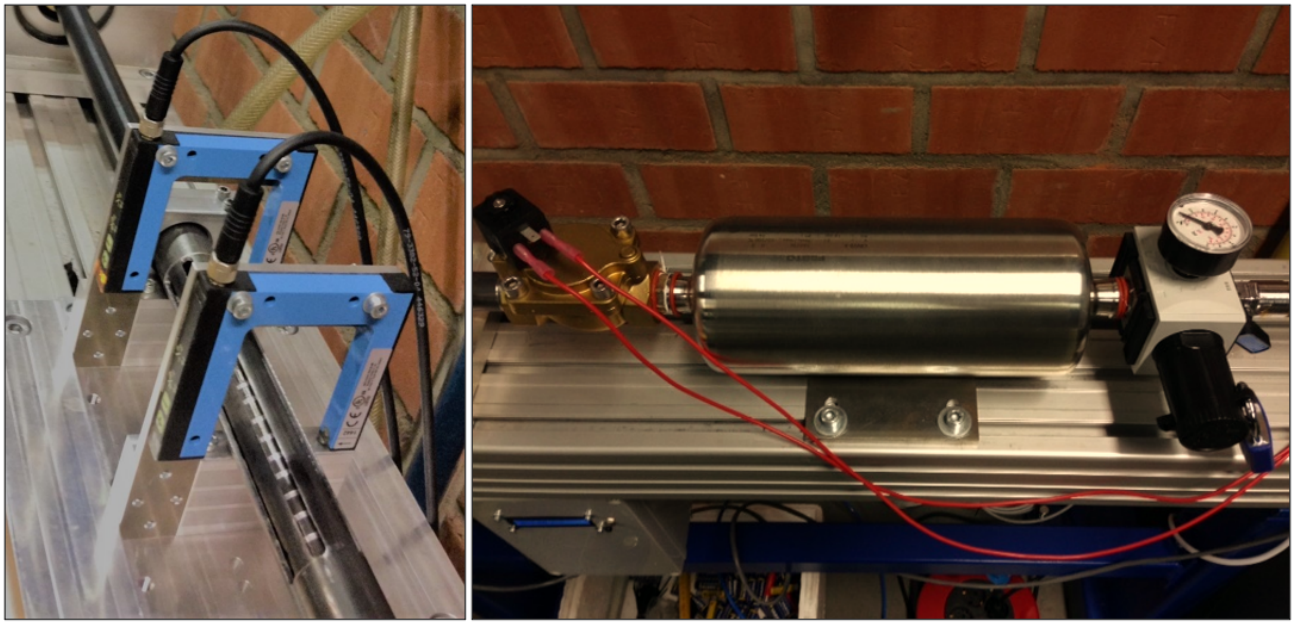

Figure 2.6: Gas gun and velocity sensor components of SHPB setup

	aluminum bars	PMMA bars
length [mm]	1800	1800
diameter [mm]	20	20
static elastic modulus [GPa]	70	3.5
density [kg/m^3]	2700	1178
wave speed [m/s]	5052	1716
impedance [kg/m$^2\mu$s]	13.64	2.02

Table 2.2: Dimensions and mechanical properties of aluminum and PMMA bars

The difference in acoustic impedances of aluminum bars and polymer specimen may result in an insufficient transmitted pulse. When the impedance difference is very large ($z_2 \gg z_1$) almost the entire wave is reflected at the interface of the incident bar and the specimen. As a result, only a weak or no impulse can be measured at the transmission bar. This holds true, in particular, for soft materials. The tested SR and TR materials have impedances of 0.7 and 0.6 kg/m$^2\mu$s, respectively. To reduce the impedance mismatch between specimen and bars, PMMA as bar material has been considered. In general, PMMA bars are suitable for testing softer materials. For resins with high impedance, aluminum bars are sufficient to obtain both a transmitted signal and a reflected signal. For soft resins, PMMA bar would be the only suitable choice to obtain a transmitted pulse. Details of the used PMMA bars are given in Table 2.2.

To record the wave data two strain gauges (DMS) with a resistance of 120.0 $\pm$ 0.1 Ω and a sensitivity coefficient of 2.14 $\pm$ 1% are appliqued in the middle of each bar.

2.2.2 Aluminum SHPB bar setup

The first SHPB setup uses aluminum (EN AW-6061) incident and transmission bars with parameters of Table 2.2. Aluminum cylindrical strikers, being made of the same aluminum with 20 mm diameter and length of 100 mm, are used. The mass of the aluminum striker is then 0.084 kg. The striker is accelerated by the gas gun, which results in a striker velocity of almost 10 m/s. From eq. 2.2 we calculate for aluminum bars and a SR specimen, transmitted wave portions of $\sigma_T/\sigma_I = 0.1$ which illustrates the problem of a high impedance mismatch.

2.2.3 PMMA SHPB bar setup

The second SHPB setup is equipped with the PMMA bars of the same length and diameter, see Figure 2.7. The corresponding cylindrical PMMA striker has also a diameter of 20 mm, a length of 100 mm and a mass of 0.037 kg; its acceleration results in a velocity

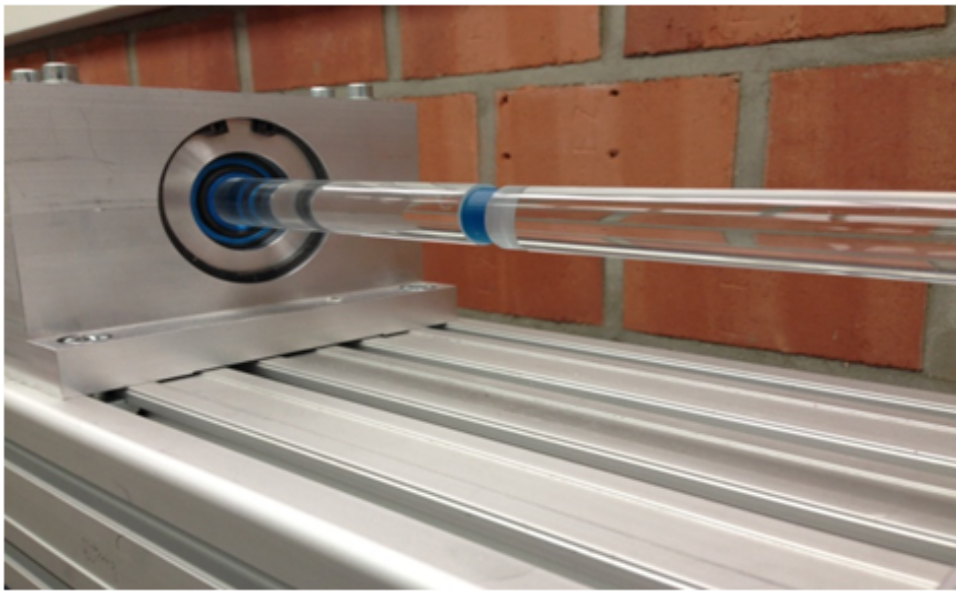

Figure 2.7: Tough resin sample fixed between PMMA bars

of 10 m/s. Since the PMMA bars tend to deform due to the impact, the striker velocity has to be calibrated carefully. For the PMMA bars and a SR specimen we calculate from eq. 2.2 transmitted wave portions of $\sigma_T/\sigma_I = 0.6$. This corresponds to our observation of the transmitted pulse being significantly higher when using PMMA bars, compared to aluminum bars.

2.2.4 Specimen preparation

Most of the dynamic tests are associated with inertia effects. Particularly, in SHPB experiment the sample is initially at rest and is expected to go under deformation in the desired rate [19]. This inertia effect could exist in both axial and radial directions and can influence the strain rate from zero to the appropriate desired level. It should be noted, that during SHPB test the goal is to determine the intrinsic material behavior and inertia effect should be controlled and minimized through the suitable specimen design in geometry and also experimental conditions (SHPB prerequisites) [19].

When testing with soft materials with SHPB inertia becomes even more severe due to their low strength. Many of such soft materials might experience large deformation under axial compression, whearas signficant expansion in radial direction takes palce[19]. In SHPB experiment the sample cross section size should not exceed the bar diamater, and since the bar diameter in our test is known (20mm), then the specimen diameter is limited for proper axial compressice strain.

Considering the assumption of incompressibilty, approximated little change in specimen volume is:

$$\frac{\pi}{4}d_0^2 l_0 = \frac{\pi}{4}d^2 l \tag{2.3}$$

Where d_0 and l_0 is the initial specimen diameter and thickness, respectively. d and l are also current diameter and thickness, respectively. Specifically, for compression experiment:

$$\frac{l}{l_0} = 1 - \epsilon_E \tag{2.4}$$

where ϵ_E is the engineering strain of the sample.

The two types of mentioned resins were printed by the SLA 3D printer (Formlabs), see Figure 2.2, with high precision, particularly to be tested under high loading- rate SHPB. After the printing process the samples were polished. Hence, the materials are considered to be homogeneous and isotropic throughout the test. In the next chapter, the concept of the SHPB test and the desired shape and geometry of the specimens are fully discussed.

The geometry of the specimens for the compression SHB tests is cylindrical with a diameter of 18 mm.

For the setup with aluminum bars, the samples have a length of 9 mm. Thus, the length-to-diameter ratio is 0.5 which is favorable to minimize inertia effects. Moreover, rather thin specimens are needed to facilitate the dynamic stress equilibrium [84, 85]. For the PMMA bars the length of the samples are 15 mm. Here we need longer specimen in order to obtain the same strain rate.

2.3 Prerequisites of SHPB testing

The soft materials being tested have common charachteristics of low strength, stiffness and wave mpedance. The loading condition, including rate and state of the loading play an essential role in mechanical response of the sample. During such dynamic tests, uniform deformation is neccesary to be achieved, which could be obtained through creating the stress equilibrium condition, in which the low wave speed in our soft specimens causes difficultes in creating stress equilibrium. The low strength makes the transmitted wave amplitude too weak to be accurately measured. Generally, in this condition, the sensitivity to strain rate and also the state of the stress would make the Prerequisites on test condition more strict.

One of the challenging issues is to achieve to uniform deformation in a soft specimen when conducting SHPB test due to the nature of the low wave speed in soft samples. It is assumed that the specimen deforms uniformly so that the deformation averaging on the length of specimen illustrates any point-wise deformation. Nevetheless, this assumption

requires other prerequisites to be applied for consideretion.

2.3.1 One-dimensional wave theory

The SHPB experiment is based on one-dimensional wave theory. The induced longitudinal wave $u(x,t)$, and its parts after reflection and transmission, are measured as strain signals $\epsilon_I(t)$, $\epsilon_T(t)$, $\epsilon_R(t)$, where the indices I, R and T refer to the incident, reflected and transmitted wave accordingly. The displacement at the specimen-incident-bar interface u_1 and the specimen-transmission-bar interface u_2 can be derived from the measured strain signals [18, 19].

$$u_1 = c_b \int_0^t (\epsilon_I - \epsilon_R)\,\mathrm{d}t \qquad u_2 = c_b \int_0^t \epsilon_T\,\mathrm{d}t \tag{2.5}$$

The indices b and s refer to bar and specimen, respectively. The strain in the specimen with the length L_s can be calculated by

$$\epsilon_s = \frac{u_2 - u_1}{L_s} = \frac{c_b}{L_s} \int_0^t (\epsilon_I - \epsilon_R - \epsilon_T)\,\mathrm{d}t\,. \tag{2.6}$$

From Hooke's law the axial stresses and the corresponding axial forces are derived. The reaction forces $F_1 = F_I - F_T$ and $F_2 = F_T$ result as

$$F_1 = EA_b(\epsilon_I + \epsilon_R) \qquad F_2 = EA_b(\epsilon_T)\,. \tag{2.7}$$

Averaging these forces and dividing by area A_s gives the stress in the specimen

$$\sigma_s = \frac{E_b A_b}{2A_s}(\epsilon_I + \epsilon_R + \epsilon_T) = E_b \frac{A_b}{A_s}\epsilon_T\,. \tag{2.8}$$

Then, the strain in the specimen and the strain rate result as

$$\epsilon_s = -2\frac{c_b}{L_s} \int_0^t \epsilon_R\,\mathrm{d}t \tag{2.9}$$

$$\dot{\epsilon}_s = -2\frac{c_b}{L_s}\epsilon_R \tag{2.10}$$

and the dynamic elastic modulus of the specimen is obtained by:

$$E_{\mathrm{dyn}} = \frac{\sigma_s}{\epsilon_s} = -\frac{A_b E \epsilon_T L_s}{2A_s c_b \int_0^t \epsilon_R\,\mathrm{d}t}\,. \tag{2.11}$$

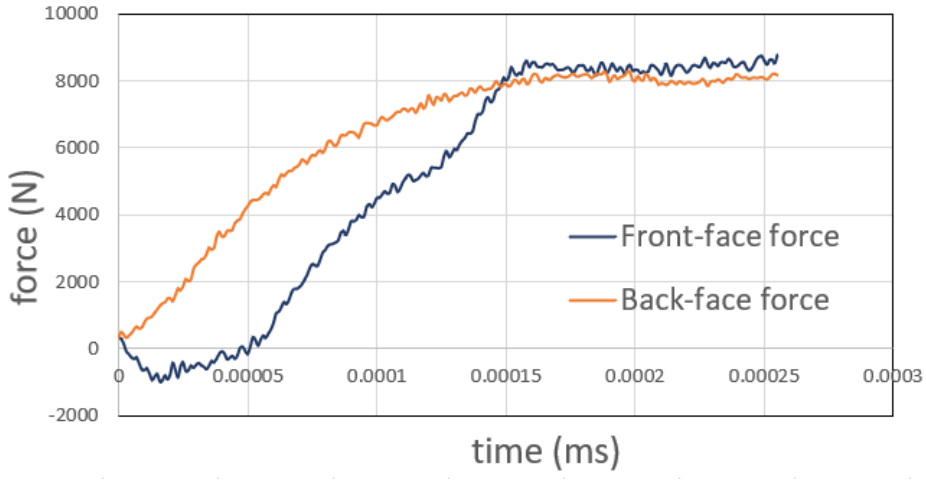

Figure 2.8: Full history of Front and back forces of a sample in aluminum bar, start of the stress equilibrium can be clearly observed

2.3.2 Stress equilibrium

The SHPB experiment is based on two fundamental assumptions: The first one is the assumption of one-dimensional wave theory, which is related to the calibration of the setup. The bars in the SHPB test must be well-aligned so that the stress wave propagates without significant lateral effects and without dispersion. For the SHPB test in this study, a laser technique was utilized in order to adjust the proper bar alignment, as mentioned earlier. The second assumption is the stress equilibrium condition, which is related to an instantaneous equilibrium of forces in the loaded specimen, $F_1 \approx F_2$, Eq. (2.7). This assumption is basically related to an axially uniform state of deformation and needs to be examined during the test. To do so, we use here a strategy suggested in [86] and determine a parameter relating the forces Eq. (2.7) at the specimen-incident bar interface and the specimen-transmission bar interface, respectively.

$$R(t) = \frac{\Delta F(t)}{F_{avg}(t)} = 2\left|\frac{F_1(t) - F_2(t)}{F_1(t) + F_2(t)}\right| \tag{2.12}$$

The specimen is in stress equilibrium when $R(t)$ approaches zero and for $R(t) < 0.05$ it is considered to be acceptable. In our experiments stress equilibrium was easy to obtain for the PMMA bars but for aluminum bars it was more challenging. By applying a pulse shaper technique and also controlling the speed of the striker [87], an acceptable stress equilibrium of $R(t) = 0.04$ was achieved here. The full front and back force profiles of the specimens in aluminum and PMMA bars are illustrated in Figures 2.8 and 2.9.

In addition to the two fundamental assumptions, friction and inertia effects are important issues during SHPB testing. In order to minimize friction for the specimens, the sample-bar contact surfaces were lubricated. Inertia has already been addressed by the

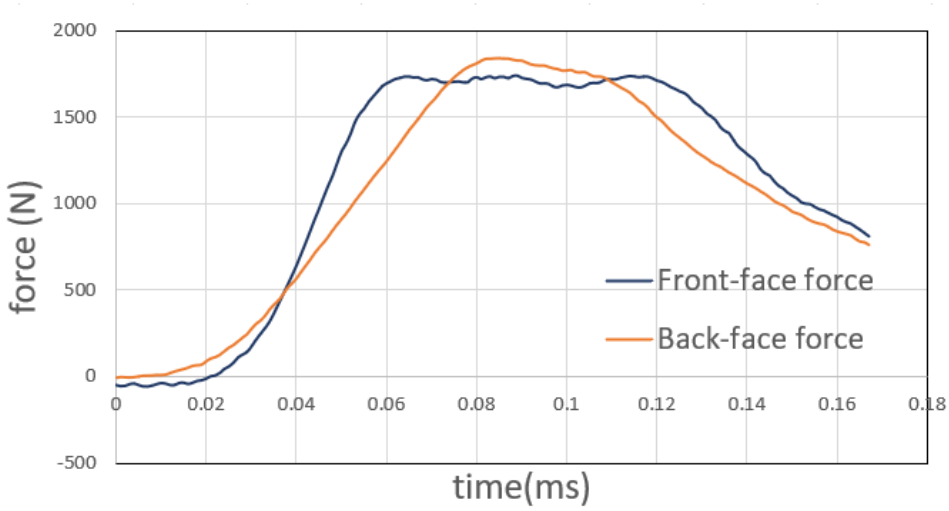

Figure 2.9: Full history of Front and back forces of a sample in PMMA bar, start of the stress equilibrium can be clearly observed

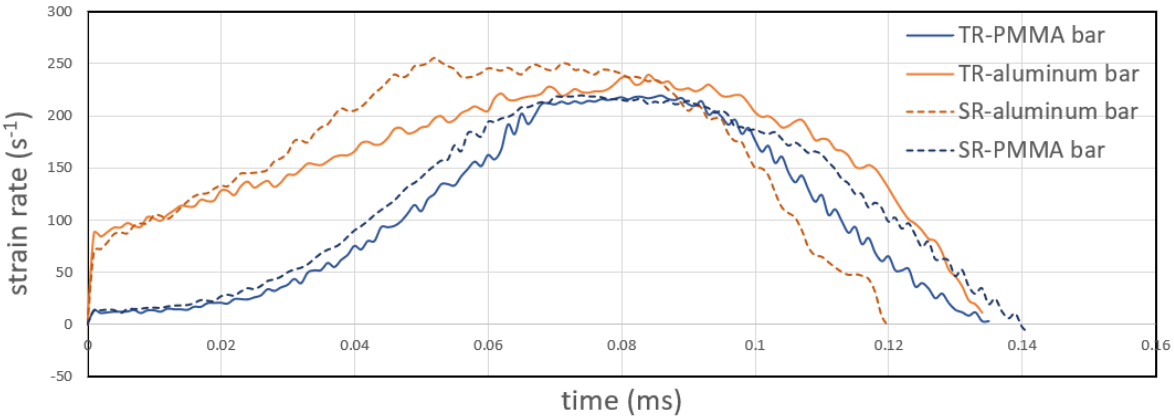

Figure 2.10: Full strain rate history of SR and TR samples in aluminum and PMMA bars

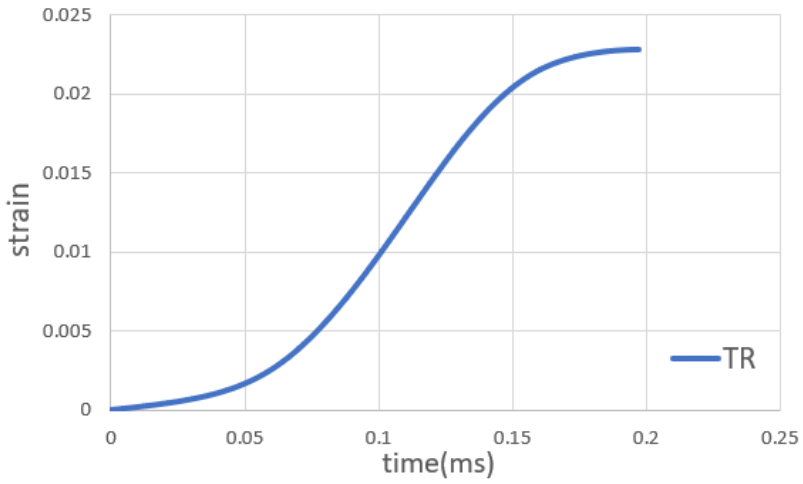

Figure 2.11: Constant strain rate of a TR specimen

design of the specimens, Section 2.2.4. The goal of SHPB testing is to determine the intrinsic material response and significant inertia effects can cause extra axial stresses, which blur the result [19].

As stated earlier, to obtain precise result the strain rate is desired to be constant and as presented in the previous subsection constant strain rate deformation would help to diminish the inertia effects. Since the impact experiment does not allow real-time adjustment on the laoding pulse, according to sample behavior, the adjustment process on the control to reach the desired testing condition on the specimen is iterative. Mostly, the conventional trapezoidal types of incident would not satisfy the requirement of the constant strain rate deformation, but the transmitted wave from the test counts as important information about the specimen feedback and response [19]. Based on this respond, the incident pulse can be modified in the next attempt in order to approach dynamic stress equilibrium and constant strain rate. This will lead us to incident pulse modification through using the pulse shaper.

2.3.3 Pulse shaping

Pulse shaping technique is utilized to facilitate the stress equilibrium and constant strain rate deformation in the sample by appropriately modifying the profile of the incident pulse based on the response of the sample in the test [19]. To reach to a better constant strain rate deformation in specimen the incident pulse is required to posses a similar profile to the stress response of the tested sample, reprensted by the transmitted signal [19]. The shape of the incident pulse is controlled by using the right pulse shaper. During the intial timing of the dynamic loading the incident signal should have a moderatly low rate of loading to reach to a better stress equilibrium and also minimized accelaration-induced inertia [19].

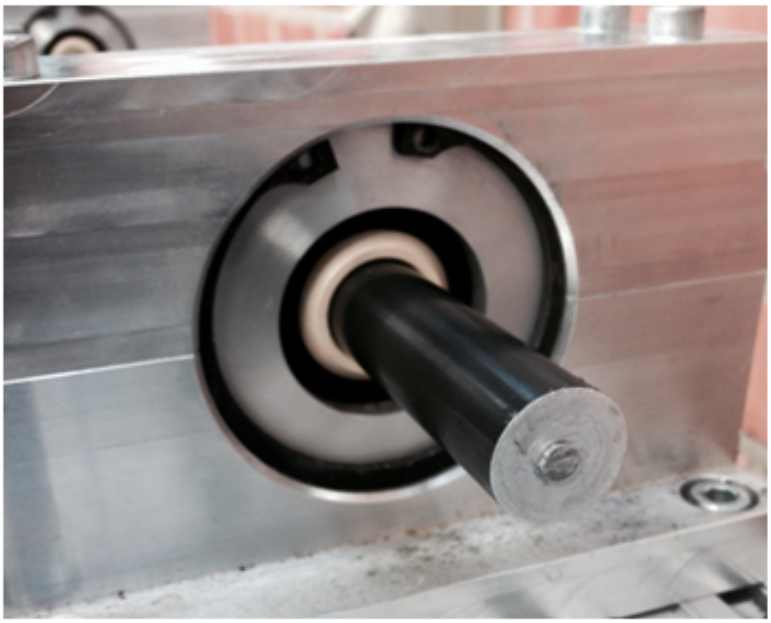

Figure 2.12: Lead pulse shaper on the aluminum bar

For a well-defined strain rate in a SHPB test, the ideal incident pulse needs to rise to its maximum with a long rise time. To shape the wave pulse, thin cylindrically shaped lead plates with the thickness of 0.3 - 0.5 mm were fixed with grease at the impacted end of the aluminum incident bar, Figure 2.12. These pulse shapers can be plastically deformed, which enables a constant strain rate and also diminishes the oscillations of the wave [22, 84]. The full strain rate history of two SR and TR samples are shown in Figure 2.10. The nearly constant strain rate for about 0.05 ms can be observed for these tested resins. In addition, Figure 2.13 shows the effect of pulse shaper on an incident pulse in aluminum SHPB test.

In the PMMA SHPB setup the incident strain waves are smoother. So it is not necessary to apply a pulse shaper to the incident bar surface.

2.3.4 Signal correction

In PMMA bars wave scattering is reduced but the viscosity of the polymeric materials requires additional effort for data acquisition. The pulse measured at the strain gauge appliqued in the middle of the bar is not necessarily the same as the pulse entering the specimen and so an adaption of the signal is needed. Therefore, preparatory experiments analyzing the wave propagation in a single PMMA bar were conducted. After striker impact the back and forth traveling pulse is measured. Since the ends of the bar are free, the complete impulse is reflected but the amplitude decreases exponentially with time. Thus, an exponential function was fitted to the amplitude $A(x)$ of the measured

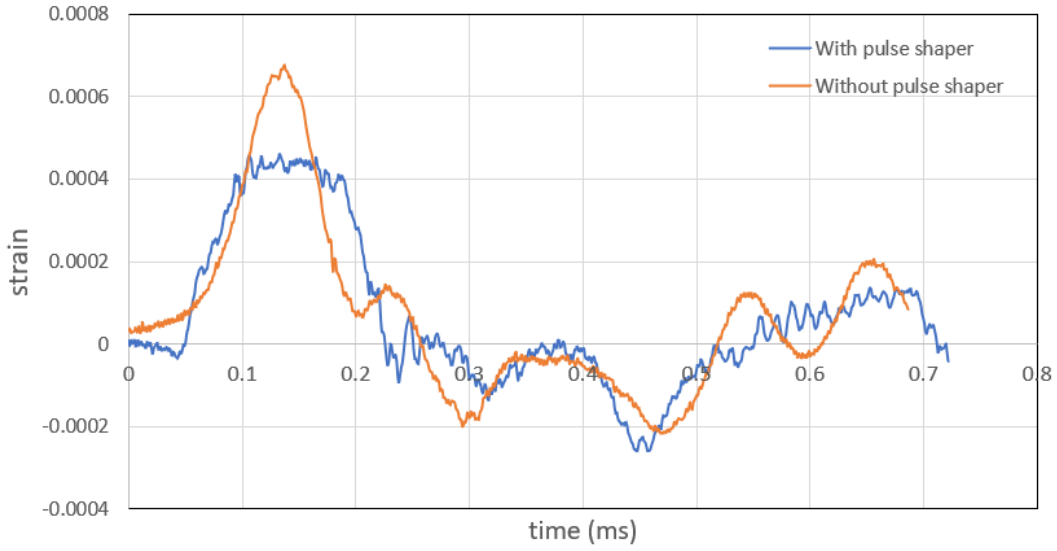

Figure 2.13: Effect of pulse shaper on an incident pulse with aluminum bars

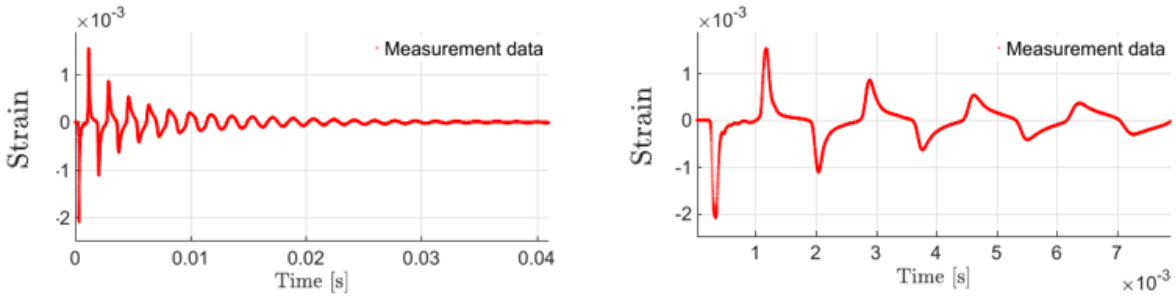

Figure 2.14: Measured signal for incident bar (left), zoomed range of the signal (right)

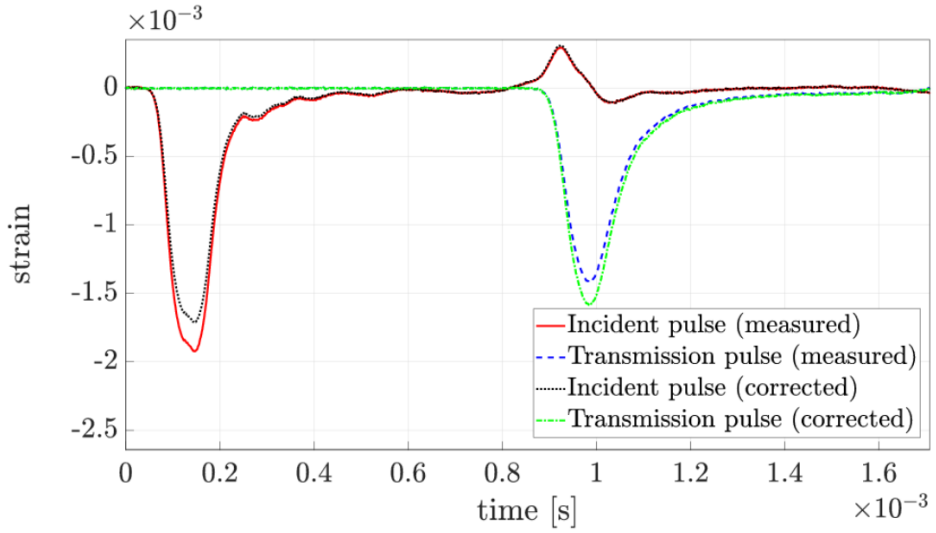

Figure 2.15: Measured and corrected signal at the center of the two PMMA bars

signal and the free coefficients are adapted.

$$A(x) = a\, e^{b\,x} + c\, e^{d\,x} \tag{2.13}$$

Here x is the distance the wave moves through the material. The coefficients of Eq. (2.13) are $a = 1.656 \cdot 10^{-3}$, $b = -0.2166 \cdot 10^{-3}$, $c = 0.4267 \cdot 10^{-3}$ and $d = -0.04539 \cdot 10^{-3}$ for our SHPB setup and striker velocity. Other setups and specifications require a new calibration of these damping coefficients.

Based on this fit the signal at the bar-specimen interface can be estimated. For the measured incident pulse $\epsilon_I(t)$ the amplitude has to be corrected downwards, while for the measured reflected pulse $\epsilon_T(t)$ and transmitted pulse $\epsilon_R(t)$ the amplitude has to be corrected upwards. The corrected signal is then used to evaluate the SHPB equations (2.8-2.10).

Figure 2.14 shows the recorded signal of the strain gauges of the incident bar. The changing sign results from the change in direction of the impulse. As can be seen, the measured amplitude decreases exponentially with time. An exponential function was fitted to the determined amplitudes of the measurement signal. To correct the signal, the distances between strain gauge and bar end respectively begin is necessary.
With a measured signal (strain gauges centrally mounted on the bars) , the signal at the contact surface can be estimated on the basis of the fitted curve.

The curve displayed in Figure 2.15 shows the measured signal before and after correction. The primitive signal correction is working well for our study because the PMMA bars does not significantly change the shape or length of the wave. This approach is verified with numerical calculations in Section 2.5. A more elaborate method of signal correction is covered in another study by the authors [88].

2.4 Experimental results

SHPB experiments need to be conducted multiple times in order to obtain reproducible results for wave shape, stress equilibrium and deduced values. Here, eight specimens of each resin material of Table 2.1 were evaluated in both experimental setups. In order to gain the intrinsic behaviour of the resin, each sample was tested only once.

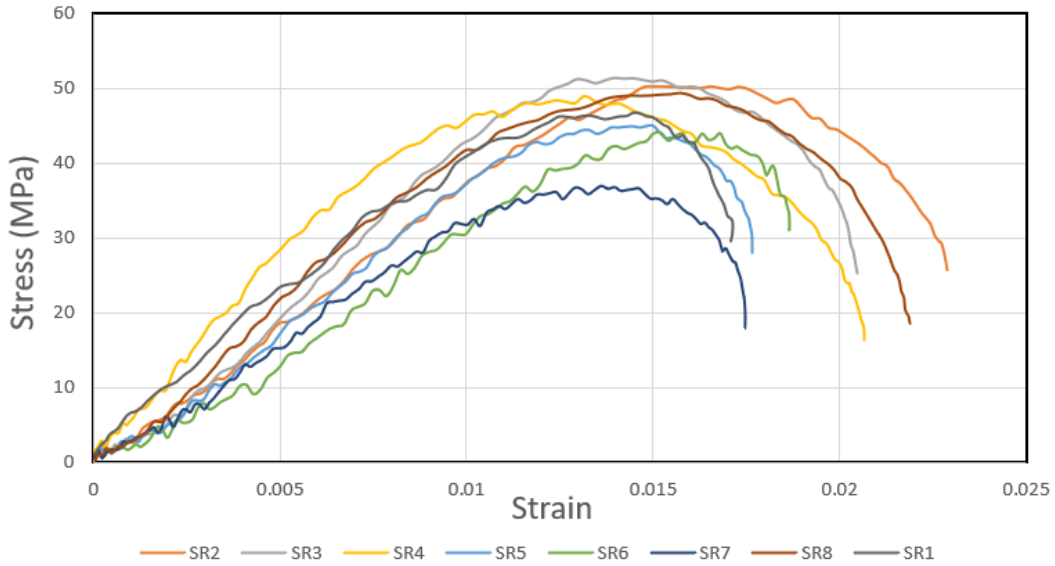

Figure 2.16: Measured stress-strain curves of eight SR samples in the aluminum SHPB setup

2.4.1 Aluminum bars

In the aluminum SHPB setup the striker hits the incident bar with a velocity of about 10 m/s. This leads to a maximum stress of about 50 MPa in both groups of specimens, see Figure 2.16 and Figure 2.19. Using equation (2.11) and a regression method for the precise slope calculation of the stress-strain curves, we deduced a mean dynamic elastic modulus of 3.7 GPa for the SR and 3.4 GPa for TR. It should be noted that for the regression only the linear part of the stress- strain curves (up to 0.5% strain) is considered. The strain rate is always in the range of $200 - 250\,\mathrm{s}^{-1}$. The values of the dynamic elastic modulus are significantly higher than the static modulus given by the manufacturer, which indicates a strain rate dependency in the polymeric resins.

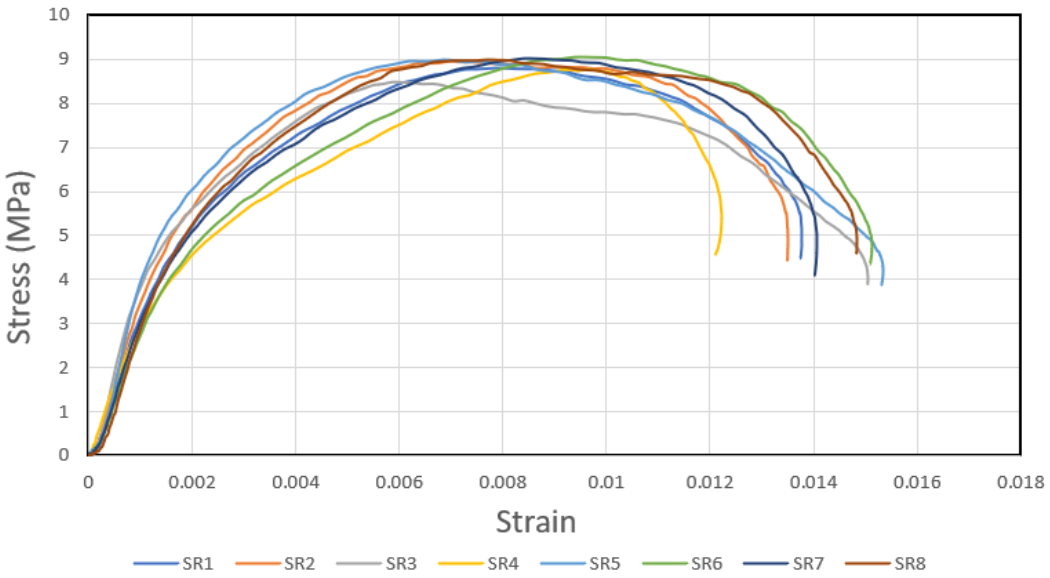

Figure 2.17: Measured stress-strain curves of eight SR samples in the PMMA SHPB setup

2.4.2 PMMA bars

The signals measured with the PMMA bars are corrected as described above. Here the maximum stress in the specimen is approximately 9 MPa and significantly lower than in the previous setup, see Figure 2.17. The reduced stress is related to the smaller elastic modulus of the PMMA but it does not play a role for deriving the dynamic elastic modulus of the resins, since only the stress-strain slope is evaluated.

The behavior of the resin specimens is almost the same. Again, regression is used and only the linear part of the stress- strain curves (up to 0.15% strain) is evaluated. For SR, a mean elastic modulus of 3.8 GPa is obtained, whereas for TR the mean is 3.4 GPa. All obtained values and their standard deviations are summarized in Table 2.3.

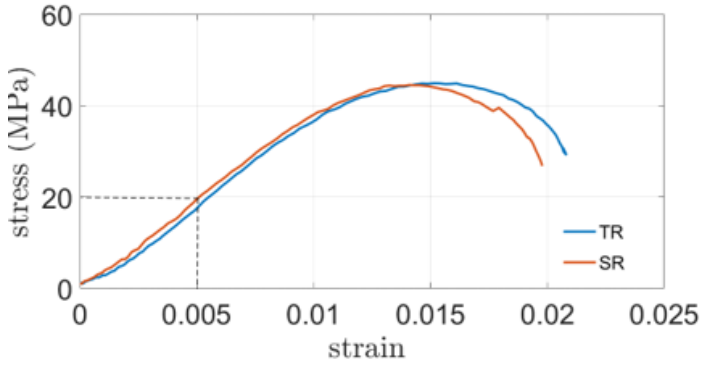

Figure 2.18: Mean stress-strain curves for both groups of specimen tested in the aluminum bar setup; the box indicates the evaluated strain range

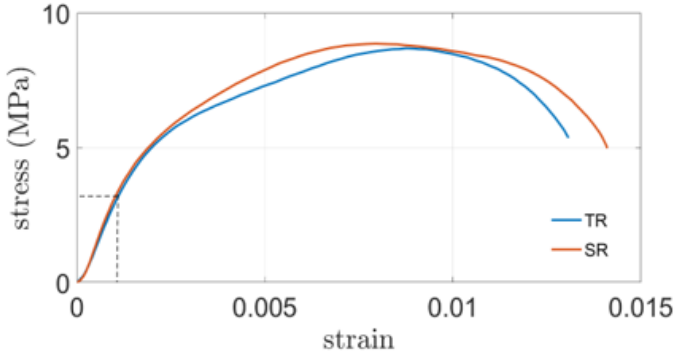

Figure 2.19: Mean stress-strain curves for both groups of specimen tested in the PMMA bar setup; the box indicates the evaluated strain range

2.5 Numerical simulations of the SHPB setups

In order to evaluate the effect of the two different SHPB setups we simulate the experiment by means of a finite element (FE) analysis with the commercial program Abaqus

resin	Aluminum SHPB			PMMA SHPB		
	striker vel. $[\frac{\text{m}}{\text{s}}]$	mean $\dot{\epsilon}$ $[\text{s}^{-1}]$	E_{dyn} [GPa]	striker vel. $[\frac{\text{m}}{\text{s}}]$	mean $\dot{\epsilon}$ $[\text{s}^{-1}]$	E_{dyn} [GPa]
SR	10	236	3.7 ± 0.9	10	215	3.8 ± 0.4
TR	10	250	3.4 ± 1.3	10	207	3.4 ± 0.9

Table 2.3: Experimental results for standard resin (SR) and tough resin (TR).

[26]. The main purpose of the simulation is to validate the strain wave propagation assumptions and to evaluate the corresponding wave signals.

The FE model was built for the full SHPB arrangement. All components are isotropic linear-elastic and meshed with three-dimensional 8 node linear brick elements, Figure 2.20. The boundary conditions are chosen so that only longitudinal movement is allowed and at the interfaces surface to surface contact was defined. We use an explicit time integration (Abaqus explicit).

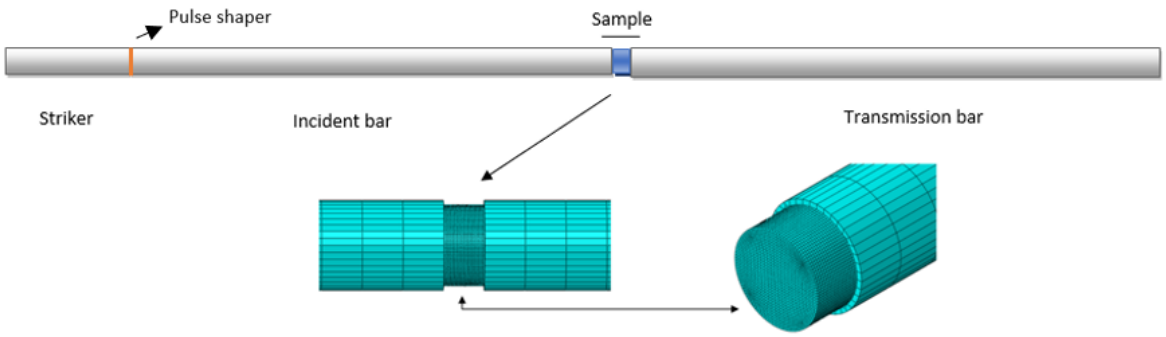

Figure 2.20: FE-Mesh configuration of the SHPB setup

Parametric studies have been performed with strikers of 100 mm length and a predefined velocity of 10 m/s. The damping of the PMMA bars is modeled with a Rayleigh damping. For the aluminum bar a pulse shaper was added by a contact to contact surface. However, because the plastic properties are not well known, we had to reduce the impact speed to recover the incident wave. Figure 2.21 shows exemplarily the incident pulse propagation in aluminum. Although a slight discrepancy between simulation and experiment still remains, the pulse can be recovered quite accurately.

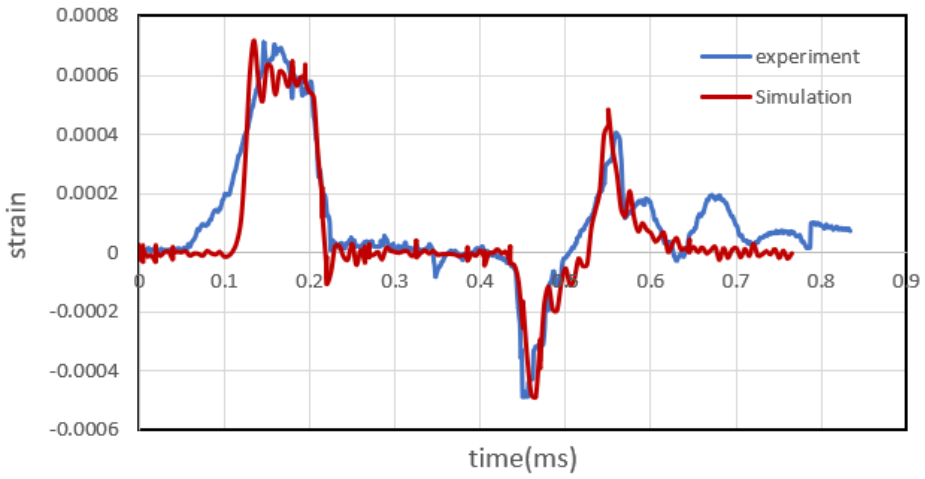

Figure 2.21: Incident pulse propagation history in the aluminum SHPB setup

Figure 2.22 shows the incident wave pulse in a PMMA bar. For the experiment, the mean of the strain waves from the eight tested samples of each group is plotted. Here also exists a good agreement between the experiment and simulation waves.

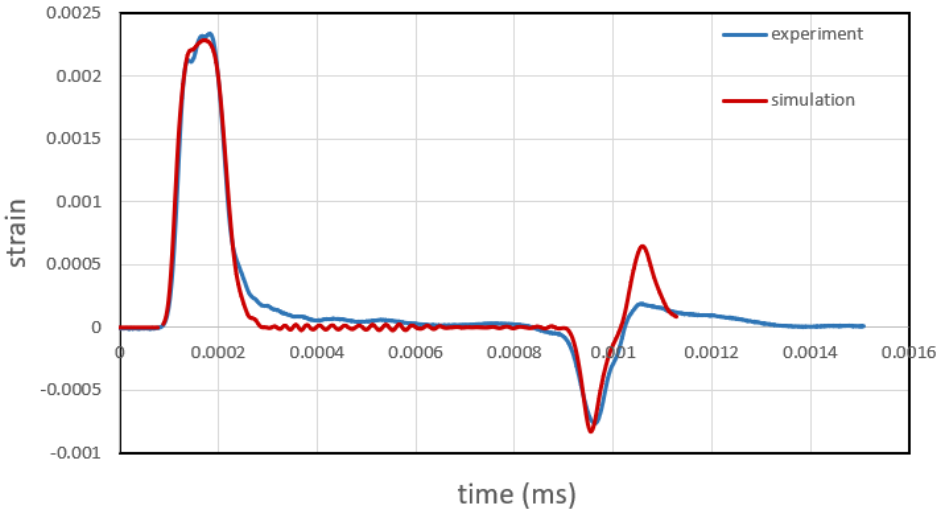

Figure 2.22: Incident pulse propagation history in the PMMA SHPB setup

In Figures 5.12 and 2.24 the transmitted pulse is shown for both setups. Again we observe a good agreement between the strain waves, although there are slight differences in some parts, which can be caused by several reasons, mainly related to the experimental condition.

Moreover, mesh convergence studies were performed by implementing two different mesh densities (total number of elements 80976 [used], and 289576), and the represented

numerical simulation results were compared and prove the convergence. The run time of the explicit simulation is 22 minutes for the used mesh density (mesh density1). Time cost might differ based on computer power. The implicit method would work on this simulation as well, but it should be noted that the time and computational cost would be more significant rather than the explicit method (approximately lasts several hours on the same computer power).

In general, it is recommended to consider the fact that the numerical results are much more reproducible than the experiments, as the conditions of the shots vary during the tests. Hence, during this study, we could validate the assumption of linear-elastic specimens, and the general improvement obtained by fit (2.13). Furthermore, the stress on both sides of the specimen in simulation for both setups is shown in Figure 2.26.

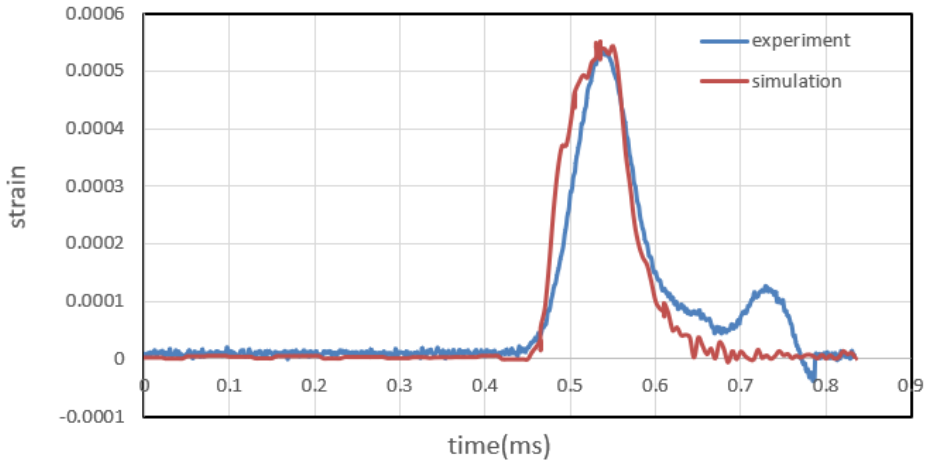

Figure 2.23: Transmitted pulse propagation history in the aluminum SHPB setup with a TR sample

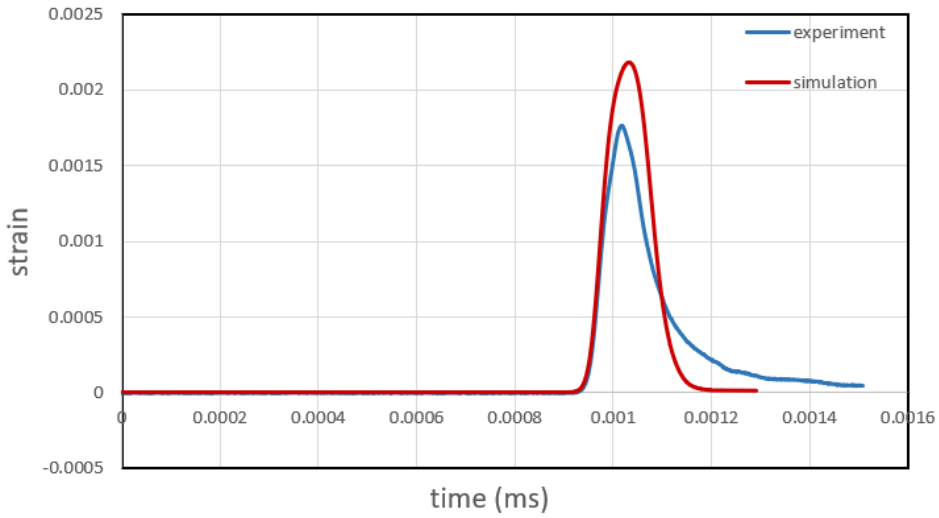

Figure 2.24: Transmitted pulse propagation history in the PMMA SHPB setup with a TR sample

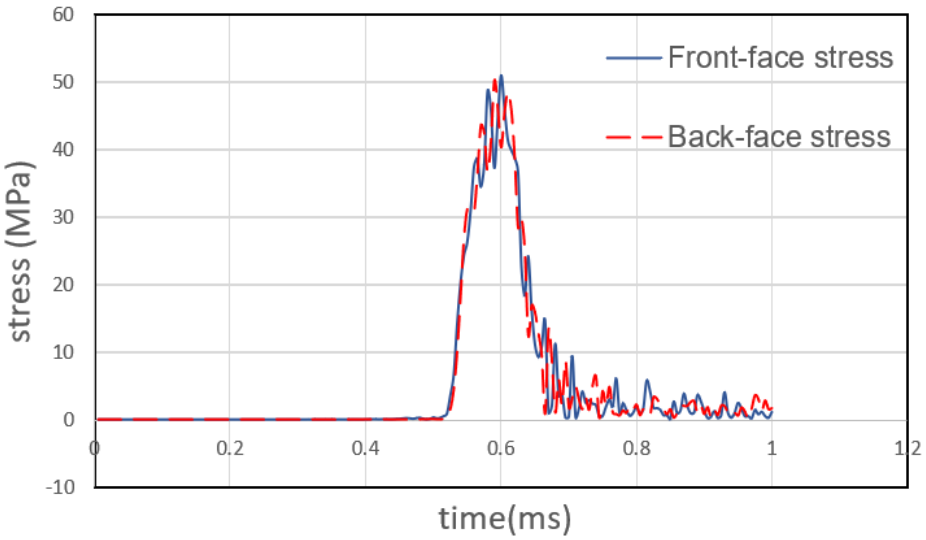

Figure 2.25: Stress on both sides of the specimen in aluminum bar

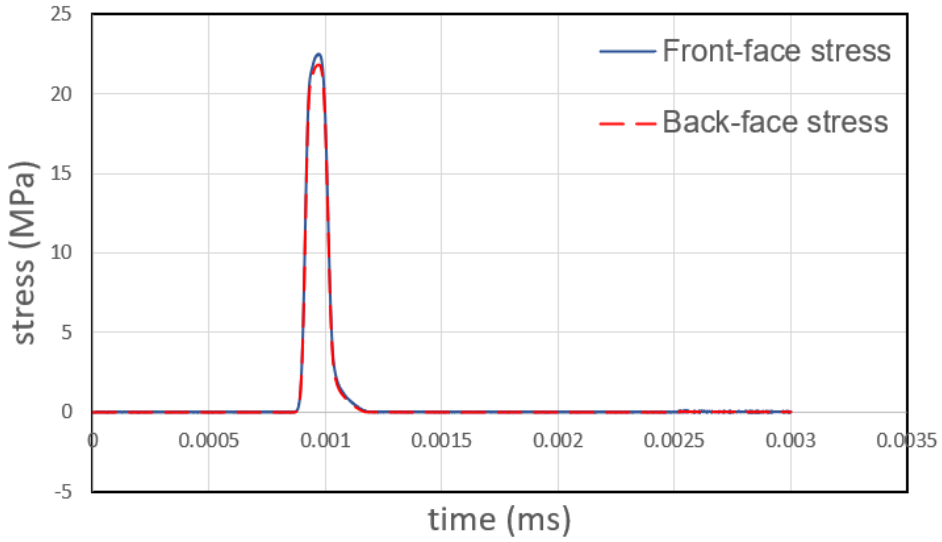

Figure 2.26: Stress on both sides of the specimen in PMMA bar

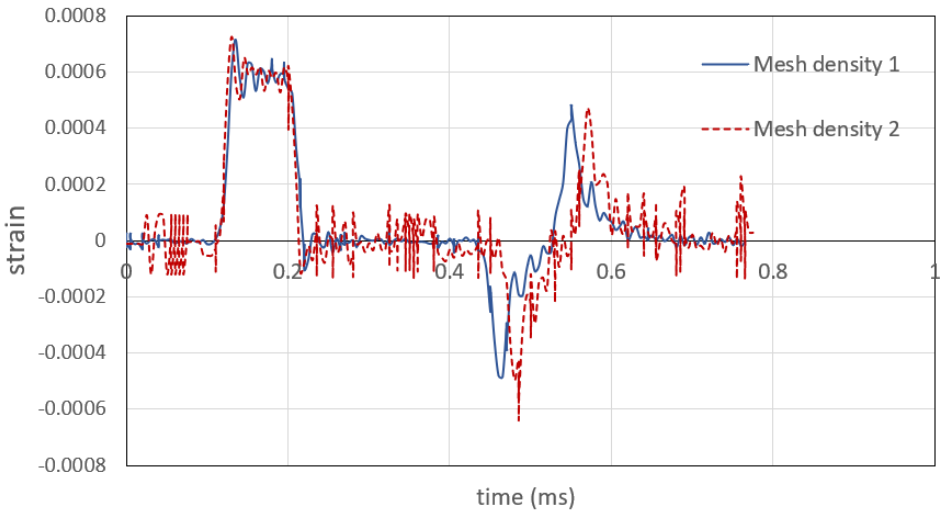

Figure 2.27: Incident pulse propagation history in the aluminum SHPB setup of both mesh sizes (mesh convergence)

2.6 Discussion and conclusion

SHPB experiments take a lot of attempts to obtain the best possible waves and the final outcome. Certainly, utilizing different bar materials changes the test conditions and the experimental details such as pulse shaping and data acquisition need to be adapted.

The waves gained from aluminum bars required pulse shaping in order to obtain a constant strain rate and to reduce dispersion, while there is little need for pulse shaping in the PMMA bar setup. Due to the inherent damping of PMMA, the strain wave shows almost no scattering but needs an amplitude signal correction. Further, the stress equilibrium is achieved more conveniently by using PMMA bars.

The FE analysis confirms the assumptions of the experiment and reproduces the waves nicely. Also the wave speed in the bars corresponds in the experiment and in the simulation. For instance, the experimental wave speed in the aluminum bar is 5015 m/s and in the FE model it is 5000 m/s, which is another indication of the good agreement between the test and simulation. In addition, the stress on the both sides of the specimen is shown in Figure 2.26. Of course, some differences remain and are likely due to the condition of the test such as non-ideal contact.
In total, utilizing the PMMA bars requires more effort during and after the test, although less scattering in the prorogated waves and less varying results are obtained.

The vast applications of resins, specifically for 3D printing, has motivated us to investigate their dynamic behaviour under high strain rates. Samples of standard and tough resin were tested in two different split Hopkinson pressure bar setups, one with aluminum and one with PMMA bars. In the PMMA bar setup the incident strain waves are smoother but have a lower amplitude than in the aluminum bars.

In our experiments we obtained mean dynamic elastic moduli of 3.7 GPa for standard and 3.4 GPa for tough resin with aluminum bars. With PMMA bars, mean dynamic elastic moduli of 3.8 GPa for standard and 3.4 GPa for tough resin were obtained. The corresponding strain rates are 200-250 s^{-1}. The dynamic values are about one-third higher than the corresponding static moduli of 2.8 and 2.7 GPa for SR and TR samples, respectively. Clearly, both setups give a very similar dynamic response of the specimen. The test results illustrate that the MMA based white standard resins have a slightly higher dynamic elastic modulus, comparatively.

In parallel to the experiment, finite element simulations were conducted to verify the tests. The computed waves are in good agreement with the experimental results. This allows us to conclude that PMMA incident and transmission bars are recommended for the dynamic testing of resin specimens.

3 Soft tissue simulant material dynamic behavior

This chapter considers the basics of brain tissue properties and the related agarose gel properties and the preparation process. The bubble dynamics, including the theoretical background and variational model is represented in this chapter. The section of variational model of bubble growth and the constitutive equation is already submitted for publication by us, in [89].

Investigation on dynamic response of materials that mimic biological soft materials at high rate loading has become increasingly important due to the essential role in different biomedical applications, i.e., injury mechanisms impact [90, 91]. Accurate investigation and characterization of the soft biological materials are becoming more important because of their growing implications in various areas of biology, medicine and also biomaterials, including in vitro wound healing assays [92], regenerative tissue engineering [93], stretchable bioelectronics for skin surface application or implantation [94, 95] and microfluidic systems for biological studies [96, 97]. When the biological system is exposed to the impact, the human brain is rapidly accelerated, which results in the acceleration-induced pressure gradient. Depending on the amplitude and duration of such mechanical impact, the biological tissue is mainly subjected to a wide range of deformation and even more considerably crucial damage, associated with the formation of bubbles, known as the "Cavitation phenomena".

In order to gain a precise prediction of possible injuries, a basic understanding of how soft materials respond under rapid loading or equivalent acceleration is critical. Mainly the biological tissues are simulated by using soft materials, e.g., balistic gelatin, which are often used in crash or ballistic experiments to replicate soft body parts. Their mechanical properties are at the boundary between fluid and solid and they undergo large, rubbery, and often time-dependent deformations. By now their material behavior is not yet fully understood but Despite all the chalenging points of utilizing the biological hydrogels, these soft bio-materials are considered for the experimental and numerical investigation of the onset, growth and collapse of the bubbles.

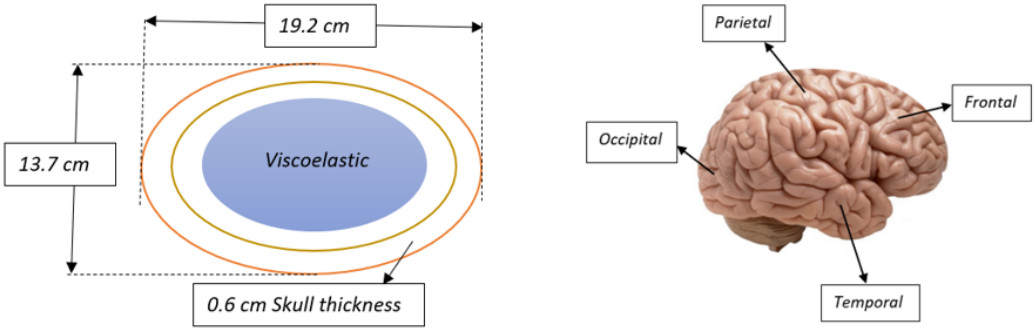

Figure 3.1: Average head geometry model (left), different brain lobes (right)[99]

3.1 Brain tissue

Baisically human brain is a soft metabolically active tissue, suspended in cerebrospinal fluid (CSF) within the rigid cranium. This environment play an important role in isolating the brain from the external mechanical loads on the head [98]. It is quite normal for the brain to withstand a specific range of mechanical load directly, related to the blood flow and also CSF material and in addition to that a tiny major of body posture. The blood circulation and CSF flow would also maintain the dynamic balance of pulsatile hydrodynamic forces in the skull, throughout the cardiac cycle (the Monroe-Kelly hypothesis) [98], due to the constant internal volume of the skull.

The brain tissue is composed of an outer layer known as gray matter, including cell bodies and dendrites beside axons, and an inner core of white matter consisting primarily of myelinated axons. The cerebrum as the largest section of the brain consists of two cerebral hemispheres, in which each of these hemisphere has an inner core composed of white matter, and an outer surface, known as the cerebral cortex which is composed of grey matter. It is also important to know that each hemisphere of the brain is traditionally divided into four lobes of the frontal, temporal, parietal, and occipital lobes, see Figure 3.1. The commissural nerve tracts play the role of connection of hemispheres, in which the most important one is known as the corpus callosum.

In the briefly explained anatomy of the brain tissue, the role of CSF was also mentioned. This colorless transcellular fluid circulates around the brain mostly in specific holes and spaces in the brain such as the subarachnoid space, ventricular system, and in the central canal of the spinal cord [101], see Figure 3.2. The estimations illustrate that around 150 mL of CSF exists especially in subarachnoid space, which is constantly being regenerated and replaced in the brain.

The effort to model and determine the soft tissue of the brain has been continuously ongoin, although the biomechanical studies and dynamic behavior of simulated soft

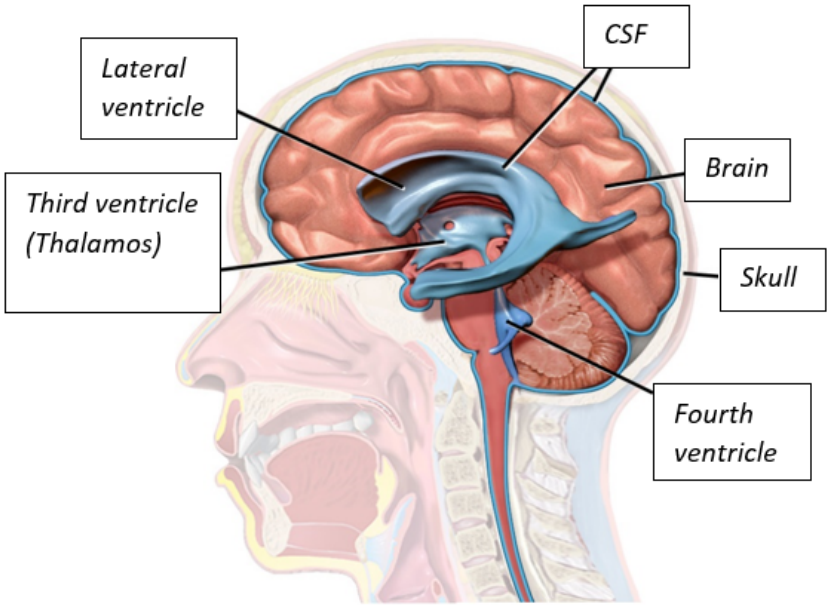

Figure 3.2: CSF distribution (ventricles) map in the brain (adapted from [100])

tissue materials have been recently accelerated. Soft tissues including brain tissue have nonlinear behavior and the relatively low stiffness of such materials have made them more struggling for simulation and modeling.

3.2 Brain injury related cavitation

Basically, cavitation occurs when the local pressure in the liquid reduces below the vapor pressure. This pressure gradient in each medium could orginated from different causes. Specifically, in this study, the cavitation related to the brain damage from traumatic brain injury (TBI), induced by impact or acceleration is investigated. Brain damage caused by TBI under impact/acceleration is mainly divided into two groups of focal and diffuse. The first consists of contusions, lacerations and tentorial/tonsilar herniation. Focal damage may also occur as coup or contrecoup (opposite to the site of impact), see Figure 3.3. On the other hand, diffuse damage encompasses diffuse axonal injury (DAI), cerebral swelling and is often associated with focal damage [34]. Some of the frequent causes of the damage are related to the motion of the brain with respect to the skull, including striking and bouncing of the parenchyma against inner skull protrusions. DAI is mainly related to the shear damage originated by the rotational movement of the parenchyma within the skull and also bending/stretching of the craniospinal junction [102]. In these sorts of injuries rotational or bending motions might cause severe shearing of axons in different brain regions [103, 104], and is observed in almost 30% of

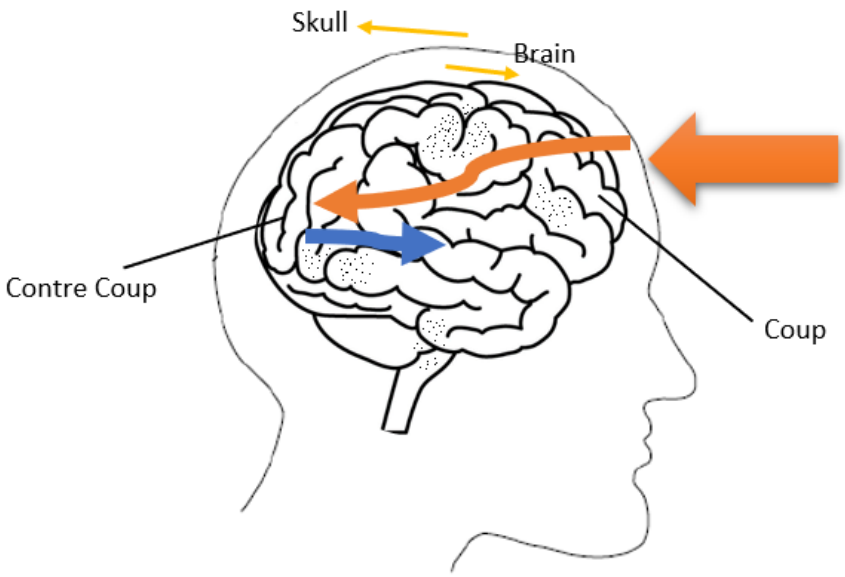

Figure 3.3: Coup–contrecoup injury schematic

the injury cases related to brain damage [102].

Cavitation induced by the negative pressure, also known as the volumetric or compression–tension damage, is one of the most important ones. Moreover, the other part of the injuries could result in rupture of bridging veins, axonal fibers and vascular tissue, also known as shear damage [34].

The dynamics of a frontal impact injury in TBI are associated with volumetric damage. The translational cranial motion leads to relative brain movements and the consequent intracranial pressure gradients. High positive pressures are observed at the coup site,

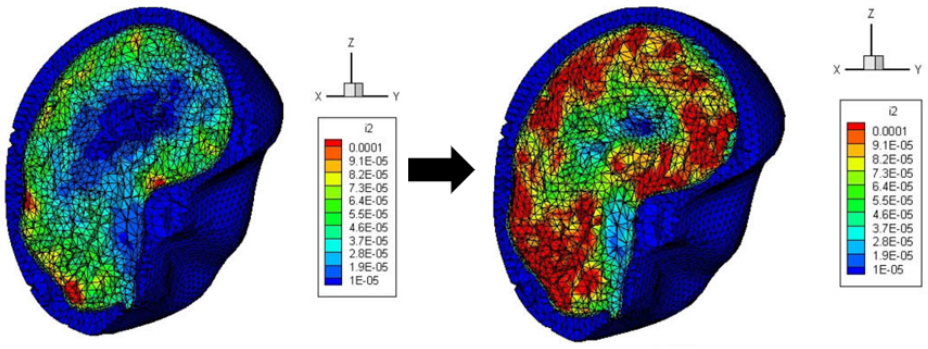

Figure 3.4: Frontal impact: cavitation damage [34]

	GM	WM	BSCC
Mass density[kg/m^3]	1040	1040	1040
Long-term shear modulus[kPa]	6.80	8.20	11.60
Bulk modulus[kPa]	2190	2190	2190
Yield stress[kPa]	20	20	20
Hardening exponent	10	10	10
Initial void radius[m]	100	100	100

Table 3.1: Material properties of soft tissue suggested by [34], GM = gray matter; WM= white matter; BSCC = brain stem and corpus callosum.

together with marked negative pressures at the contrecoup site [34]. Coup injuries are produced by the slapping effect of the skull hitting the brain; contrecoup lesions follow from the bouncing of the brain against the inner posterior surface of the skull and the possible development of cavitation bubbles within the brain due to high negative pressures. The growth and collapse of these bubbles may induce local tissue damage[34].

Vapor bubbles form when pressure falls below the saturated vapor pressure as may occur during the passage of tensile pressure. Coup cavitation is caused by high negative pressure, following intense shock wave in both coup and contrecoup areas [34]. There is a high potential for the resulted cavitation bubbles to form, grow and collapse within cerebrospinal fluid (CSF) and brain tissue. CSF carries dissolved gasses, and cavitation can be induced within CSF or other fluid compartments within the brain [34]. Nucleation of cavitation bubbles may occur through heterogeneous nucleation, initiating at junctions of liquid-solid boundaries, e.g., particulate surfaces. However, pre-existing gas nuclei can act as another source [28].

Figure 3.4 shows Contour plots of the intracranial pressure over a mid-sagittal section of the head model, in a work implemented by El Sayed. et al, in which the traveling stress reflects back by the skull at the contrecoup site and then moves back toward the interior of the parenchyma. It is then followed by the negative pressure wave leading to volumetric damage in different brain areas [34]. Cavitation initiates when the tensile stress reaches to a critical value P_c. This would lead to unstable growth of bubbles in the tissue and is locally amplified by the superposition of primary and reflected tensile waves [34].

	Skull	CSF
Mass density[kg/m^3]	1210	1004
Bulk modulus[kPa]	4760	2190
shear modulus[kPa]	3280	0.50

Table 3.2: Skull and CSF properties [34]

3.3 Soft tissue simulants Hydrogels

Hydrogels are considered to be one of the most important natural and synthetic materials nowadays, used largely in biomedical applications with the purpose of simulating different body organs, mainly as tissue simulant materials with different stiffness ranges. The main function of using gels and hydrogels is related to tissue engineering section of bimedical applications, and probably the most important one, in order to build tissue scaffold. The majority of materials used as the tissue simulant materials in tissue engineering are the same as the ones used for impact study applications such as crash test impact for instance, in order to simulate the head and the pressure gradient studies in such fields. These investigations mainly include the direct and indirect effects of mechanical impact and shockwave applications, such as blast wave effect on the brain tissue and acceleration-induced pressure , which would cause the cavitation effect in the soft tissue of the brain, section 3.2.

Basically, research in this specfic field aims to provide investigation regarding such soft gels to replace diseased or damaged organs, or tissues that are defective or have been lost as a result of accidents or disease. In addition, The investigation and studies, themselves, accounts as a seperated important part that these materials are used to further address the properties and charactritics of soft tissue simulant materials. By this means, we can more precisely know the behavior of soft materials under different conditions, including high rate loading dynamic applications, and their response which is mainly complicated due to their nature labile properties and nonlinear elastcity. Furthermore, the uses of hydrogels have extended to cover a wide range of applications that include, but are not limited to, drug delivery, wound healing, ophthalmic materials and tissue engineering [105, 106].

Hydrogels are water-swollen polymeric three-dimensional networks, consisting of crosslinked hydrophilic polymers, which this specific ability to swell under biological conditions turns them into a great choice of materials for biomedical applications [107]. Such gels illustrate 3D network structure, which is physically or chemically crosslinked, allowing effective immobilization and release of active agents and biomolecules. Owing to their high water content, hydrogels resemble natural soft tissue more than any other

type of polymeric biomaterials [107]. Furthermore, these hydrogels are the favorites for scaffolds due to their biocompatibility (such as chitosan and alginate-based hydrogels) and high permeability [107], besides the fact that they are injectable and can be also formed via photopolymerization [108, 109]. There exist a hydrophilic moieties such as carboxyl, amide, amino and hydroxyl groups, dispread along the polymeric chain, which highly affects the high hydrophilicity of hydrogels [110]. In the state of swollen, these gels are soft and rubbery resembling highly precise living tissues.

The equilibrium swelling of the hydrogels highly depends on the osmotic driving forces, encouraging the entrance of water or biological fluids into the hydrophilic hydrogel matrix, and the cohesive forces exerted by the polymer strands within the hydrogel, besides the cohesive forces, which resist the material expansion and variation of such forces depends on crosslinking density [111]. Basically, the amount of water absorption by the hydrogels increases by increasing the hydrophilicity of forming polymer, which also results in lower gel swelling. When the hydrogels are in their dry forms are mainly referred to as "xerogels", while dry porous hydrogels gained by using drying techniques such as freeze-drying are called "aerogels" [111].

There are certain classifications of hydrogels, fundamentally divided into three major groups of natural, synthetic, and semi-synthetic gels. Mostly, the synthesization of the hydrogels is processed through the polymerization of vinyl or vinyl-activated monomers. Since the equilibrium swelling of such synthetic hydrogels varies widely based on the hydrophilicity of the monomers and the crosslinking density, a bi-functional monomer is usually added to carry out an in situ crosslinking reaction [110]. Natural hydrogels consist of natural polymers (polynucleotides, polypeptides, and polysaccharides), which these natural polymers are gained from various natural origins. For instance, collagen, which is obtained from mammals [110].

In order to enhance to the required physical and chemical properties, synthetic polymers are also used, which play an importrant role in some particular areas such as tissue engineering scaffolds, since they have the ability to be molecularly tailored with block structures, molecular weights, mechanical strength and biodegradability [112, 113, 114]. Basically, synthetic polymers utilized for synthetic groups of hydrogels are into three groups of nonbiodegradable[115, 116, 117], biodegradable[118, 119] and bioactive polymers [120, 121]. For such gels, due to their application as soft tissue simulants, it is essential to maintain physical and mechanical integrity. The hydrogels can strengthen by incorporating crosslinking agents, comonomers, and increasing the degree of crosslinking [105, 109].

There is an optimal level of crosslinking for nonbiodegradable hydrogels because too much crosslinking would lead to brittleness and less elasticity, in which the elasticity is a very important element for giving flexibility to the crosslinked chains, and to fa-

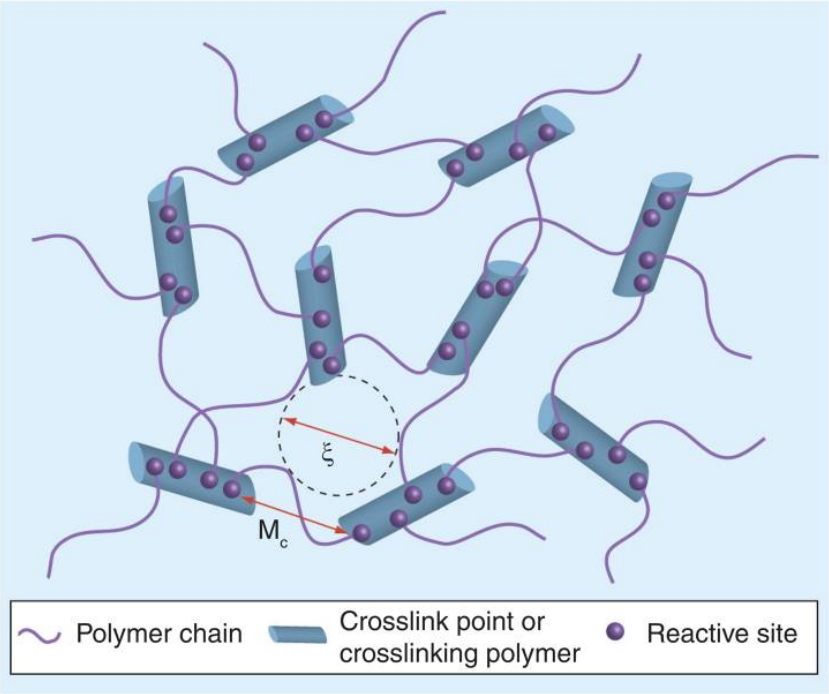

Figure 3.5: Schematic of hydrogel structure with hydrophilic polymer chains connected through crosslink points or crosslinking polymers [107]

cilitate the movement or diffusion of the incorporated bioactive agents [107]. Hence, a defined balance between mechanical strength and flexibility is crucial for such hydrogels. On the other hand, Biodegradability matters in the case of its rate which is important mainly when such gels are actively being used in tissue scaffolds and not just as tissue simulant in impact tests or other simulation studies. Many polymers created in nature are biodegradable, such as proteins, cellulose, starch, and chitin, but they are limited in making hydrogel scaffolds with tailored biodegradability and mechanical properties [107].

Most hydrogels used for soft tissue simulants or various biomedical applications are extracellular matrix (ECM)- based, filled with ECM molecules like proteins and proteoglycans. Agarose and collagen are the common hydrogels used for such purposes. It is desirable to build scaffolds to mimic the structure and bio-functions of the natural ECM [122, 123]. To date, numerous bioactive peptide sequences derived from ECM proteins such as fibronectin, laminin, and collagen, have been incorporated into synthetic hydrogels.

One of the challenges regarding such hydrogels is related to mehanical characteristics, which also depends on the type of tissue to be mimiced through the usage of gels. The hydrogel stiffness is accounted as one of the main parameters to control the mechanical

properties required for specific applications no the target tissue, in which the main parameter that play an essential role is the crosslinking density [110].

3.3.1 Agarose gel - preparation process

In this study, in order to investigate the transient dynamic behavior of brain tissue simulant material, agarose gel is utilized. Mainly, for such biomechanical applications related to direct or indirect impact-induced injury tests agarose and collagens as both natural and synthetic gels are considered. In addition, there have been studies, in which the tissue was simulated through the usage of natural materials such as bovine or swine tissue as in vivi and in vitro experiments, which are different concepts with respect to our experimental approach.

In similar cases to our approach toward the usage of soft mimicking materials protein gels and porcine as an example have been also widely used. Particularly, for dynamic experiments regarding the brain response to impact loading, gel materials are used as surrogates, especially collagen and agarose gels. Such gels are more convenient for handling and also for large quantity usage and more importantly, the versatile physical and mechanical properties of these soft materials would be an advantage, in which their concentration- dependant stiffness can turn them suitable for simulating the target tissue. The previous studies show that the mechanical properties of agarose gel with a concentration of about 0.2-0.6% are somehow close to that of brain tissues [27].

Traditionally, ballistic gels have been used as tissue simulant materials in a wide variety of impact tests, but the limitations of such gels are related to room temperature decomposition, translucence, and single-use behavior. In addition, the stiffness related to concentration of collagen is mainly higher with respect to the brain tissue and would be a better fit for the tissues with higher stiffness, such as aorta tissue [28]. Also unlike collagen, agarose samples can be readily prepared without pre-existing macro bubbles [28].

The agarose molecule is a linear polysaccharide consisting of β-1,3 linked D-galactose and α-1,4 linked 3,6 anhydro-αL-galactose residues [55]. When cooled from a homogeneous aqueous solution at 80-90 °C to a temperature below its gelation temperature (around 35 °C), it forms a three- dimensional network of physically cross-linked agarose fibers. Thermodynamically, this gelation involves a transformation from a random coil configuration in a sol state to a double helix in the initial stages.

We focus here on agarose gel which has a considerably wider range of stiffness than other gels like collagen. Generally, the stiffness of soft bio-materials covers a wide range, e.g., of 0.1 to 10 kPa for brain tissues [57, 58] or about 100 kPa for the human aorta [59].

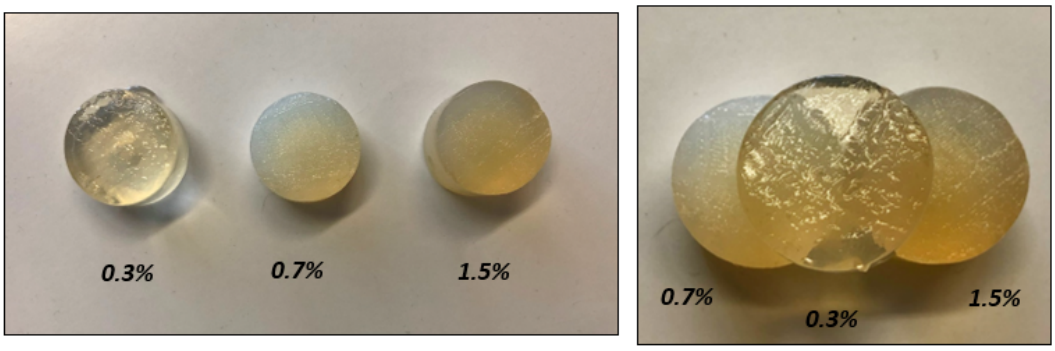

Figure 3.6: Agarose sample pieces of 0.3%, 0.7% and 1.5% (left), translucency difference of samples (right)

	shear modulus [kPa]	surface tension [N/m]	density [kg/m^3]	viscosity [m^{2}s^{-1}]
0.3% agarose gel	8	0.0072	1000	$8.81 \cdot 10^{-6}$
0.7% agarose gel	18.6	0.023	1070	$2 \cdot 10^{-5}$
1.5% agarose gel	39	0.075	1150	$4 \cdot 10^{-5}$

Table 3.3: Material properties for different gel concentrations

Because of its concentration-dependent stiffness, agarose can easily be tuned to mimic such different target tissues [28].

For this study, we prepared 21 specimens in 3 different concentrations of 0.3%, 0.7% and 1.5% bio-agarose gel (BIO-RAD, Certified biology agarose 1613101, Bio-Rad laboratories), i.e. each group contains of 7 samples. For 0.3%, 0.7% and 1.5% (g/ml) agarose specimens, see Figure 3.6, we added 100 ml of purified distilled water into a Pyrex beaker. Agarose powder was added slowly to avoid the formation of clusters, and mixed with distilled water by using a magnetic stir, while heated up to 80 degrees Celsius. Moreover, to compensate for evaporation, the weight of the samples was measured and water was added to regain the initial weight. After cooling, the mixtures were injected into the cuvettes by using a pipette. Then they were sealed tightly and cured for 10 hours, before testing. The full experimental approach will be discussed in the section 4.

3.4 Bubble dynamics

3.4.1 Theoretical background

The very first researchers that addressed bubble dynamics were Besant's (1859) [124] and Parson's (1893), however Lord Rayleigh (1917) proposed the most important mathematical model to describe the bubble dynamics. In this model, a spherical vapor bubble is assumed in an incompressible and inviscid fluid medium under constant external pressure, more than a pressure inside the bubble. In Besant model, we consider $\dot{R}$ as the velocity of the bubble wall, the radial velocity u of an incompressible liquid at position r can be described as:

$$u = \frac{R^2 \dot{R}}{r^2}, R \leq r < \infty. \tag{3.1}$$

The velocity potential of the liquid Φ is derived by integration over u:

$$\Phi = -\int_r^\infty u dr = -\frac{R^2 \dot{R}}{r^2}. \tag{3.2}$$

In order to gain a relation between the radial velocity and the pressure p_l in the liquid at position r, we can use the bernoulli theorem:

$$\frac{p_l - p_\infty}{\rho} = -\frac{\partial \Phi}{\partial t} - \frac{1}{2}u^2 = \frac{2R\dot{R}^2 + R^2\ddot{R}}{r} - \frac{1}{2}\frac{R^4\dot{R}^2}{r^4} \tag{3.3}$$

Here p_∞ and ρ are the pressure away from the bubble location and water density, respectively. By substituting R for r in equation 3.3 as the position next to the bubble boundary, which derives Besant fomula for an emty bubble:

$$R\ddot{R} + \frac{3}{2}\dot{R} = \frac{P_l - P_\infty}{\rho} \tag{3.4}$$

When the external pressure P_{ex} is applied to the system, then the remote pressure in the medium would be $P_\infty = P_0 + P_{ex}$, accounted as hydrostatic pressure.

In 1949, Plesset developed the model with the same assumptions but this time containing some amount of non-condensable gas and also considering surface tension and viscosity in his analysis, nowadays known as Rayleigh-Plesset equation [125]. Basically, Rayleigh–Plesset equation is a second-order nonlinear model for the radius change of a bubble in the fluid. Since this model exhibits most of the qualitative features of re-

fined models, it has been considered to be suitable enough to be used without further modifications. One of the essential assumptions in Rayleigh–Plesset equation is related to the incompressibility of the liquid medium, which in some cases is not adequate. Some authors already addressed this issue such as Herring's (1949), Gilmore's (1952) and Keller's (1956, 1980) [125].

In the an extention to Besant model, bubble is initially considered at equilibrium radius R_0 without external driving pressure and the pressure in the bubble P_b can be derived by the partial pressure of vapor P_v and gas pressure P_g:

$$P_b = P_g + P_v = P_0 + \frac{2\sigma}{R_0}. \tag{3.5}$$

The bubble will finally dissolve due to the excess pressure which is induced by the surface tension. If we consider the quasi.static pressure increase and also follow the polytropic law for the gas in the bubble, the gas pressure can be written as:

$$P_{gas} = P_g(\frac{R_0}{R})^{3k} = (P_0 + \frac{2\sigma}{R_0} - P_v)(\frac{R_0}{R})^{3k}. \tag{3.6}$$

With k being the polytropic exponent. Assuming constant vapor pressure, the pressure inside the bubble is derived as:

$$P_b = (P_0 + \frac{2\sigma}{R_0} - P_v)(\frac{R_0}{R})^{3k} + P_v. \tag{3.7}$$

The pressure at the bubble boundary P_l is the same as the pressure inside the bubble without surface tension term, so:

$$P_l = (P_0 + \frac{2\sigma}{R_0} - P_v)(\frac{R_0}{R})^{3k} + P_v - \frac{2\sigma}{R}. \tag{3.8}$$

Using equation 3.4:

$$R\ddot{R} + \frac{3}{2}\dot{R} = \frac{1}{\rho}[(P_0 + \frac{2\sigma}{R_0} - P_v)(\frac{R_0}{R})^{3k} + P_v - \frac{2\sigma}{R} - P_\infty] \tag{3.9}$$

Equation 3.9 was gained by Noltingk and Neppiras in 1950 [44]. Then it was extended by Poritsky [87] to account the effect of viscousity ν of water, which results in energy

dissipation term at the surface of the bubble:

$$R\ddot{R} + \frac{3}{2}\dot{R} = \frac{1}{\rho}[(P_0 + \frac{2\sigma}{R_0} - P_v)(\frac{R_0}{R})^{3k} + P_v - \frac{2\sigma}{R} - \frac{4\nu\dot{R}}{R} - P_\infty] \tag{3.10}$$

Equation 3.10 is typically known as the Rayleigh-Plesset or RPNNP (Rayleigh-Plesset-Noltingk-Neppiras-Poritsky) equation.

Since then the Rayleigh-Plesset model has been modified through different approaches in different applications by applying various assumptions, including primarily the compressibility of the liquid [126], generation of shock waves [127], transition from an isothermal to an adiabatic collapse, diffusion [128], chemical reactions [129], evaporation and condensation [130].

Herring [131] was one of the first researchers who slightly modified the plesset model on underwater explosions, where $P_\infty$is mainly considered constant and the effect of surface tension and viscosity are neglected. He considered an almost incompressible flow and constant density but the speed of sound is considered finite. Gilmore [132] contributed a slightly more general model, in which instead of considering the almost incompressible condition, he assumed general enthalpy functions $h(p) \neq \frac{P-P_\infty}{\rho}$ and varying sound speed with time. The main principle of Gilmore model is the usage of Kirkwood and Bethe hypothesis, which considered the local speed of sound [125].

Keller and Miksis [126] described the dynamics of an acoustically excited bubble in a slightly compressible medium by taking into account the small compressibility of the liquid, which affects the acoustic radiation [44]. This is particularly important for applications related to large amplitude oscillations. In this modification, the considerations would lead to smaller maximum amplitudes of the forced bubble.

In a slight modification given by parlitz et al. [133], the excitation pressure is given by a sinusoidal function with the specified frequency. Mainly the model follows as equation 3.10, and the driving term of $P_{ex}Sin(\omega t)$ is replaced to allow for arbitrary pressure functions fitted from pressure measurements in the experiments [44]. For such cases, the assumptions are: the constant spherical shape of a bubble, neglecting translational forces which are small enough, following ideal polytropic law for the gas inside the bubble, constant pressure (and vapor pressure) and temperature throughout inside the bubble, no gas diffusion or heat transfer in the bubble, small changes of density and compressibility of the medium and constant speed of sound in the liquid.

Through the applications in ultrasound contrast agent models in relation to microbubbles, De Jong [134] did experimental studies related to contrast agent and modeling by

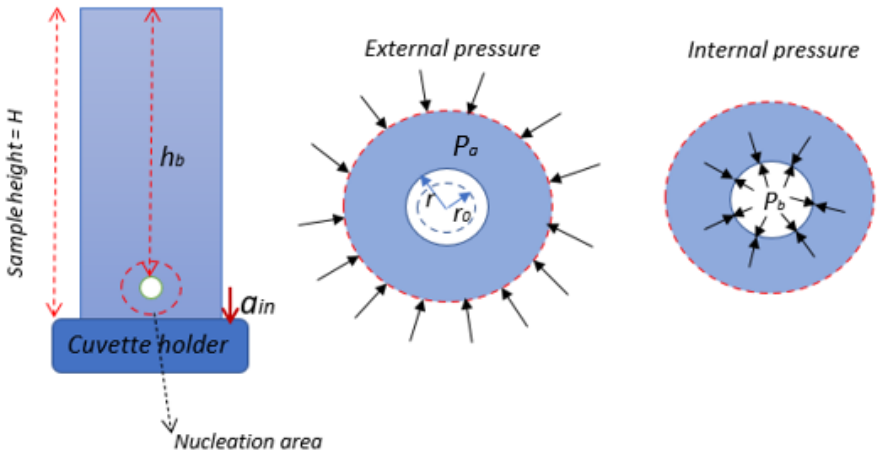

Figure 3.7: Schematic of a spherical cavitation bubble in a cuvette (left), pressure inside and outside the bubble (right)

their theoretical description of the vibration of a microbubble, considering shell elasticity, radiation and total damping and viscosity damping. This Rayleigh-Plesset based model was about the gas bubble in water and the bubble coated by albumin. Church [134] also derived equation from Rayleigh-Plesset model, accounted for the shell thickness and viscoelastic properties. In 2000, Hoff modified Church model through the usage of a linear model based on bulk properties of the particles and viscosity of polymeric material and considered air-filled microbubbles. In 2005 Chatterjee-Sarkar also modified the model, using Newtonian interfacial rheological in their model, which means that only viscous interfacial stresses are taken into account [135], and in 2008 Tsiglifis-Pelekasis derived a model, aimed to large acoustic pressures for microbubble and used both types of materials in Keller and Miksis equation and compare the results with a Kelvin-Voigt based model [135].

Depending on the nature of application almost all the models corresponds well for the slow expansion phase and the very begining stage of the collapse. It is still a serious limitation to accept the models during the final stages of collapse, due to the small bubble size and extremly high bubble wall velocities, which is significantly difficult for the high speed camers to capture with high precision.

3.4.2 Variational model of bubble growth

In this work, we consider soft, viscoelastic materials with large deformability. Such materials are, for example, biological tissues, gelatine, jelly, or agarose gels, which are often

used in the crash or ballistic experiments to replicate soft body parts. Their mechanical properties are at the boundary between the fluid and solid and they undergo large, rubbery, and often time-dependent deformations. By now their material behavior is not yet fully understood. In this study, we model the cavitation dynamics, particularly in agrose gel. Agarose is mainly considered to be stiffer than collagen and therefore can cover a wider range of material stiffnesses. In addition, agarose samples can be prepared without pre-existing macro bubble, turning the investigation suitable for bubble dynamics from the nucleation level [28].

In a limited recently developed models of bubble dynamics, related to soft biological and simulational biological materials, a viscoelastic medium with focus on Maxwell-based and Kelvin-Voit-based are mostly considered to extend the basic Rayleigh–Plesset model for spherical bubble. For instance, Gaurdron etal. developed a theoretical framework regarding spherical bubble dynamics, using strain-energy functions (Neo-Hookean, Mooney–Rivlin) [136]. Kang et al. also modified Rayleigh–Plesset equation by incorporating the Kelvin-Voigt and neo-Hookean models [28]. Fu et al. modified the work by Knowles and Jakub to model the time-dependent cavitation process in a hyperelastic material by taking the surface tension into account [137].

Here, we propose a variational model of bubble growth in soft gels and study it numerically and experimentally. The basic assumption is that the bubble is surrounded by an incompressible material so that it can be modeled like a hollow sphere, Figure 3.7. For the volume $V(r)$ at time t and a distance $r(t)$ from the bubble center, this immediately yields a relationship between bubble radius $R(t)$, bubble wall velocity $\dot{R}(t)$, and the radial velocity field $v(r,t) = \dot{r}$ in the material,

$$\frac{\mathrm{d}}{\mathrm{d}t}\left(\frac{4\pi}{3}(r^3 - R^3)\right) = 0 \quad \Rightarrow \quad \dot{r} = \frac{R^2\dot{R}}{r^2} = v(r,t)\,. \tag{3.11}$$

Substituting this relation into the momentum balance, integrating it, and taking into account the boundary conditions at the wall of a bubble in a liquid, leads to the Rayleigh-Plesset equation for bubble oscillations, [41]. Here, however, we follow the classic ideas of continuum thermodynamics in the sense of Truesdell & Noll [138], and we expect that in a deformation the contributing energy components compete with each other. The optimal internal process is the one that minimizes the system's total energy. This minimum energy leads to the equilibrium configuration in statics (assuming the existence of a stable equilibrium), and in dynamic processes it is generalized by Hamilton's variational principle of stationary action which states that of all possible trajectories the one with an optimal effect is chosen.

Thus, for the variational formulation of the bubble growth model, we postulate the existence of a free energy potential which contains, in addition to the energy of the

formation of a pore surface, the elastic deformation energy and, if necessary, a potential for inelastic deformations. For the time-dependent material equations, we require that they follow from a kinetic potential. In a fast deformation, part of the external work applied on the system results in an inertial effect with an additional kinetic energy. Because of the fast deformation, inertial effects with a kinetic energy compensate part of the rapidly applied external work. The action integral comprising the sum of all these contributions can then be optimized with respect to the bubble motion $\dot{R}(t)$. As a result we obtain in the case of a viscoelastic gel-like material an ordinary differential equation which can be used to calculate (numerically) the bubble size $r(t)$. Additional terms may arise, for example, when considering mass diffusion, thermal effects or, most relevant in this context, material damage.

To derive the constitutive model for cavitation in gel, we first consider the deformation and summarize the relevant energy contributions. The energy optimization then yields the differential equation we are looking for for the bubble motion.

3.4.3 Kinematics of the deformation

Our basic model is a spherically symmetric cavity or bubble surrounded by a thick layer of gel material. The bubble has the radius R_0 or $R(t)$ in the reference or the current configuration, respectively, and it is loaded by uniform tension p_z at the outer side with radius b_0 or $b(t)$, see Figure 3.8. Under the assumption of a volume-preserving deformation, the motion from the original radius $r_0 \in [R_0, b_0]$ to the current radius $r \in [R, b]$ is uniquely described by

$$r(t) = \left(r_0^3 - R_0^3 + R(t)^3\right)^{1/3} . \tag{3.12}$$

We consider the change of the sphere circumference at R, and write for the tangential stretch

$$\lambda = \frac{r}{r_0} . \tag{3.13}$$

For the change of a line element in radial direction we know only that

$$\lambda_r = \frac{\mathrm{d}r}{\mathrm{d}r_0} , \tag{3.14}$$

but because we consider the material to be incompressible, $\lambda_R = \lambda^{-2}$ applies. It follows $r^2\,\mathrm{d}r = {r_0}^2\,\mathrm{d}r_0$ and by integration we get $r^3 = {r_0}^3 + c$. The constant results from the volume constraint to $c = R^3 - R_0^3$. This gives us the tangential stretch (3.13) as a

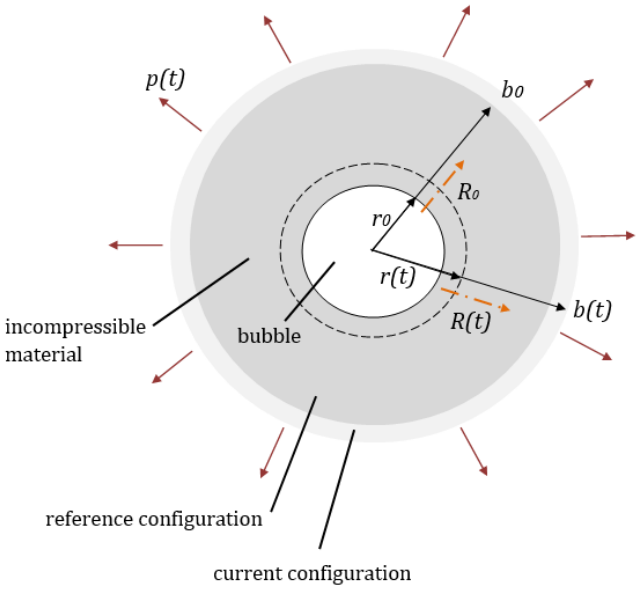

Figure 3.8: Spherical symmetric model of a bubble with inner radius R_0, R and outer radius b_0, b in the initial and the current configuration

function of the current radius, $\lambda(r)$,

$$\lambda = \left(1 - \frac{c}{r^3}\right)^{-1/3} \qquad \text{with} \quad c = R^3 - R_0^3\,, \tag{3.15}$$

or vice versa, the instantaneous radius as a function of the stretches, $r(\lambda)$. For further calculations we deduce its derivative,

$$\frac{\partial \lambda}{\partial r} \equiv \lambda' = (1 - \lambda^3)\frac{\lambda}{r} \qquad \text{and} \qquad \frac{\lambda^3}{r^3} = -\frac{1 - \lambda^3}{c}\,. \tag{3.16}$$

Summarizing we state that for a hollow sphere with incompressible material, the deformation is completely described by the cavity radius $R(t)$, the stretch $\lambda(r,t)$, and by its rate of change, $\dot{\lambda}(r,t)$. Additionally, a non-local dependence of λ' may apply. Therefore, the domain of the constitutive equations for bubble growth, i.e. the state space $\mathcal{Z}$, reduces to

$$\mathcal{Z} = \{R, \lambda, \dot{\lambda}, \lambda'; T\} \quad \Rightarrow \quad \dot{R} = \dot{R}(\mathcal{Z}). \tag{3.17}$$

Here T is the absolute temperature, which stands for possible additional external fields.

3.4.4 Elastic energy density

The elastic material response is characterized by the strain energy density Ψ as a function of the deformation gradient $\mathcal{F}$ or, more precisely, the deformation tensor $\mathcal{F}^T\mathcal{F}$. The nominal stress tensor follows from the differential, $\mathcal{P} = \partial_{\mathcal{F}}\Psi$, and by transforming it to the current configuration, the actual stresses $\boldsymbol{\sigma} = \mathcal{P}\mathcal{F}^T \det \mathcal{F}$ is obtained. We remark that $\det \mathcal{F} = 1$.

The invariants of the deformation tensor $\mathcal{F}^T\mathcal{F}$ can now be formulated with the stretches (3.13) and (3.14),

$$I_1 = 2\lambda^2 + \lambda^{-4} \qquad \text{and} \qquad I_2 = \lambda^4 + 2\lambda^{-2}, \tag{3.18}$$

and $I_3 = 1$. In the simplest case, we assume that the gel can be described with one elastic modulus μ. This corresponds to a Neo-Hookean material model with strain energy density

$$\Psi = \frac{\mu}{2}\left(I_1 - 3\right) = \frac{\mu}{2}\left(\lambda^2 + \lambda^{-4} - 3\right) . \tag{3.19}$$

If we want to weight both invariants with material module, then we obtain the energy density of the Mooney-Rivlin material model,

$$\Psi = \frac{\mu_1}{2}\left(I_1 - 3\right) - \frac{\mu_2}{2}\left(I_2 - 3\right) = \frac{\mu}{2}\left((k-1)\left(\lambda^2 + \lambda^{-4} - 3\right) + k\left(\lambda^4 + 2\lambda^{-2} - 3\right)\right) , \tag{3.20}$$

where we set $\mu_1 = (1-k)\mu$ and $\mu_2 = -k\mu$. For $k = 0$, Eq. (3.20) obviously corresponds to the Neo-Hookean model. More generally, the Ogden material model formulated in the principal stretches can also be stated. However, a meaningful adaption of the corresponding material parameter is hardly possible here and so we stay with the two basic models.

3.4.5 Variational form

According to the ideas of classical continuum thermodynamics [138], we expect that in a deformation the energy contributions compete with each other, and the actual internal process is the one that optimizes the action. The action is the time integral over the Lagrangian function $L = K - \Pi$, with kinetic energy K and potential energy Π, and Hamilton's variational principle of stationary action states that of all possible trajectories, the one with

$$\int_{t_1}^{t_2} L \,\mathrm{d}t \to \text{optimum} \tag{3.21}$$

is chosen. For (3.21) it follows that the derivative must become zero, which leads to $\dot{L} = 0$ and to the Lagrangian equations of second kind. In the presence of dissipative processes, however, an energy rate remains. Let it be described here by a Rayleigh dissipation potential $-\Phi$. Thus, the current energy change is $\dot{L} = -\Phi$ and the optimal motion is consequently the one which optimizes its difference. The sought constitutive equation for the bubble size thus provides the principle of maximum dissipation,

$$\frac{\mathrm{d}}{\mathrm{d}\dot{R}}\left[\dot{L} + \Phi\right] = 0\,. \tag{3.22}$$

For a time-dependent elastic gel material, we assume the following energy contributions.

The surface of a bubble with radius $R(t)$ has the energy

$$S(R) = 4\pi R^2 \gamma_0 \tag{3.23}$$

where γ_0 is the surface energy per undeformed unit area. Initially, at radius r_0, the bubble is filled with some amount of gas with partial pressure $p_{\mathrm{G}0}$. We assume an isentropic change of state with exponent κ and $p_{\mathrm{G}} V^{\kappa} = \text{constant}$. Then, the work of volume change is determined by

$$W_{\mathrm{G}} = \frac{p_{\mathrm{G}0}}{\kappa - 1}\frac{4\pi R_0^3}{3}\left[\left(\frac{R_0^3}{R^3}\right)^{\kappa-1} - 1\right]. \tag{3.24}$$

The elasticity of the material can be described with the models from Section 3.4.4 and, by integrating over the volume of the hollow sphere, we calculate here its elastic energy. For the Neo-Hookean model (3.19) we obtain

$$\begin{aligned} W^e(R) = \int_V \Psi \,\mathrm{d}V &\overset{(3.19)}{=} 4\pi \int_{\lambda(b)}^{\lambda(R)} \frac{\mu}{2}\left(2\lambda^2 + \lambda^{-4} - 3\right)\frac{c\lambda^2}{(\lambda^3 - 1)^2}\,\mathrm{d}\lambda \\ &= 2\pi\mu(R^3 - R_0^3)\left[-\frac{2\lambda^2 + 2\lambda + 1}{\lambda^3 + \lambda^2 + \lambda}\right]_{\lambda(b)}^{\lambda(R)}. \end{aligned} \tag{3.25}$$

With $\lambda(R) = {}^{R}\!/_{R_0}$ and $\lambda(b) = {}^{b}\!/_{b_0}$ this gives the energy

$$W^e(R) = 2\pi\mu(R^3 - R_0^3)\left(\frac{R^2}{R^2 + R\,R_0 + R_0^2} - \frac{R_0}{R} - \frac{b^2}{b^2 + b\,b_0 - b_0^2} + \frac{b_0}{b}\right) \tag{3.26}$$

where b abbreviates $b(r) = (b_0^3 - R_0^3 + R^3)^{1/3}$. However, usually it is $b \approx b_0$ so the expression (3.25) simplifies. For Mooney-Rivlin material the corresponding calculation

leads to

$$W^e(R) = 2\pi\mu \left((k-1) \left(2R^3 - 2R^2 R_0 + \frac{R_0^4}{R} - R_0^3 \right) + k \left(\frac{R^4}{R_0} - \frac{2}{3} r^3 - 2R_0^2 R + \frac{5}{3} R_0^3 \right) \right) . \tag{3.27}$$

To account for the time dependence of local deformation we consider the evolution of radial stretch $\mathrm{d}\lambda_r / \mathrm{d}t$, denote it as effective rate of stretch $\dot{\lambda}$, and calculate it from the radial velocity (3.11).

$$\dot{\lambda} = \left| \frac{\partial \dot{r}}{\partial r} \right| = \frac{2R^2}{r^3} |\dot{R}| \tag{3.28}$$

Let the effective current stress σ in the material depend on the stretch rate $\dot{\lambda}$, e.g. by means of power law $\sigma \propto \dot{\lambda}^m$. We choose $m = 1$, and define a quadratic (conjugate) rate potential per unit volume,

$$\psi^*(\dot{\lambda}) = \frac{1}{2} \eta \dot{\lambda}^2 , \tag{3.29}$$

with the kinematic viscosity constant η as the product of dynamic viscosity constant ν_0 and mass density ρ_0 of the material, $\eta = \nu_0 \rho_0$. We can now integrate this rate potential for the hollow sphere.

$$\begin{aligned} \Phi(\dot{R}, R) &= \int_R^b \psi^*(\dot{\lambda}(\dot{R}, R)) \, \mathrm{d}r \\ &= \eta \int_R^b \left(\frac{2R^2 |\dot{R}|}{r^3} \right)^2 2\pi r^2 \, \mathrm{d}r = 2\nu_0 \rho_0 \frac{4\pi R^3}{3} \left(\frac{\dot{R}}{R} \right)^2 \left(1 - \frac{R^3}{b^3} \right) \end{aligned} \tag{3.30}$$

The rate potential $\Phi(\dot{R}, R)$ describes a change in energy.

In the same way, the radial velocity (3.11) is used to determine the kinetic energy of an expanding hollow sphere.

$$\begin{aligned} K(R, \dot{R}) &= \int_R^b \frac{1}{2} \rho_0 \, v_r^2 \, 4\pi r^2 \, \mathrm{d}r \\ &= \int_R^b \frac{1}{2} \rho_0 \left(\frac{2R^2 \dot{R}}{r^2} \right)^2 4\pi r^2 \, \mathrm{d}r = 2\pi \rho_0 \, R^4 \left(\frac{1}{R} - \frac{1}{b} \right) \dot{R}^2 \end{aligned} \tag{3.31}$$

The mechanical work applied by a (positive or negative) pressure $p(t)$ results in the

power

$$P(\dot{R}, R) = p(t)\frac{\mathrm{d}}{\mathrm{d}t}\left(\frac{4\pi}{3}b^3\right) = p(t)\,4\pi R^2\dot{R}. \tag{3.32}$$

Here we tacitly assume p to be the difference between the applied remote pressure p_∞ and a bubble vapor pressure p_V.

3.4.6 Constitutive equation

With the assembled terms, we now formulate Hamilton's principle. For this, we need the derivatives with respect to the bubble size r for the contributions (3.23) - (3.31). They are given in the appendix. From (3.22) then follows

$$\frac{\partial S}{\partial R} + \frac{\partial W_\mathrm{G}}{\partial R} + \frac{\partial W^e}{\partial R} - \frac{\partial K}{\partial R} + \frac{\mathrm{d}}{\mathrm{d}t}\frac{\partial K}{\partial \dot{R}} + \frac{\partial \Phi}{\partial \dot{R}} = \frac{\partial P}{\partial \dot{R}}\,. \tag{3.33}$$

If we now assume that the ratio R/b is negligibly small, then the time-dependent terms simplify. After some algebraic manipulations we obtain the differential equation of bubble motion:

$$\begin{aligned}\frac{2\gamma_0}{\varrho_0 R} + \frac{\mu(1-k)}{\varrho_0}\left(\frac{5}{2} - \frac{2R_0}{R} - \frac{R_0^4}{2R^4}\right) + \frac{\mu k}{\varrho_0}\left(\frac{4R}{R_0} - \frac{2R_0^2}{R^2} - 2\right)\\ + \frac{3}{2}\dot{R}^2 + R\ddot{R} + \frac{4}{3}\frac{\nu_0}{R}\dot{R} = \frac{p(t)}{\varrho_0} + \frac{p_{\mathrm{G}0}}{\varrho_0}\frac{R_0^{3\kappa}}{R^{3\kappa}}\end{aligned} \tag{3.34}$$

This constitutive equation extends the classical Rayleigh-Plesset equation by elastic and non-local terms. It comprises several specific cases. For example, dropping the time-dependent expressions and setting $\gamma_0 = 0$, $p_{\mathrm{G}0} = 0$, and $k = 0$, it reduces to the classical solution for static cavitation [139] or, with $\gamma_0 \neq 0$ again, we can deduce a critical bubble nucleation size [140]. We remark that energy contributions of additional fields can be added easily.

4 Experimental investigation on cavitation

In this chapter the full experimental approach regarding implementation of drop tower test is described and the outcome including the cavitation nucleation and bubble growth in agarose gel samples are presented. The essential parts of this chapter is already submitted for publication by us, in [141].

4.1 Experimental approach on bubble dynamics

The generation methods used for the onset of cavitation are versatile. Mostly in the recent attempts, the shock wave originated and progressed by laser light, heat, electrical sparks and even chemical explosions. Moreover, some groups use the sound field setups, known as acoustic cavitation. In addition to the mentioned methods, there are a few methods to counter the simulation of impact during the process of test. Split Hopkinson Pressure Bar test (SHPB) has been used for dynamic impact tests to characterize materials in compression for rates from 10^2 to 10^5 1/s. Other methods such as torsional resonator testing [21], atomic force microscopy (AFM) and rheological-based testing have been developed to ascertain the dynamic behavior of soft biological materials [28]. By using such methods, there exist a good chance to test a wide range of fluidic and solid materials and biological tissues in vivo. However, the lack of the ability to impart high-rate loading and the direct observation of the tested samples during impact besides the requirement of direct contact between soft material and loading frame [28], lead us to use the drop tower method for measuring the soft agarose samples at high strain rates.

The cavitation generation method depends on the nature of the investigation. Depending on the area of causing the bubble nucleation we can design different concepts. However, using different methods should still cause the same change in the stress field in the medium where the cavitation is expected to happen. In the acoustic method periodic high-frequency acoustic waves are used to create cycles of compression and tension as a result of its positive and negative phases, respectively [65]. Cavitation bubbles are generated through the negative portion of the cycle, where the acoustic wave reaches its maximum amplitude and collapse in the positive portion of the cycle. This process is

often accompanied by the mechanism of rectified diffusion, resulting in diffusion of gases into the bubbles, which diminishes the apparent tensile strength [65].

In most of the generation methods, tensile loading plays an essential role. Chesterman [143] described a dynamic method known as the Tube-Arrest method (T-A), which generates direct tensile loading on a column confined in a tube as a result of an arrest in its motion. A tube containing the fluid is placed vertically and connected to the springs in a way that, when stretched and suddenly released, the tube and fluid are affected by the rapid and harsh upward velocity, in which the impact of the tube with the fixed stop on the upward path would arrest of the tube motion. After impact, the upward motion of the fluid column generates a tensile wave that is propagated to the bottom of the tube where cavitation is generated [65]. This method is addressed in more details in the work of Hansson et al. [144], Overton et al. [145], and Williams et al. [147]. Chesterman utilized distilled water in a glass tube with various velocities to study the effect on cavitation cluster dynamics as opposed to its generation and Hansson completed that experimental effort by adding a methematical model for the formation of the clusters, while Overton developed the method by using a piezoelectric transducer in a cylindrical rubber block forming the base of the tube to measure pressure, and reported the apparent cavitation thresholds of negative 0.178, 0.189, 0.203 MPa for degassed fresh tap-water, deionized water, and sea-water [65].

Another dynamic method is known as Bullet-Piston (B-P) method causing cavitation as a result of a tensile reflection of a generated compressive pulse [148]. A fluid-filled tube is mounted vertically with a free upper-end exposed to the atmosphere and the bottom-end closed by a sliding-fit position rod. A bullet impact causes a compressive pulse at the open end of the piston rod, which propagates into the fluid column and then reflects in tension at the fluid-atmosphere interface as a result of the lower acoustic impedance of the air compared to the fluid. This reflected wave depends on the amount of tension that the fluid medium can resist, known as the apparent tensile strength of the fluid (plateauing) [65]. This method is also described more deeply in the works of Couzen et al. [149], Sedgewick et al. [150].

Split Hopkinson pressure bar (SHPB) test has been one of the important methods for impact-induced and shock wave propagated test methods used for onset of cavitation. Mainly this particular generation method is ideal regarding simulation of the blast wave, causing the bubble nucleation and growth, although there is a possibility of modification of SHPB test for variations in test setup and for instance turn into pressure wave input or direct impact on the sample by removing the transmission bar and just using the incident bar, in which the sample is attached to it. Same as B-P method is the modified SHPB test known as the fluid-Hopkinson bar method developed by Kenner [151] including of vertically placed tube with a fluid column, but this time instead of a short piston rod, a longer rod was utilized. The advantage of using a longer rod is related to

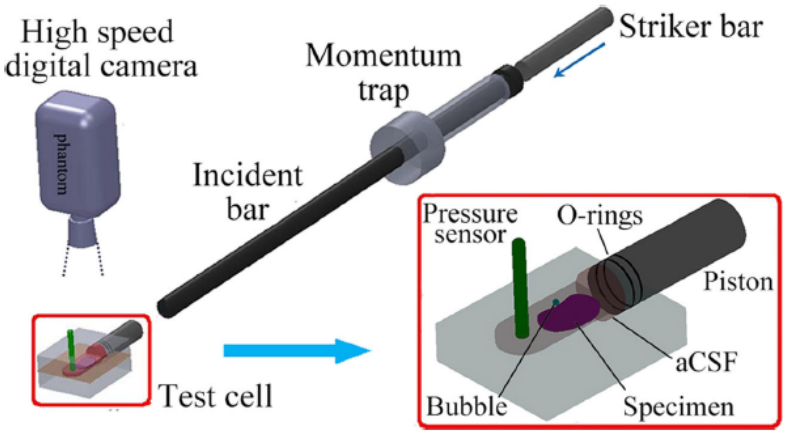

Figure 4.1: Modified SHPB test setup inclduing chamber for single bubble growth [27]

allowance for the generation of a compressive pulse without multiple cycles of reflections in B-P method, which was described by Overton[145]. In this method, the same concept of plateauing of the reflection magnitude used in B-P method was observed and the compressive pulse shape was shaped by way of a spherical striker launched by a gas gun and the use of a pulse shaper and loading rod [65].

As fully described in the second chapter, mainly metallic bars are used in SHPB test setups and one essential requirement regarding such high-rate loading test is related to acoustic impedance. When it comes to testing soft tissue simulant materials, metallic bars are not well-suited due to the significant acoustic impedance differences and are mainly changed to polymeric bars such as nylon or PMMA bars. In some studies, related to TBI-impact simulation tests, such polymeric bars in SHPB setups were used for shockwave simulation, such as blast-induced cavitation. In many of the studies, swine or bovine tissue was used as the direct dynamic behavior of tissue, and in a few cases, the cadaver material was utilized for such high-strain rate loading experiments.

Particularly, soft gels such as agarose and collagen have been targeted as soft tissue simulant in order to study their dynamic mechanical behavior in impact-induced experiments mainly in SHPB and drop tower tests. For instance, Hong et al. [27]. investigated the localized tissue surrogate deformation by cavitation and in order to do so they modified the SHPB setup to test agarose gel samples (0.4%- 0.6%), see Figure 4.1. In that study, single bubbles were placed in the gel medium and the effect of shockwave and pressure input through the bars on the samples were investigated by analyzing the bubble growth in underpressure and overpressure conditions. In addition, Hopfes group [29] modified the SHPB test and used the shock tube to generate pressure waves for cavitation studies.

4.2 Drop tower test

In this work, drop tower test is used to investigate the dynamic response of the soft tissue simulated material, in this case agarose gel, under high-rate loading impact test. In addition to SHPB test, which was fully described as for its conventional and modified setup, other methods such as torsional resonator testing [66], atomic force microscopy (ATM) [67] and rheological-based testing [48] have been developed to ascertain the dynamic behavior of soft biological materials. Using such methods gives a good chance to test a wide range of soft fluidic and solid materials. However, the lack of the ability to impart high-rate loading and the direct observation of the tested samples during impact limits their potential for cavitation experiments. Kang et al.[49] modfied the conventional drop tower test into an integrated system to adapt the experiment for cavitation test and capturing the bubble formation and growth by high-speed camera. In their study, Kang group worked on water, collagen and agarose gels in drop tower test and through that they simulated the acceleration-induced cavitation in soft materials.

Fundamentally, as stated earlier, cavitation occures due to the sudden change of the local pressure and during this work we are investigating the impact-induced cavitation, in which by implementing drop tower test and simulating impact effect on the gel as soft tissue simulant we will derive the bubble growth size through the usage of high-speed camera and diduce the range of cavitation pressure in agarose gel. Here comes another advantage of drop twoer test, which is the ability to investigate the cavitation in soft materials, correlating them to other physical parameters [49]. In our test, a different physical parameter, acceleration and its rate of change related to the generation of bubbles in agarose gel is used, which is not possible with other generations methods such as lasers or ultrasound. This can specifically be useful in the study of injury biomechanics where force, accelerations, and material properties are key physical parameters [49].

As fully described in section 3, we prepared 21 specimens in 3 different concentrations of 0.3%, 0.7% and 1.5% bio-agarose gel (BIO-RAD, Certified biology agarose 1613101, Bio-Rad laboratories), i.e. each group contains of 7 samples. For 0.3%, 0.7% and 1.5% (g/ml) agarose specimens, we added 100 ml of purified distilled water into a Pyrex beaker. Agarose powder was added slowly to avoid the formation of clusters, and mixed with distilled water by using a magnetic stir, while heated up to 80 degrees Celsius. Moreover, to compensate evaporation, the weight of the samples was measured and water was added to regain the initial weight. After cooling, the mixtures were injected into the cuvettes by using a pipette. Then they were sealed tightly and cured for 10 hours, before testing.

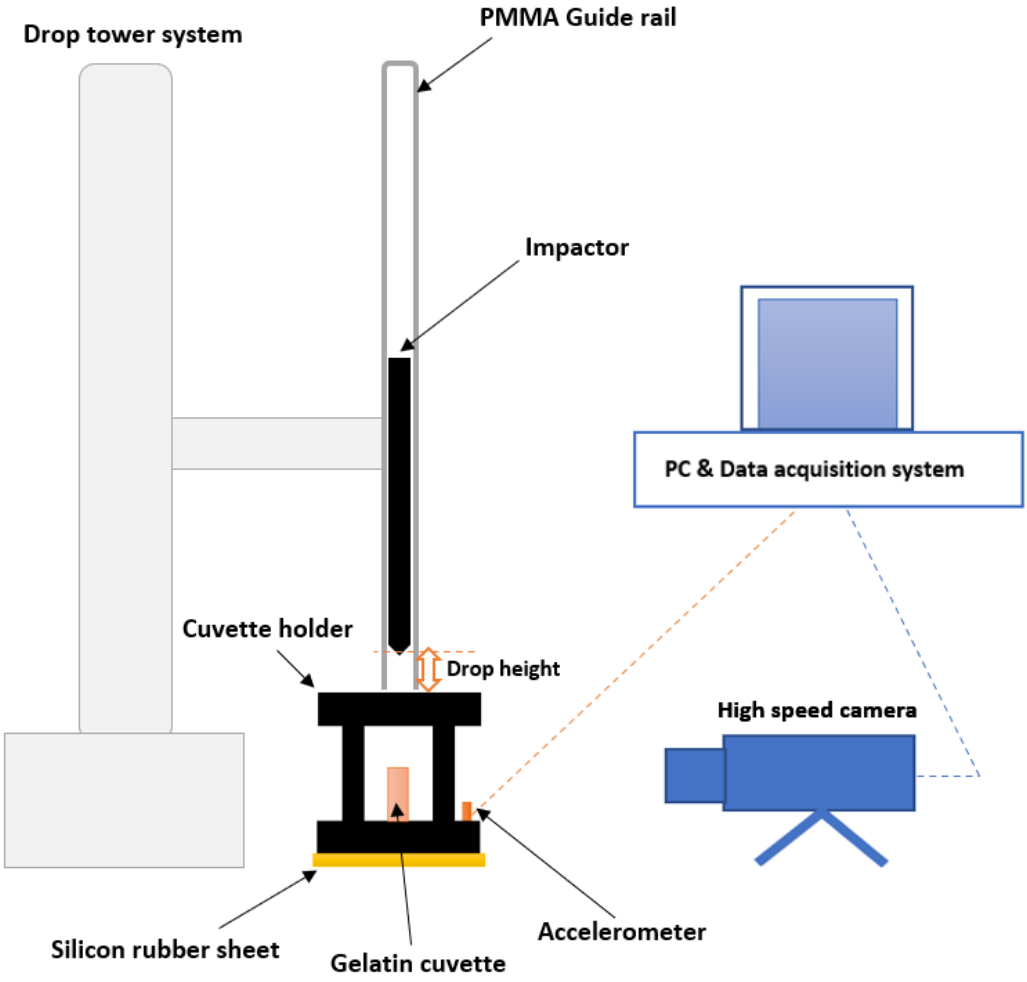

Figure 4.2: Schematic drop tower test setup: The bubble growth is recorded with a high speed camera while the 1.8 kg impactor hits the cuvette holder from the minimum drop height of $h_d = 100 - 300\,\mathrm{mm}$.

	elastic modulus [kPa]	tensile strength [kPa]	mass density [kg/m^3]
silicone rubber	100	1926	845

Table 4.1: Properties of the silicone rubber sheet XE-0700-ALVEO [146]

Our test setup consists of a conventional drop tower impact system, the gel sample cuvette, a cuvette holder, an accelerometer, the data acquisition system and a high speed camera, see Figure 4.2. The agarose gel samples were prepared inside standard plastic cuvettes, as explained above, sealed with a cap and then glued onto the cuvette holder using 5-min epoxy. The holder consists of two horizontal plates connected by four vertical columns; it is made of mild steel to be rigid enough to tolerate the impact from the impactor striker, being made also from mild steel. The cuvette holder's mass is 8.3 kg; the impactor weighs 1.88 kg. The precise calibration is implemented before each drop attempt, by checking the perpendicular position of the PMMA tube, where the impactor strikes onto the cuvette holder upper surface. In addition, as the first step the centre of the upper surface of the cuvette holder, where the impactor ought to land, was marked and the laser technique was used to ensure that tip of the impactor is aligned on the marked spot. In addition, a soft silicon sheet with a thickness of 14 mm is placed at the bottom of the cuvette holder to allow for a certain downward movement of the designed setup, see Figure 4.3.

A HBM Data acquisition system is employed for measurement, in connection with an ICP based accelerometer (KISTLER-Quarz 8044), in which the data are acquired at a rate of 90 kHz.

In the current modification of drop tower setup, rubber sheet foam plays a vital role, emphasisyng the downward movement of the cuvette and cuvette holder and the acceleration which is effected by that. Figure (4.4) illustrates the schematic free body diagram of the test system, in which the movavle block presents the cuvette holder (m), a linear spring (k) and a damper (c), which represents the rubber sheet. When the impactor is released from a certain drop height, h_d, it would be in a state of free fall toward cuvette holder, m, until it initiate the impact contact with the surface of cuvette holder, which is initially stationary on the rigid surface (reference surface). It should be noted that impactor and cuvette holder move only in vertical exis, since the movement of the impactor is constrained by the PMMA guide rail and the impactor and cuvette holder are calibrated for alignement in a way that impactor hits the vertical symetry axis of the cuvette holder, m. Furthermore, our focus is mainly concerns on the transient dynamic response of defined setup, since the mechanical loading occures in the inital impact of impactor and cuvette holder. In this regard, the dynamics of the setup can be divided into four main phases of contact and seperation as follows; $phase1$: m and reference sur-

face in contact through rubber sheet, while the impactore and m are in direct contact, *phase*2: while there is a contact between impactore and m, there is a seperation between m and rubber sheet, *phase*3: contact between m and rubber sheet but seperation between m and impactor, *phase*4: seperation between all the elements until total stopage of movements. Table (4.1) shows the physical and mechanical properties of used rubber foam sheets.

For our study, we initially determined the critical acceleration a_c that induces bubble nucleation. A series of impact tests from a low drop height, starting with 50 mm, was conducted. The drops were repeated on the same agarose sample with incrementally increasing height until cavitating bubbles were observed. The onset of cavitation was captured with a high speed camera video (Photron Fastcam SA3), at a rate of 20 000 fps. It should be noted that the nucleation and the related radius of the bubble are detected by the high speed camera and, hence, the captured minimum radius means the minimun size visible to the camera. Since the cavitation can damage the tested agarose gel, which could alter the intrinsic cavitation response, the sample was replaced with a new one whenever cavitation was observed.

The relation between the impactor drop height, h_d, and the resulting acceleration is shown in Fig 4.5. Here and in the following we plot the normalized acceleration $\bar{a}$ with $a = \bar{a}g$ where g is the gravitational constant. As expected, an increase of the drop height results in a higher acceleration. For the experiments of Section 4.3, the minimum drop height to induce cavitation was used for each agarose concentration.

4.3 Cavitation test results

We performed the drop tower test for all 21 prepared agarose samples using the minimum drop hight of the corresponding agarose concentration. The bubble nucleation was captured by our high-speed camera with 20 000 fps. Then, the images were analyzed with the ImageJ software [152]. The radius of each bubble was calculated from the projected area, $R = \sqrt{A/\pi}$, using the threshold method.

Figure 4.6 shows a typical result for the 0.3% agarose gel. The different steps of the recorded cavitation, from the bubble nucleation, growth and final collapse can be observed. The first frame shows the time, $\Delta t = 0.05$ ms per frame, and is recorded before the steel impactor hits the cuvette holder. No bubble was optically detected until frame 3, in which a bubble nucleates. From frame 4 to 7 the bubble grows, whereby Frame 7 shows the maximum bubble size. Then, from Frame 8 to 11 the bubble radius decreases until, in Frame 12, the bubble collapses entirely. Figures 4.7 and 4.8 also show the frame photographs of bubble nucleation, growth and collapse of 0.7% and 1.5%.

The primary signal we measured in our drop tower test is the acceleration $a(t)$. A typical history is shown in Figure 4.9 where also the significant steps of bubble growth are

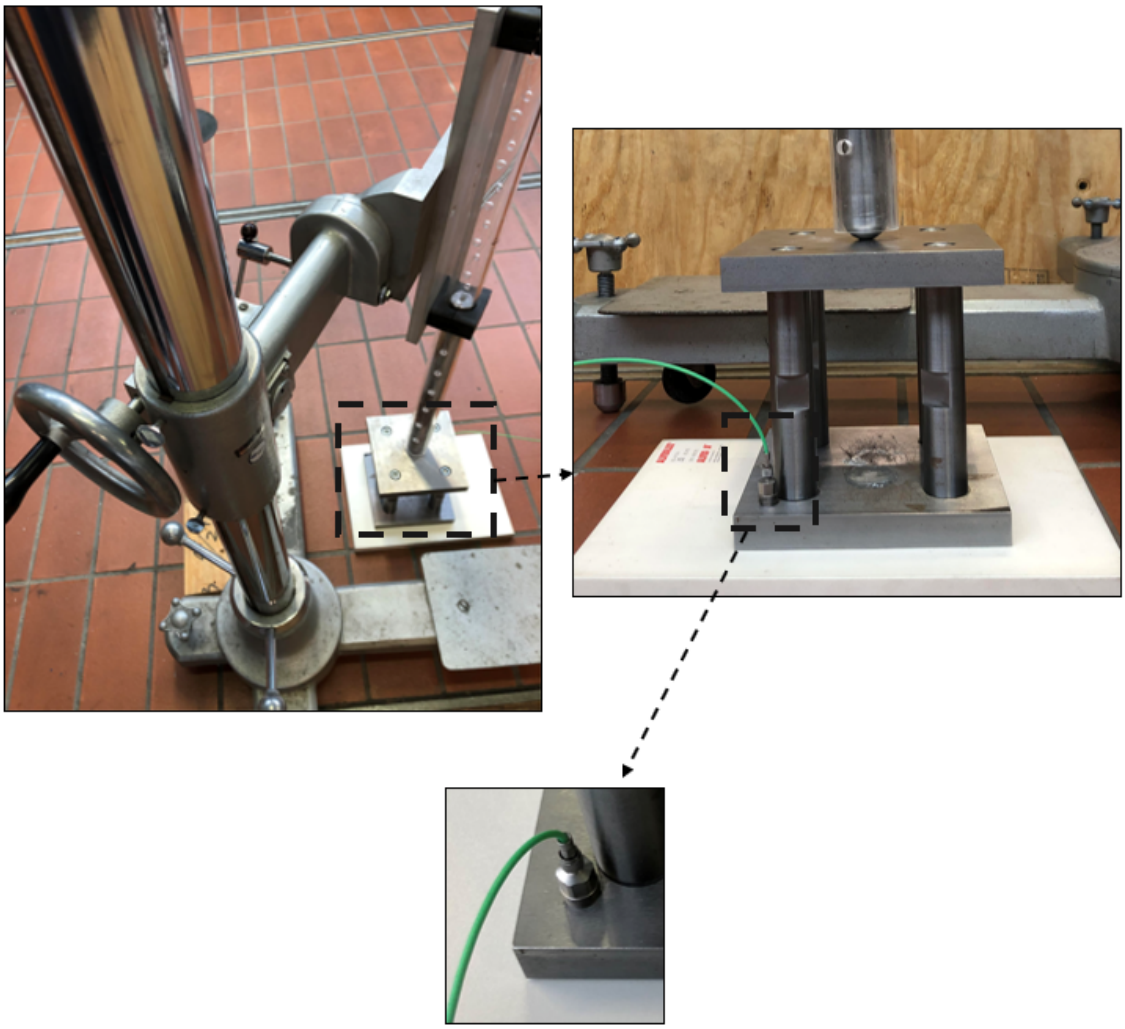

Figure 4.3: Setup of the drop tower test indicating the position of the accelerometer on the lower side of the cuvette holder.

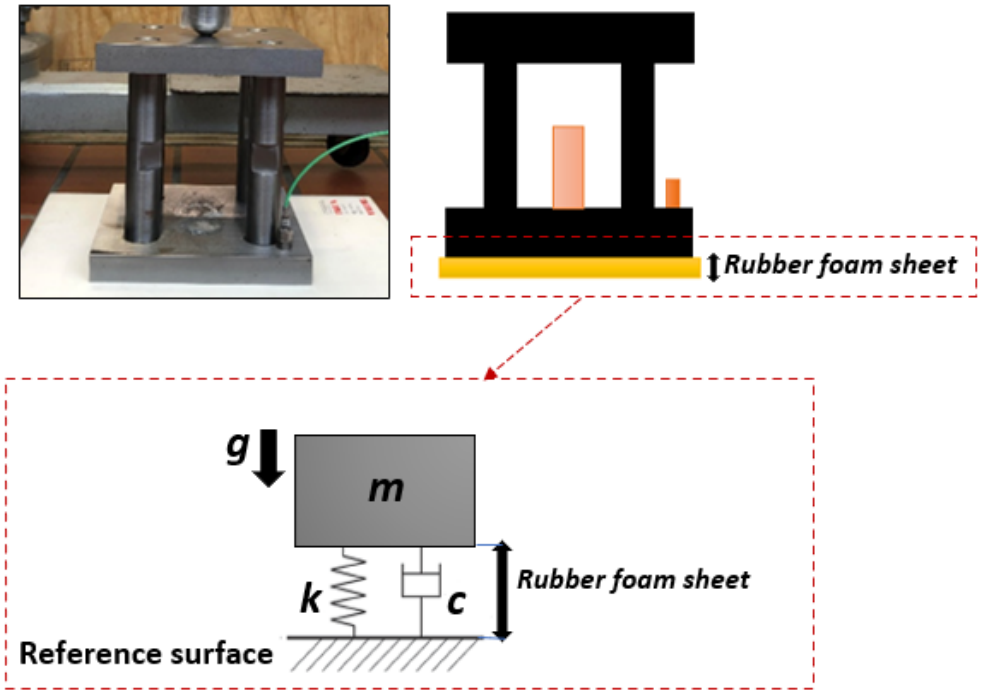

Figure 4.4: A free body diagram of drop tower test indicating the role of the rubber sheet foam.

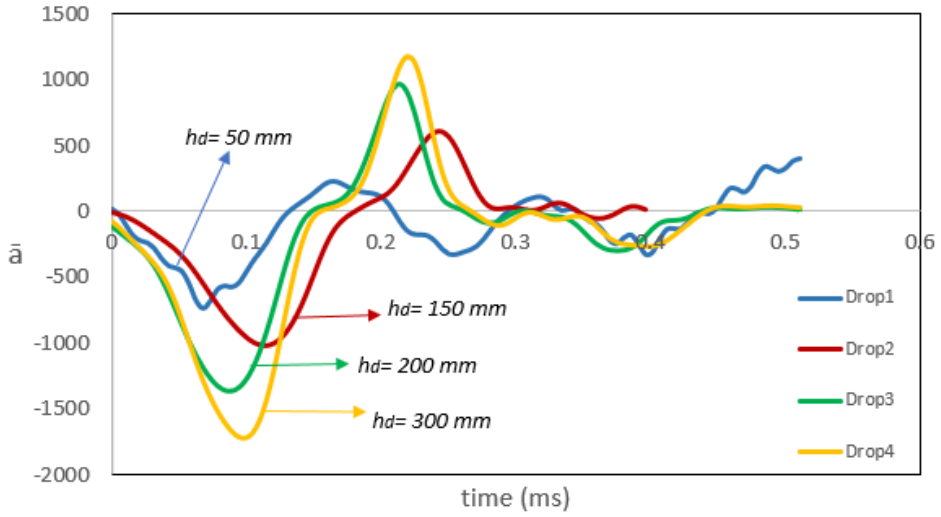

Figure 4.5: Acceleration profile $\bar{a} = a/g$ over time for different drop heights h_d

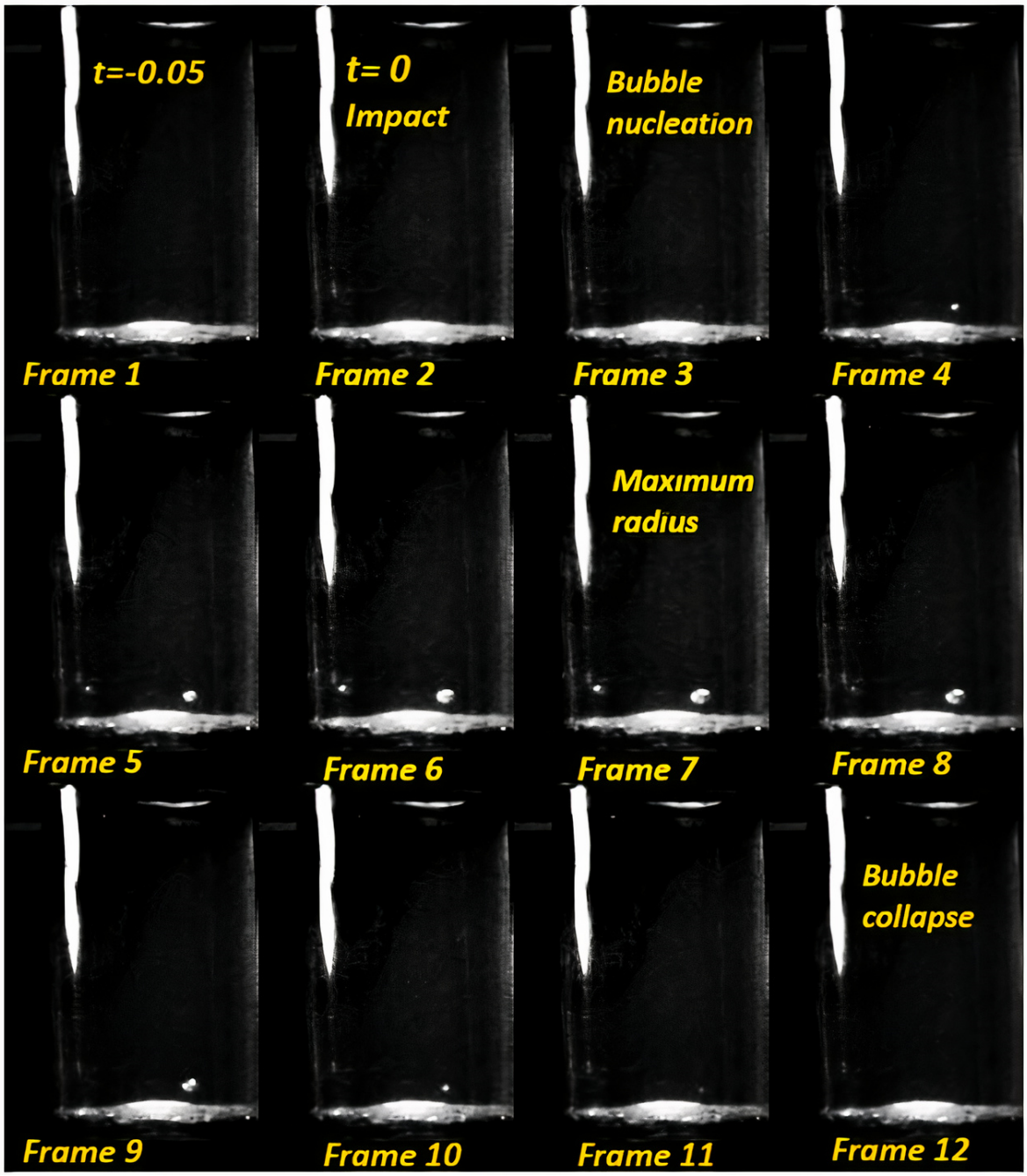

Figure 4.6: Photographs of bubble formation in a 0.3% agarose gel sample recorded with 20 000 fps.

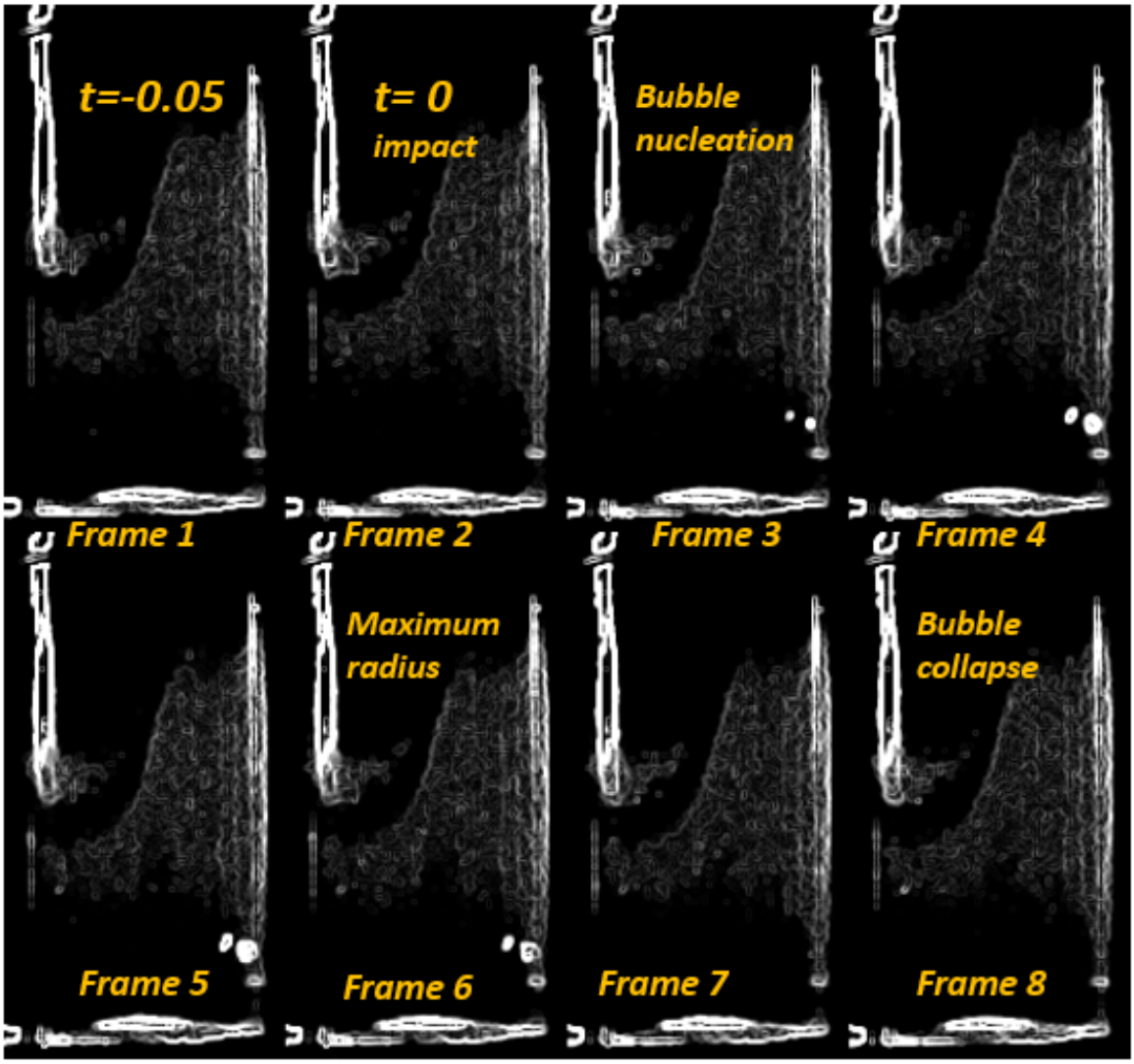

Figure 4.7: Photographs of bubble formation in a 0.7% agarose gel sample recorded with 20 000 fps.

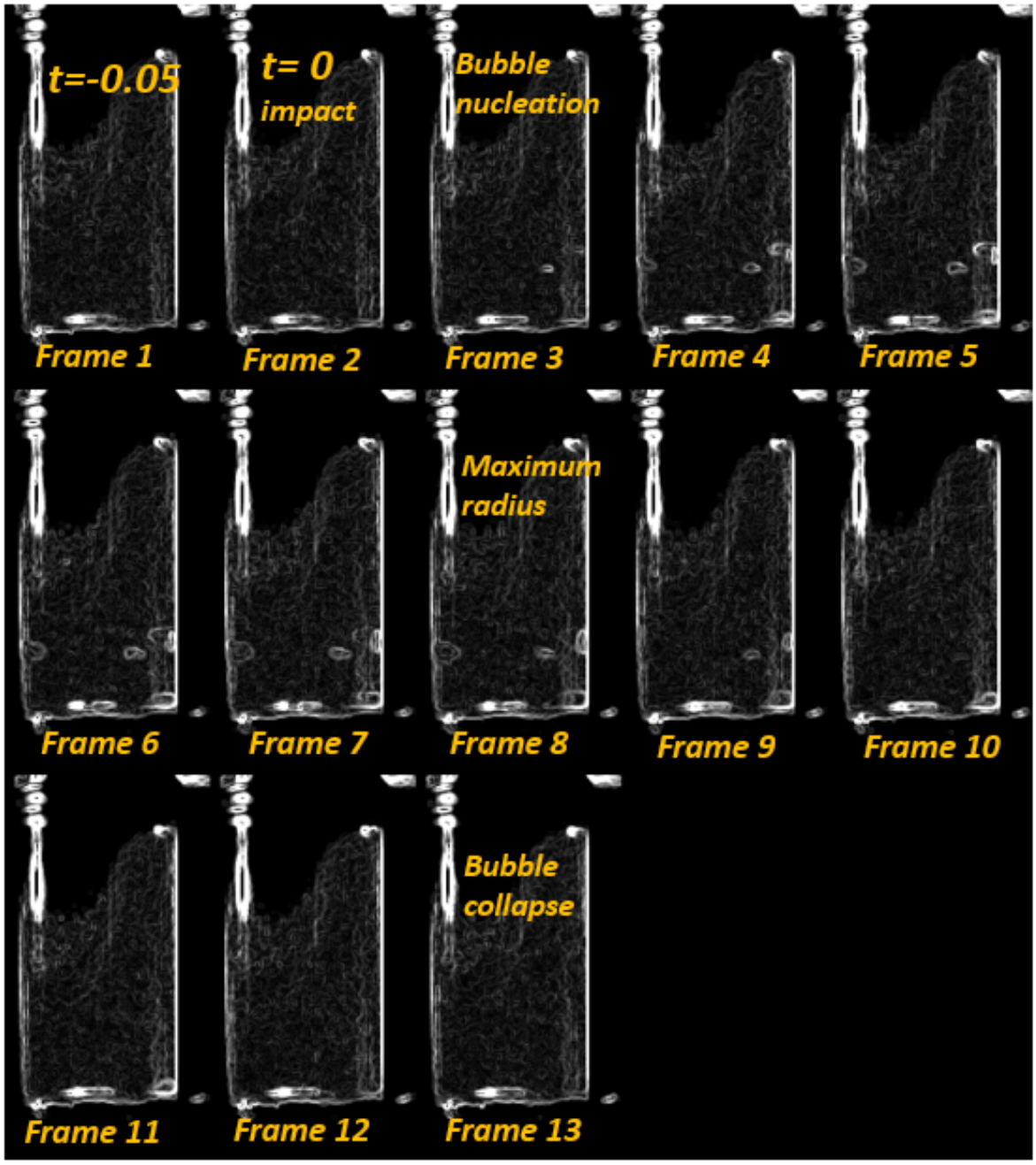

Figure 4.8: Photographs of bubble formation in a 1.5% agarose gel sample recorded with 20 000 fps.

	Attemps	h_d [mm]	$\bar{a}_{\text{amp}}$	$\bar{a}_c$	h_b [mm]
1	1st drop	100-150	741	674	46.5
2	Multiple drops	100-150	1074	988	49.3
3	Multiple drops	100-150	1003	950	48.2
4	1st drop	100-150	910	864	45.6
5	1st drop	100-150	998.5	941	47.5
6	Multiple drops	100-150	1026	971	49.5
7	1st drop	100-150	741	684	48.5

Table 4.2: Total drop tower test results for all 0.3% agarose samples; shown are the drop hight h_d, the mean of the normalized acceleration amplitude $\bar{a}_{amp}$, the normalized critical acceleration $\bar{a}_c$, and the lateral position of bubble cavitation h_b, NC denotes for no cavitation

	Attemps	h_d [mm]	$\bar{a}_{\text{amp}}$	$\bar{a}_c$	h_b [mm]
1	1st drop	150-200	833	797	46.5
2	1st drop	150-200	958	949	45.9
3	Multiple drops	150-200	1263	1198	45.5
4	Multiple drops	150-200	1361	1343	47.3
5	1st drop	150-200	1001.5	953.9	39.4
6	1st drop	150-200	1002	986.2	41.5
7	Multiple drops	NC	NC	NC	NC

Table 4.3: Total drop tower test results for all 0.7% agarose samples; shown are the drop hight h_d, the mean of the normalized acceleration amplitude $\bar{a}_{amp}$, the normalized critical acceleration $\bar{a}_c$, and the lateral position of bubble cavitation h_b, NC denotes for no cavitation

	Attemps	h_d [mm]	$\bar{a}_{\text{amp}}$	$\bar{a}_c$	h_b [mm]
1	1st drop	250-300	1286.5	1221	48.9
2	1st drop	250-300	1259.8	1205	47.1
3	Multiple drops	250-300	1721.8	1684.7	39.6
4	1st drop	250-300	1244	1202.1	43
5	Multiple drops	250-300	1585.1	1448	47.7
6	1st drop	250-300	1453.1	1403	45.1
7	Multiple drops	NC	NC	NC	NC

Table 4.4: Total drop tower test results for all 1.5% agarose samples; shown are the drop hight h_d, the mean of the normalized acceleration amplitude $\bar{a}_{amp}$, the normalized critical acceleration $\bar{a}_c$, and the lateral position of bubble cavitation h_b, NC denotes for no cavitation

	h_d [mm]	$\bar{a}_{\text{amp}}$	$\bar{a}_c$	$R_{\max}$ [mm]	h_b [mm]
0.3% agarose gel	100-150	927.6	867.4	1.15 $\pm$0.18	47.8 $\pm$1.32
0.7% agarose ge	150-200	1069.7	1037.8	1.21 $\pm$0.24	44.3 $\pm$2.87
1.5% agarose ge	250-300	1425	1360.6	2.2 $\pm$0.44	45.20 $\pm$3.15

Table 4.5: Summary of drop tower test results for 3 different groups of agarose samples; shown are the drop hight h_d, the mean of the normalized acceleration amplitude $\bar{a}_{amp}$, the normalized critical acceleration $\bar{a}_c$, the bubble radius $R_{\max}$, and the laterial position of bubble cavitation h_b; $\pm$ denotes the standard deviation

indicated. The acceleration reaches its (negative) maximum value when the impactor hits the cuvette holder, inducing a state of tension in the agarose gel samples. This tensile stress is continued until we observe the maximum radius of the bubble and then the bubble starts shrinking. In the compressive state the bubble collapses. The full drop tower test results for all the concentration groups are indicated in Tables 4.2,4.3 and 4.4. The average acceleration amplitudes and the critical acceleration for the three tested groups of samples are shown in Table 4.5.

For our experiments with the minimum drop height, the region of bubble formation is close to the bottom of the cuvette samples. In most cases, the onset of cavitation starts with a single spherical bubble. When we increased the drop height, we also observed groups of bubbles, see Figure 4.10. However, in this study we focus on the onset of bubble growth to deduce the corresponding critical pressure in the gels. Nevertheless, it is interesting to observe bulk cavitation when the drop height is increased above the

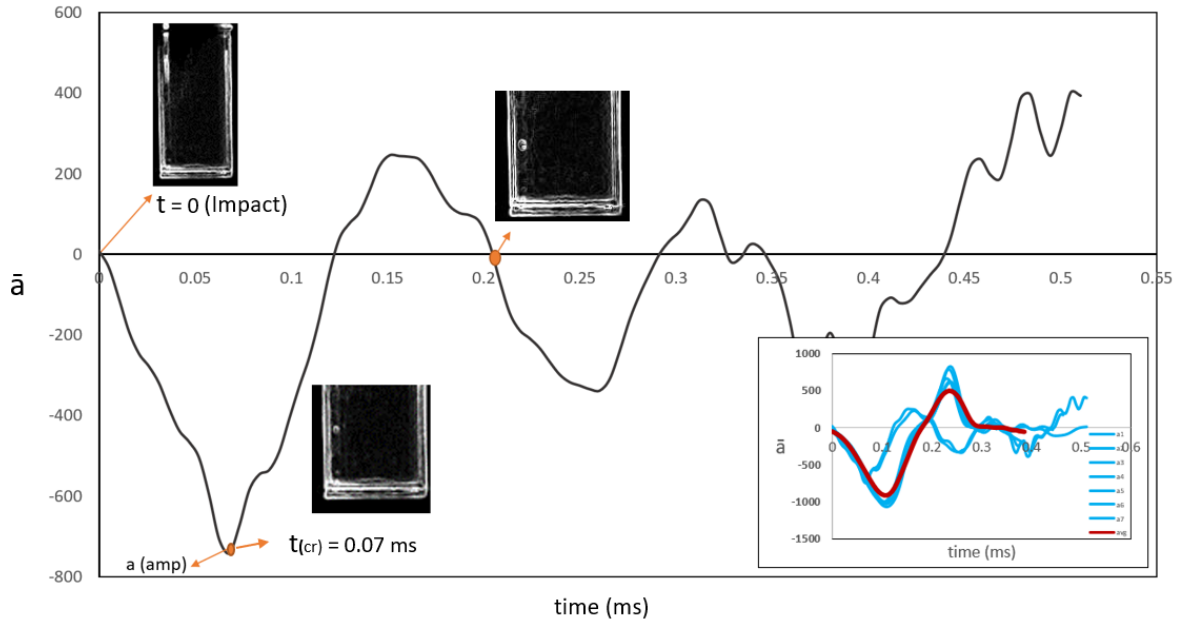

Figure 4.9: Acceleration history and the corresponding bubble formation in a 0.3% agarose gel sample; the inset shows the acceleration profile of all 0.3% samples and in red the average acceleration profile.

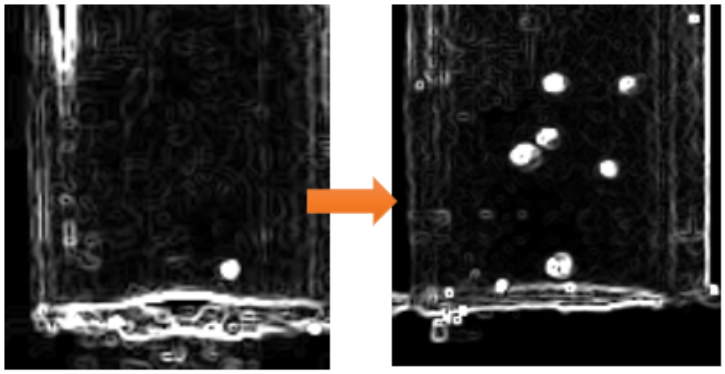

Figure 4.10: 0.3% agarose gel: growth of a single bubble in a sample accelerated with drop height of 150 mm (left) and bulk cavitation in a sample accelerated with a drop height of 200 mm (right)

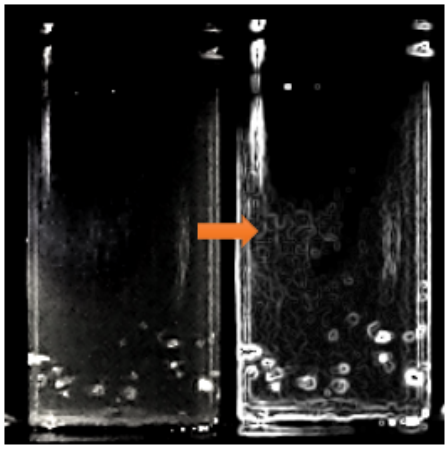

Figure 4.11: Finding edge tool of imageJ for a better bubble edge recognition.

critical h_d, as instead of the formation of a single bubble with a proportionally larger radius, we observe a bulk modulus with not necessarily significantly larger bubbles. By using the imageJ software and in addition to the usage of the threshold tool, the "Finding Edge" tool is also added to precisely recognize the bubble edges for area calculation, see Figure (4.11). Figure (4.12) shows the frame sequence of bulk cavitation in a 0.3% agarose gel. As it can be seen the range of bubble sizes are almost the same and the cavitation time period is somehow shorter with respect to single bubble cavitation.

In Figure 4.13 the evolution of the bubble radius over time is shown for all three types of agarose gels. We observe a wave-like raise and decay of the bubble. In a purely elastic material, the bubble would keep oscillating with that period of tension, cf. [89, 153] but here it is dissipated because of the viscosity of the gels. Depending on the gels stiffness, we see rather different maxima of the bubble size. In the soft 0.3% gel the maximum radius is about 1.15 mm whereas in the stiffer 1.5% gel it is about the double.

We also see from Figure 4.13 that the duration of bubble cavitation correlates with the gel stiffness. The life time of bubbles is almost the same for 0.3% and 0.7% gel but a bit longer for the 1.5% gel samples. This result was expected because from the solution of Eq. 3.34 we know that the period of tension for bubble oscillation depends mainly on the initial bubble radius [153, 140]. This initial radius is in the submicron scale and likely the same for all agarose gel samples investigated here.

From the results of Figure 4.13 we deduce the pressure state at the position of bubble growth. In order to do so, we fitted $R(t)$ by fourth order polynomials. In Figure 4.15 the result for 0.3% agarose is shown; the other samples were fitted accordingly, where the fourth polynomial curve is fitted to the time-dependent radius change of the

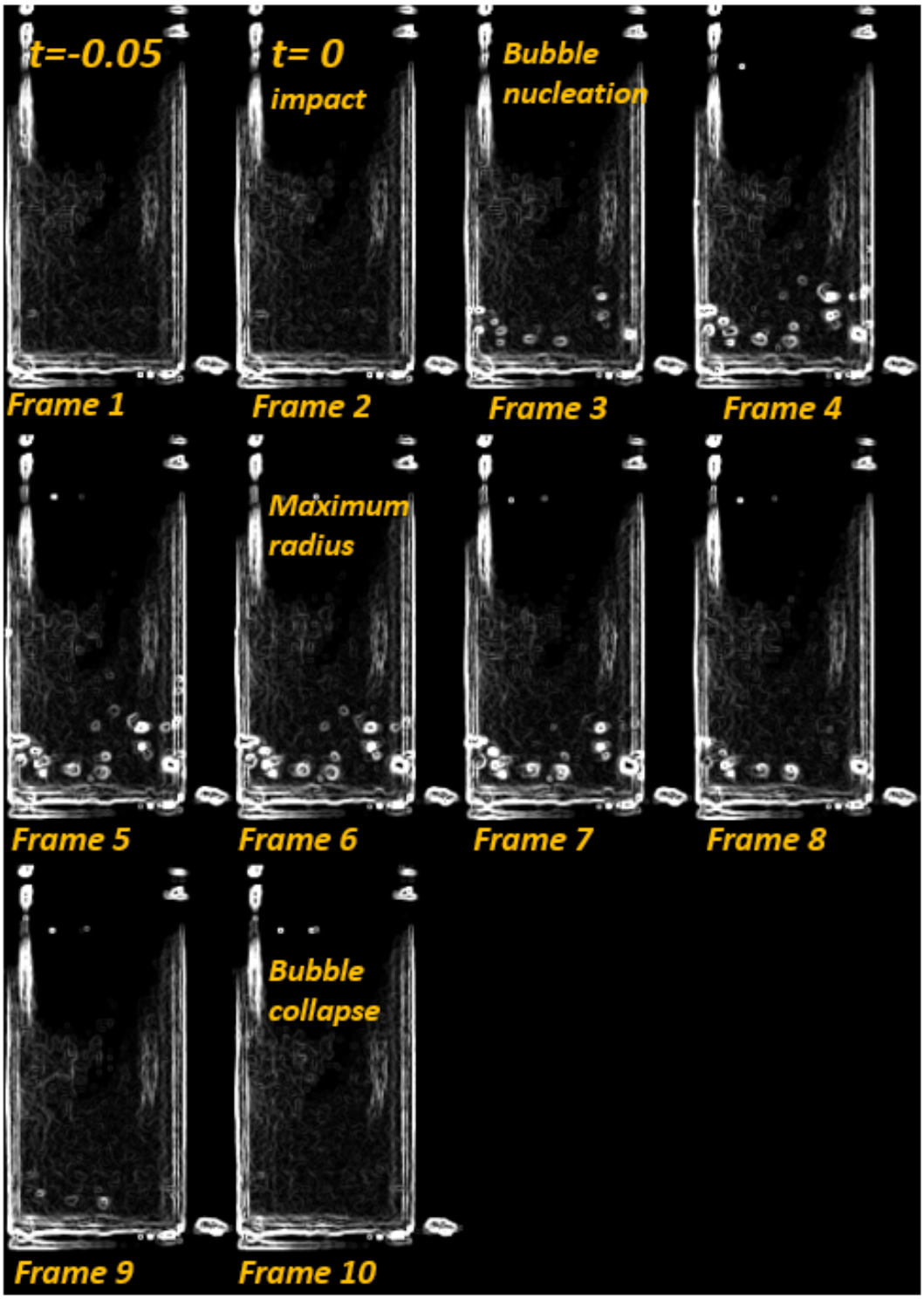

Figure 4.12: Photographs of a bulk cavitation in a 0.3% agarose gel sample recorded with 20 000 fps.

captured cavitation and through the defined model $R(t)$, $\dot{R}(t)$ and $\ddot{R}(t)$ are measured. An evaluation of Eq. 3.34 then gives the pressure state during the bubble's life time. This pressure with amplitude P_{Exp} is later compared to the numerical results and listed in Table 5.1.

Figure (4.14) summarizes the critical acceleration for all measurements of the three types of specimen. We see that the mean critical acceleration causing the onset of cavitation increases with increasing gel stiffness. With a higher stiffness more energy is required to cause a local deformation in gel and, therefore, a higher mechanical energy of the drop is needed to trigger bubble cavitation.

For the evaluation of our experimental results we use the theoretical approach of bubble dynamics, which governs the dynamics of a spherical bubble of radius $R(t)$ in an infinite body, cf. [41]for the basic model and also [136, 137, 89] for the elastic extension.
As mentioned in theoretical model section, for simplicity we assume the bubble to be empty, i.e. the gas pressure P_{G0} is neglected and all local loading is completely attributed to the remote hydrostatic tension $P(t)$, which is induced by the rapid acceleration of the specimen during impact.

Also, we assume no heat transfer between the bubble and the surrounding continuum. Consequently, the mechanisms that contribute to the bubble dynamics are the material's elasticity with shear modulus $\mu_0 = 8\,\mathrm{kPa}$ for 0.3% gel, the surface tension with constant $\gamma_0 = 72\,\mathrm{N/mm}$, the gel's viscosity with kinematic viscosity $\nu_0 = 8.81 \cdot 10^{-7}\,\mathrm{m^2/s}$ and the inertia of the gel with mass density $\varrho_0 = 1000\,\mathrm{g/cm^3}$. The mentioned properties are taken and adapted from [28, 154] for the gels with 0.3%, 0.7% and 1.5% concentrations, since the gel model and concentrations are similar. Agrose gel properties are listed in Table 3.3.

Also, in [28, 155] the existence of small traces of air bubbles, although optically invisible, was seen via a dynamic light scattering in purified water. Because the situation is similar in our study, we assume an initial bubble radius of $R_0 = 100\,\mu\mathrm{m}$ as in [34, 28]. We remark that in [156] much smaller bubbles have been deduced. However, regarding an elastic expansion, an initial bubble size in the submicron range would result in stretches of more than 1000. This seems not realistic and so we assume rather large initial bubbles here, which may be an effect of the fabrication process. We also remark that this initial bubble size only effects the elastic term of Eq. (3.34).

We will evaluate Eq. (3.34) to deduce the magnitude of the acceleration-induced pressure upon impact from the measured bubble size. Because we consider in our experiments the minimum drop hight, this value corresponds to the minimum cavitation pressure for the different concentrations of agarose.

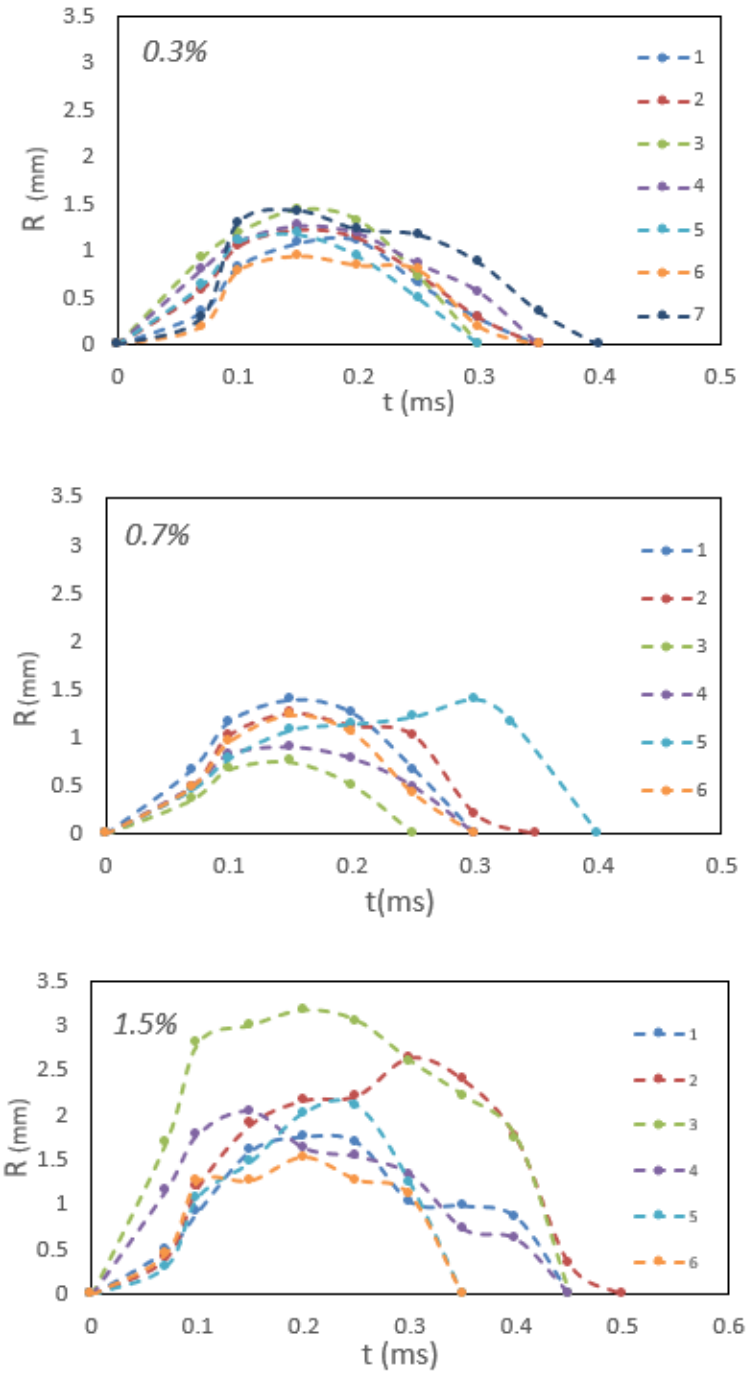

Figure 4.13: Bubble radius change over time for 0.3% agarose (top), 0.7% agarose (middle) and 1.5% (bottom) agarose gel samples.

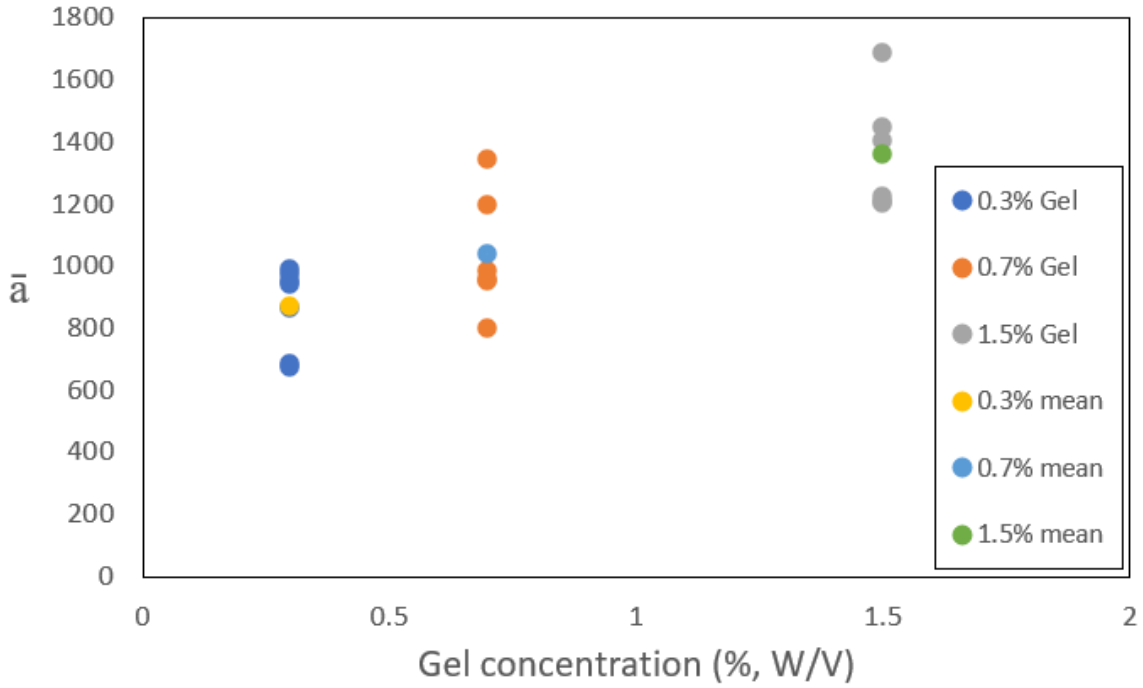

Figure 4.14: Measured values of the critical acceleration for cavitation over the concentration of the agarose gels; the inset shows the corresponding elastic modulus.

Regarding the fact that we investigate the situation of minimum pressure for bubble cavitation, we can conclude that a stiffer material is more affected by bubble growth. On one side, it can sustain a higher pressure (or, to be precise here: a higher hydrostatic tension) but, on the other side, once the threshold of cavitation pressure is reached, the cavitating bubbles are larger. With respect to the actual purpose of the agarose gel, namely to mimic brain tissue, this means that in a stiffer (maybe older) brain tissue the potential damage of bubble cavitation is larger. However, we remind that we consider the minimum cavitation pressure here and cannot conclude on groups of bubbles from this analysis.

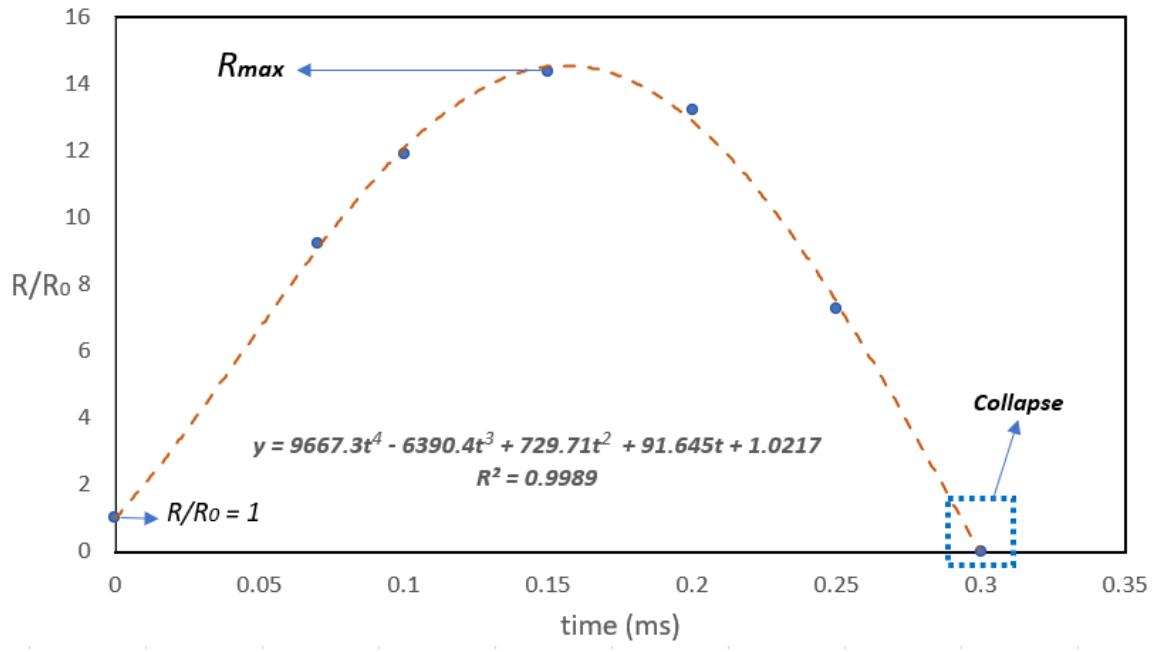

Figure 4.15: Measured relative bubble radius over time for the 0.3% agarose gel sample and a 4th order polynomial fit of the data

5 Numerical investigation of cavitation test and pressure gradient of bubble

In this chapter, we focuse on the numerical investigation on the validation of the test results, bubble dynamics and the related pressure-volume changes. Important parts of this chapter are submitted for publication by us, in [141, 142].

5.1 Finite element modeling of drop tower test

In parallel to the experiments, we performed numerical analyses using the finite element method (FEM). The commercial FEM program Abaqus was used; all dynamic processes were computed with an implicit time-discretization.

5.1.1 Drop tower model

In a first step the whole cuvette holder, the attached cuvette sample, and the rubber foam sheet at the bottom of the cuvette holder were designed and meshed with their exact dimensions, see Figure 5.1. A standard linear tetrahedra mesh (C3D4 elements) was used for the cuvette holder and the sheet; for the cuvette sample, the corresponding hybrid option was used. All parts of the model including the gel sample, the cuvette holder and the rubber sheet, were meshed as one single part to avoid inaccurate contact conditions.

For the rubber sheet, a viscoelastic model was used with the material properties of Table 4.1 and a relaxation time of $\tau = 0.15\,\mathrm{s}$ with the corresponding relative modulus of $\gamma = 0.25$; we refer to Eq. (5.2).

The rubber sheet is completely fixed at the bottom.The boundary of the cuvette holder is fixed in a way that only movement in the y-axis direction (upward and downward) are allowed. A radial constrain of the cylindrical gel sample is implemented to model the cuvette, where x and z directions are fixed. At the top, the impact of the steel bar is modeled with a rigid analytical body impacting with a velocity of $V = \sqrt{2gh}$. A surface-to-surface contact between the analytical rigid body and the upper surface of the cuvette holder was defined, which then causes the acceleration of the setup and its downward movement.

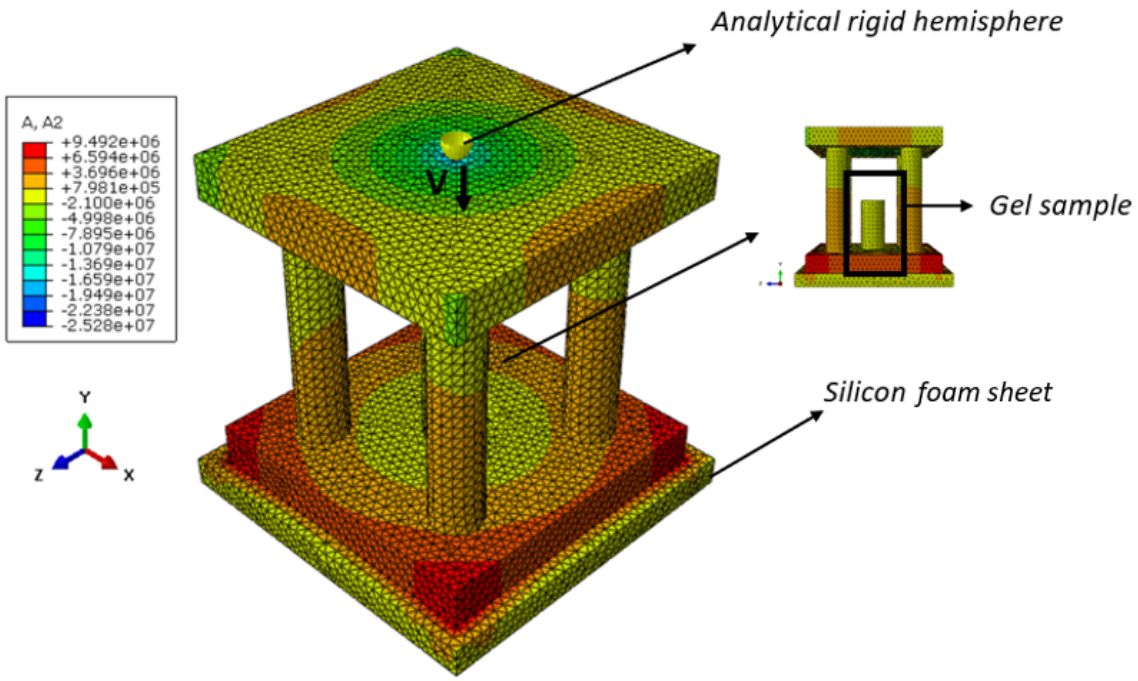

Figure 5.1: 3D FEM model of cuvette holder; the color indicates the acceleration (in Y direction) computed for a 100 mm drop height

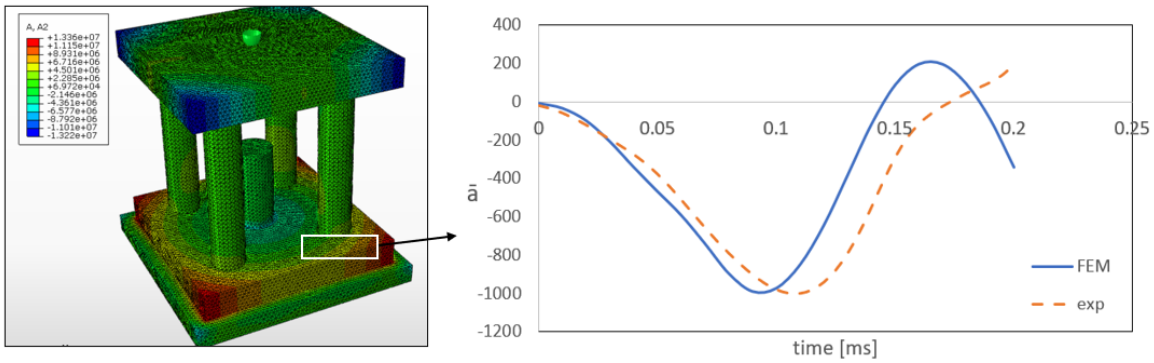

Figure 5.2: Area of the computed acceleraion from FEM (left), Mean normalized acceleration $\bar{a} = a/g$ over time from experiment and computed acceleration $\bar{a}$ from FEM (right)

The agarose sample is modeled with a hyperelastic Neo-Hookean material model with energy density

$$W = c_1 \left(\operatorname{tr} C - 3\right) + \frac{1}{D_1} \left(\det C^{1/2} - 1\right)^2 \tag{5.1}$$

where C is the right Cauchy-Green tensor and $\operatorname{tr} C$ its first invariant (trace). The material constants are the shear modulus $\mu_0 = 2c_1$ with $c_1 = 4 \cdot 10^{-3}\,\mathrm{MPa}$ and the inverse of the bulk modulus $K/2$ with a value of $D_1 = 0.009\,\mathrm{MPa}^{-1}$ for an agarose gel of 0.3% concentration. For the 0.7% gel and the 1.5% gel these values were linearly extrapolated to give $c_1 = 9 \cdot 10^{-3}\,\mathrm{MPa}$, $D_1 = 0.0021\,\mathrm{MPa}^{-1}$ and $c_1 = 2 \cdot 10^{-2}\,\mathrm{MPa}$, $D_1 = 0.0045\,\mathrm{MPa}^{-1}$, respectively. For the viscosity of the material a Maxwell model is used,

$$\mu(t) = \mu_0 \left(1 + \gamma \exp\left(t/\tau_0\right)\right) \tag{5.2}$$

with a relative shear modulus of $\gamma = 0.6$ and a relaxation time of $\tau_0 = 80\mu\mathrm{s}$. The volumetric viscosity is modeled analogously, now with a relative bulk modulus of 0.2 and the same relaxation time.

We started our numerical investigations with a convergence study, i.e. the setup was computed with three different finite element meshes with a total number of 80424, 148521 and 317222 elements. The results showed that the model of Figure 5.1 with 80424 elements is sufficiently accurate. In addition to the mesh density studies, it was proven that the use of linear tetrahedral elements leads us the same results as quadratic elements, see Figure 5.15. Hence we chose the linear elements as stated earlier, due to a more efficient computation.

For different drop heights, the impact boundary conditions were applied and the (normalized) acceleration at place of accelerometer on the cuvette holder is computed. The

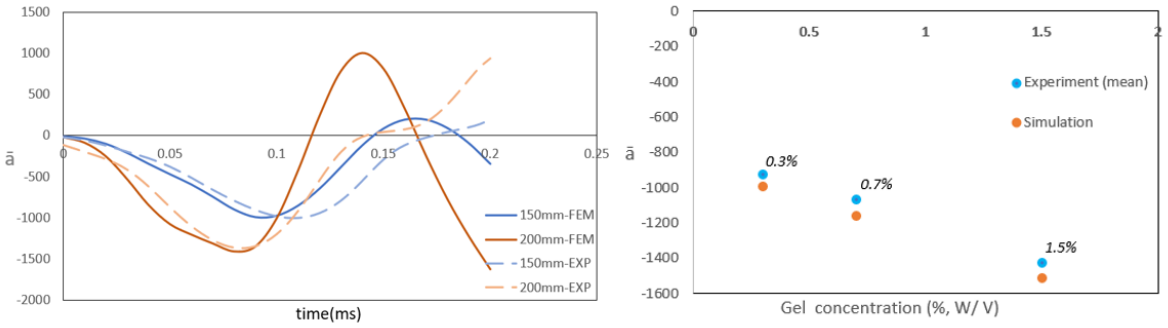

Figure 5.3: Normalized acceleration $\bar{a} = a/g$ over time at the bottom of the specimen for the different drop heights (left) and computed acceleration $\bar{a}$ compared to the mean of the acceleration values measured experimentally for the different gels (right)

resulting acceleration over time is displayed in Figure 5.2, based on the experimental cavitation drop height $h_d = 100 - 150\ mm$. The comparison with the experimental results shows a very good agreement, therefore we continue to use these values as input for a more detailed analysis.

The aim of this full-setup computation was to recover and validate the measured acceleration of the specimen. Therefore, for the different drop heights, the impact boundary conditions were applied and the (normalized) acceleration is computed. The resulting acceleration over time is displayed in Figure 5.3. The comparison with the experimental results shows a very good agreement and so we continue to use these values as input for a more detailed analysis.

5.1.2 Pressure history in the gel samples

We continue studying the pressure distribution in the agarose samples. The corresponding numerical simulation approach is the same as in the previous section but now, in order to reduce the computational costs, only the gel sample attached to the steel surface is extracted from the whole simulated setup. The model is shown in Figure 5.4. The acceleration profile measured in the experiment and validated with the computation above is now applied as the input boundary condition on the bottom surface. Because our test results indicate that the onset of cavitation occurs in the first trough, the process is simulated for about 0.30 ms. The corresponding time period is indicated by the red dashed lines in Figure 5.4. Additionally, Figure 5.5 shows the position where the pressure is evaluated later.

To analyze the pressure in the FEM model, we refer to Section 4.3 where we used our experimental data to determine the bubble radius $R(t)$. These data then serve as input to compute the pressure $P_{Exp}(t)$ using Eq. 3.34, whereby the first and second derivatives were gained from the fitted curves.

In Figure 5.6 the time-dependent pressure $P(t)$ at the bottom of the specimen is

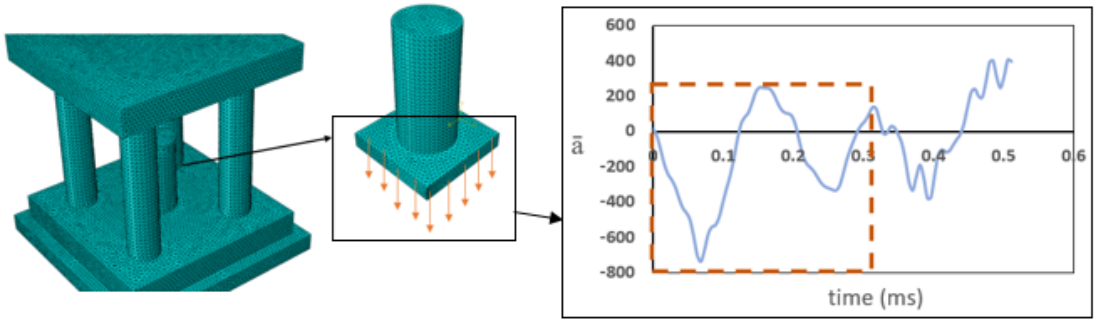

Figure 5.4: FEM model of the agarose gel samples extracted from the total model of Fig. 5.1 and typical input acceleration profile

shown. Depending on the gel concentration, we see the tension starting at about $t = 0.05\,\text{ms}$, then raising to a maximum value at $t = 0.15 \ldots 0.2\,\text{ms}$, and then decaying. The full pressure-time history is computed with the FEM model whereas the dots indicate the maximum tensile pressure obtained from the solution of Eq. 3.34. These tension values are 450 kPa, 550 kPa and 1 MPa for the 0.3%, 0.7% and 1.5% agarose samples, respectively.

The good agreement between the amplitude pressures gained from the FEM and experimental-theoretical data is encouraging and shows that the bubble cavitation in hydrogel and/or soft biological tissue can really be captured with FEM analyses and the corresponding material model of agarose gel. There is also a good agreement for the duration of the tensile stress up to the maximum growth of the bubble $t_{\text{r-max}}$, which was between 0.16 ms to 0.20 ms for the tested samples, see Table 5.1.

In addition, the pressure in the specimen is determined along a path in the centerline of the gel sample, see Figure 5.5. The three plots of Figure 5.7 show the pressure in the initial stage at $t = 0.05\,\text{ms}$, at the time of the maximum bubble size, and at the final state $t = 0.29\,\text{ms}$ for the different agarose samples. Here we observe that at all times the pressure has its maximum value at the bottom of the specimen. This makes clear why after impact from the minimal drop height single bubbles are observed in this area. After about 0.3 ms the pressure has turned into a compressive state in the full specimen.

5.2 Pressure-volume gradient validation in FEM

Here we also present the cavitation pressure and the correlated volume change of the bubble through a specific method in FEM. As explained previously, after the validation of the experimental acceleration, the local pressure in the area of bubble nucleation was derived by using the extracted FEM model shown in Figure 5.4. We first applied the validated acceleration as input (applied on the bottom surface), to derive the pressure

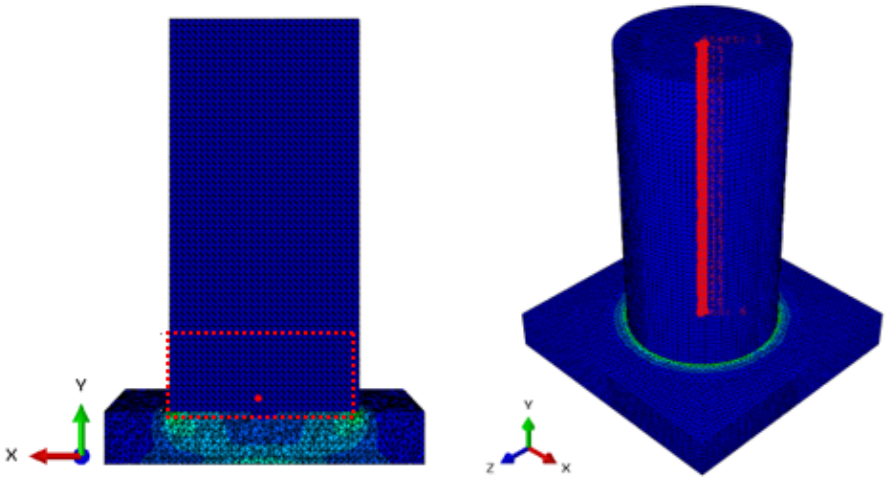

Figure 5.5: FEM model of the sample with the positions where the pressure history is evaluated (left) and with the centerline path (right)

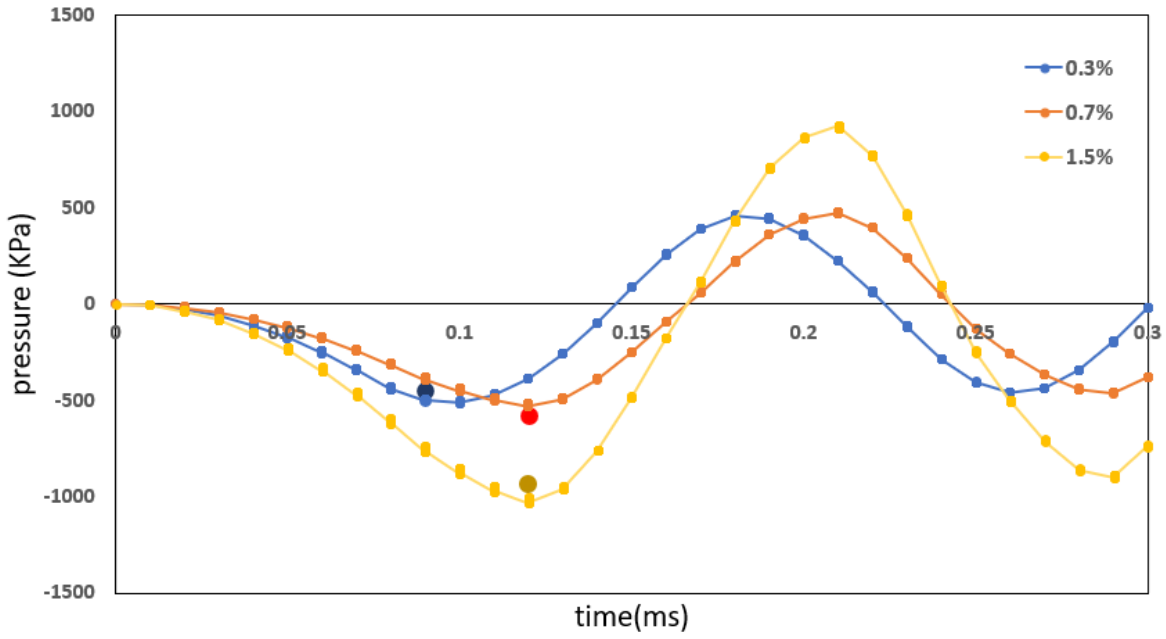

Figure 5.6: Pressure history at the position of bubble cavitation for the samples of 0.3%, 0.7% and 1.5% agarose, the amplitude pressure from Eq. 3.34 is indicated as a big dot for each concentration group

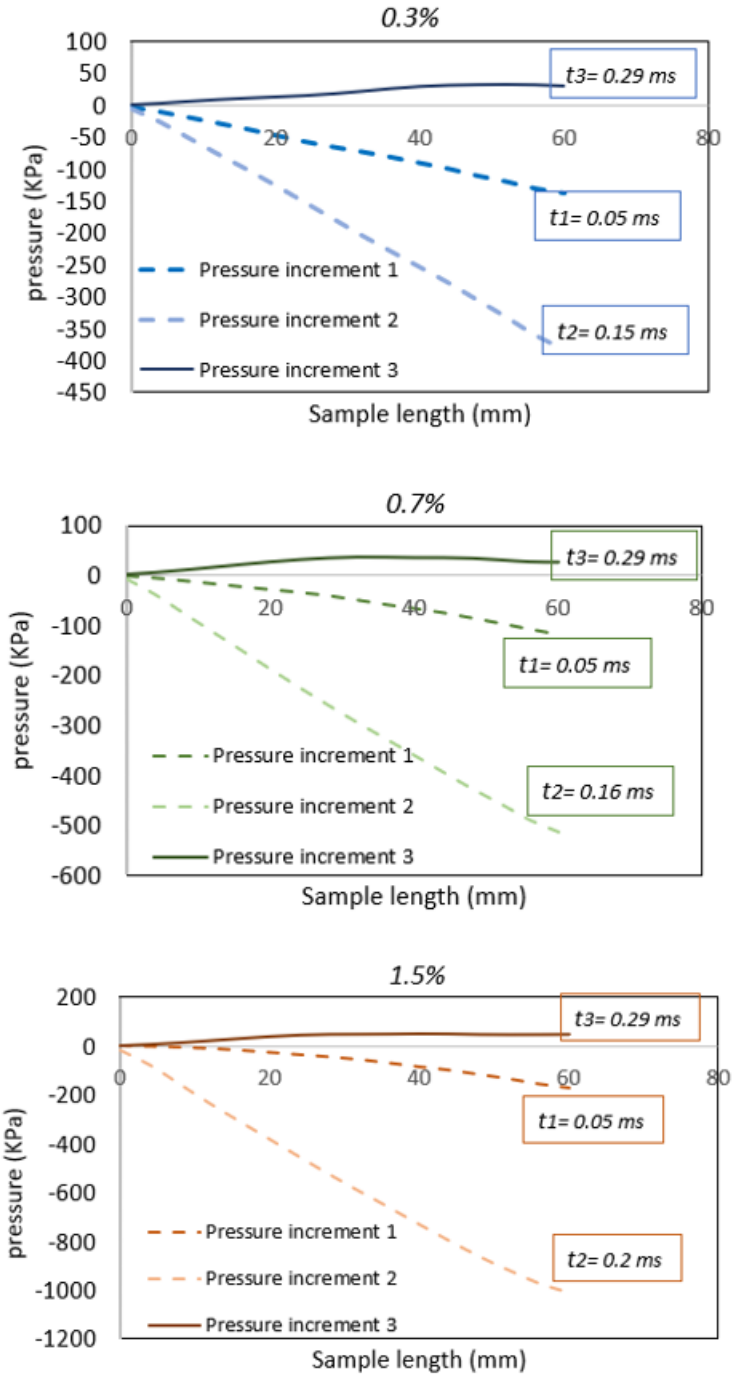

Figure 5.7: Pressure distribution along the centerline of the samples from the top at 0 to the bottom at 60 mm

	P_{FEM}[kPa]	P_{Exp}[kPa]	$t_{\text{r-max}}$ [ms]	T_c [ms]
0.3% agarose gel	-388	-447 ±92.2	0.15 ±0.02	0.34 ±0.03
0.7% agarose gel	-530	-552 ±227.6	0.17 ±0.05	0.31 ±0.04
1.5% agarose gel	-1006	-936 ±340	0.21 ±0.04	0.42 ±0.05

Table 5.1: Summary of numerical and experimental-theoretical data for the maximum pressure P, the time till maximum bubble radius $t_{\text{r-max}}$ and the period of tension T_c for cavitation.

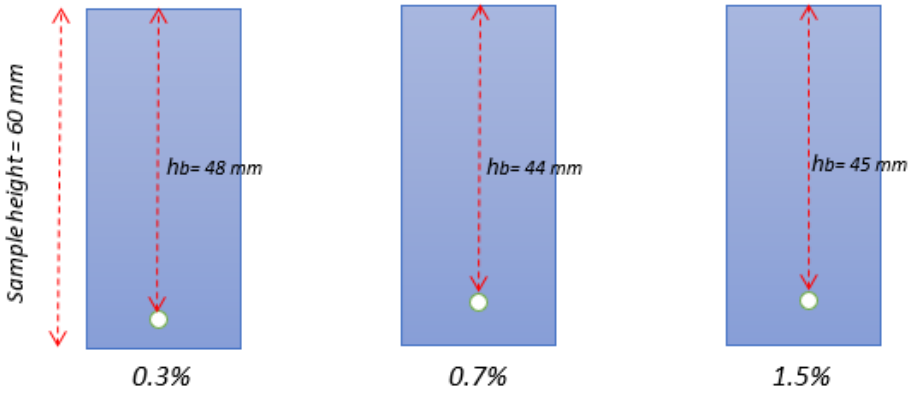

Figure 5.8: Bubble location (h_b) in different concentration groups based on the experimental results

in the cavitation region.

In order to precisely address the correlated volume change and pressure of the cavitation bubble, the "fluid-filled cavity modeling" method in Abaqus is used. The pressure drop in the region of the microbubble during high impact loading results in local vaporization of a gel material and the creation of gas pressure inside the microbubble followed by bubble expansion. Accordingly, the expansion of the microbubble could be simulated using "fluid-filled cavity modeling" tool in Abaqus explicit [26]. In this modelling tool, hydrostatic fluid elements, as surface elements, cover the entire internal boundary of the closed fluid cavity and provide a coupling between the volume change of the cavity and the pressure exerted by the contained fluid (e.g. gas). Formed cavity by hydrostatic surface elements associated with a common node with a single degree of freedom called reference node. The reference node is used to apply the pressure profile and, to obtain the volume change as a history output.

The relationship between the gas pressure P_g and the volume V_c of the cavity is given by:

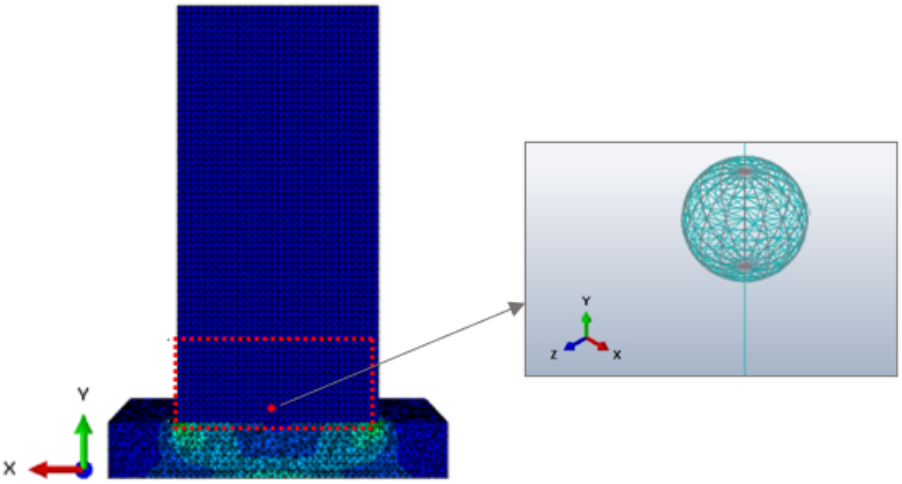

Figure 5.9: 3D model of the located bubble in the sample in FEM

$$P = \frac{R_g m_c T}{M_a} V_c \tag{5.3}$$

where T is the absolute temperature (= 299K assuming that compression is isothermal), R_g the universal gas contact (8.314 J/K mol), M_a the average molecular weight of the air within (0.0289 Kg/mol) [157] and m_c the mass of gas in the bubble that it is determined from the initial volume of the cavity with the initial pressure of $P_0 = 1$ atmosphere.

Based on the experimental results, specifically related to bubble location h_b, a spherical cavity with an initial radius of 100 μm, the volume of 0.0041 mm^3, was created and located on observed locations in 3 different concentration sample groups, respectively, as shown in Figure 5.8. In addition, the 3D model of the located bubble in the sample in FEM is illustrated in Figure 5.9. In order to optimize the computational cost, we used the 2D-axisymmetric model with the same specifications used in the previous step.

After creating the micro size bubble in the sample, the local pressure which was validated in the previous step is used as bubble inner pressure to be prescribed and derive the resulted volume growth of the bubble. Figure 5.10 shows the results for a 0.3% simulated agarose sample, in which the increased size of the axisymmetric model is shown with the displacement contour.

The time-dependant variations of the bubble volume and pressure inside the bubble for three different agarose gel concentration samples are shown in Figure 5.11. As it

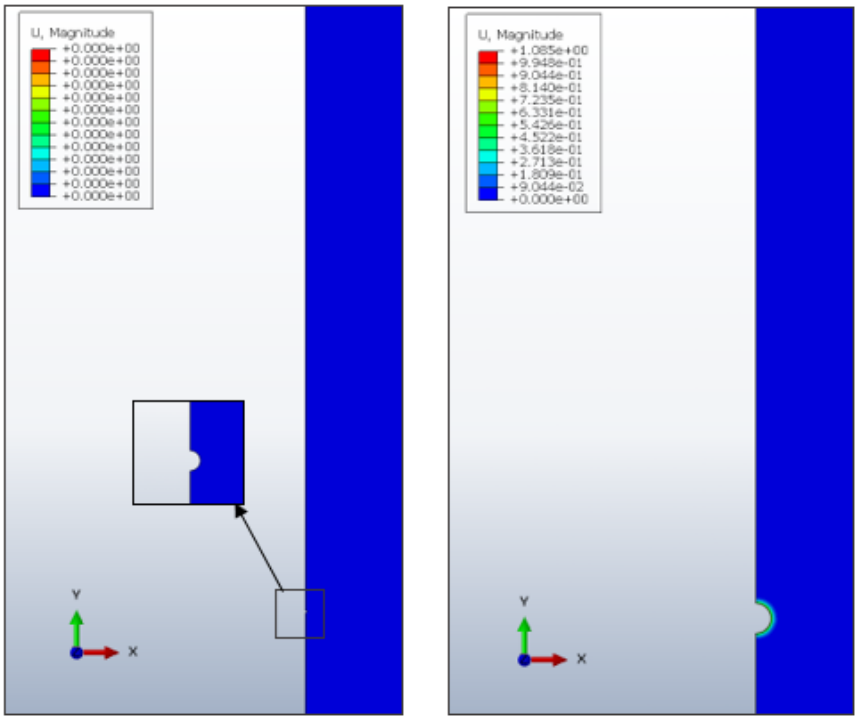

Figure 5.10: 2D axisymmetric model of the bubble growth in simulated 0.3% sample in FEM, before applying the pressure (left), and after (right) with displacement contour.

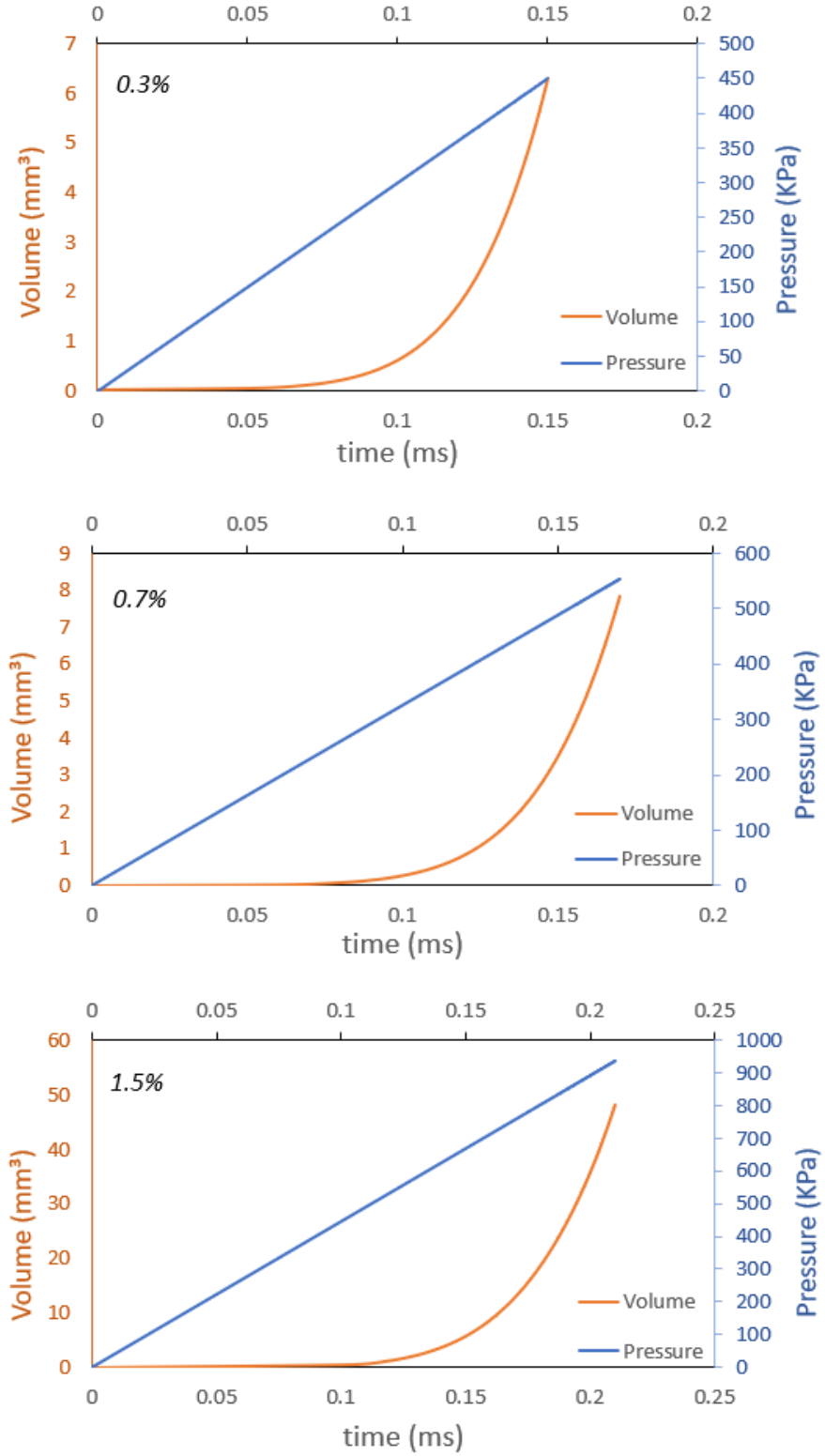

Figure 5.11: Pressure-volume behaviour of 0.3% (top), 0.7% (middle) and 1.5% (bottom) agarose gels in FEM

	$Pressure$[kPa]	Volume (Max) $[mm^3]$	T [ms]	$\bar{a}_{\text{amp}}$[FEM]
0.3% agarose gel	450	5.91	0.15	902
0.7% agarose gel	550	7.78	0.17	1050
1.5% agarose gel	940	47.24	0.21	1520

Table 5.2: Summary of numerical results from FEM

can be seen, the validated pressures are prescribed up to nearly 450, 550 and 1000 KPa, for 0.3%, 0.7%, 1.5% samples, respectively. The duration of the prescribed pressure is related to experimental data of each concentration group indicated as t_{r-max} in Table 5.1. The derived maximum volumes are 5.91, 7.78 and 47.24 mm^3. The resulted volume change derived from FEM, using fluid-filled cavity method, shows good agreement with the experimentally measured values. The nonlinear behavior of the volume curves could be related to the inertia of the agarose matter since this cavity does not act as a free balloon becoming larger but also resisting and growing in the vicinity of the matter in the defined medium. The bubble growth difference, in terms of volume, in 0.3% and 0.7% is fairly little, while when it comes to 1.5% sample in both experiment and FEM the bubble growth shows a significant difference, with respect to the applied bubble pressures.

In addition to the pressure-volume behavior, the amplitude acceleration resulting from the inserted pressure is incorporated, 902, 1050 and 1520 g, for 0.3%, 0.7% and 1.5% samples, respectively, which shows also a good agreement with the validated values of the experimental amplitude acceleration. The acceleration values are taken from the node nearby the bubble, where the pressure is applied, and not necessarily from the bottom plate, due to the dissipation that occurs the acceleration values might be less on the plate because of the nature of the simulated model, that the pressure is inserted in the bubble and not on the bottom plate. Table 5.2 shows the summary of the pressure-volume results in FEM.

5.3 Discussion and conclusion

Soft gels that mimic the biological tissue properties are used as tissue simulants in order to assess for damage-related rapid mechanical inputs. In this regard, we performed the drop tower test on the bio-agarose samples of different stiffnesses to investigate the cavitation behavior and specifically pressure gradient in the agarose samples. In parallel to the experiment, FEA was applied and the test results were validated through numerical simulation.

Our study claims that maximum bubble radius increases linearly by increasing the amplitude of input acceleration (a_{in}). During our tests, the critical acceleration were detected as the onset of cavitation were captured. This critical acceleration increases by increasing the agarose gel stiffness as well. The majority of bubbles were formed on the bottom third of the cuvettes.

The tensile stress at the bottom of the samples initiated the bubble formation and growth, while the accompanying compression stress causes the bubble to sharply shrink and eventually collapse. In the majority of the attempts, the pace of the cavitation onset to maximum bubble size ($t_0 - t_{\text{r-max}}$) is slower than the collapse stage ($t_{\text{r-max}} - t_{collapse}$). The experimental results confirm that the total time from initial bubble formation, based on the captured frames by high-speed camera (20k fps), to complete collapse of the bubble is mostly about 0.3 ms. Furthermore, the shape of the bubbles was mostly spherical, which made the area calculation convenient for final radius determination and theoretical model usage.

During this study, we investigated the cavitation behavior in agarose gel up to collapse, but not the collapse itself, since at this moment it is not yet possible to capture frames precisely enough to address the characteristics of the collapse part. It should be noted that the collapse, by itself, could be another source of damage to brain tissue. When the impact happens, the bubble start growing and great amount of energy is stored in the gelatin medium. Before the complete process of impact the applied acceleration sharply decreases and therefore, the elastic energy would lead to bubble collapse, as well as the compression stress.

In parallel to the experiment, finite element simulations were used to model the test setup and to validate the results related to acceleration and more importantly the pressure. The P_{amp} gained from FEA was in good agreement with the theoretical-experimental data. The source of slight differences could be related to the fixation of the experimental setup with respect to perfect contact in FEA. Moreover, the surface tension defined in the theoretical model, although moderate value, could also marginally makes small difference, since in the FEA surface tension is neglected.

Our study on the cavitation behavior and pressure gradient in agarose gel as a soft tissue simulant is an important step toward a better understanding of the dynamic behavior of such soft tissue simulants, which can be used in studying the injury process of human tissue in moderate to severe brain injuries. Typically soft biological tissues has the strength of about 1-10 kPa. Among the three tested groups of agarose gels with different concentrations, the 0.3% agarose gels has the most relevant properties for soft tissue of brain, although still slightly stronger. By considering the critical acceleration causing the onset of cavitation in 0.3% gels (867 g), and the consequent local pressure of the bubble, which is about 380-450 kPa based on the experiment and FEA results, we can predict that such acceleration-induced pressure would cause a temporary and permanently injury to the brain tissue, including shear damages and more significantly volumetric including cavitation.

In addition, by using the fluid-filled cavity method we recovered the volume growth of the located bubbles in the samples, based on experimental data and the correlated pressure-volume behavior indicates good agreement with the test results, reaching to the maximum volume of 5.91, 7.78 and 47.24 mm^3 for 0.3%, 0.7% and 1.5% samples, respectively.

The quantitative measurements of our study regarding the acceleration induced pressure changes in agarose gel can be utilized for further development of brain injury investigations and would be useful to study the soft biometarials such as agarose gel, which have vast applications in biomechanics for impact-injury simulations and related dynamic bubble behavior.

Appendix

Abbreviations and symbols

SHPB	Split Hopkinson Pressure Bar
SR	Standard resin
TR	Tough resin
c	Wave speed
z	Acoustic impedances
$\epsilon_I(t)$	Incident strain wave
$\epsilon_T(t)$	Transmitted strain wave
$\epsilon_R(t)$	Reflected strain wave
ϵ_s	Specimen strain
$\dot{\epsilon}$	Strain rate
σ_s	Specimen stress
E_{dyn}	Dynamic Young modulus
GM	Gray matter
WM	White matter
BSCC	Brain stem and corpus callosum
CSF	Cerebrospinal fluid
P_v	Vapor pressure
P_a	Ambient pressure
P_b	Bubble pressure
P_G	Gas pressure
P_∞	Remote pressure
k	Polytropic exponent
λ	Stretch (bubble)
Ψ	Strain energy density
$\mathcal{F}$	Deformation gradient
$\mathcal{F}^T\mathcal{F}$	Deformation tensor
K	Kinetic energy

Π	Potential energy
$-\Phi$	Rayleigh dissipation potential
γ	Surface tension
ν	Viscosity
ρ	Mass density
μ	Shear modulus
h_d	Drop height
h_b	Bubble location (height)
$\bar{a}_{\text{amp}}$	Amlpitude acceleration
$\bar{a}_c$	Critical acceleration
NC	No caviation
C	Cauchy-Green tensor
τ_0	Relaxation time
V_c	Cavity volume

Mesh convergance

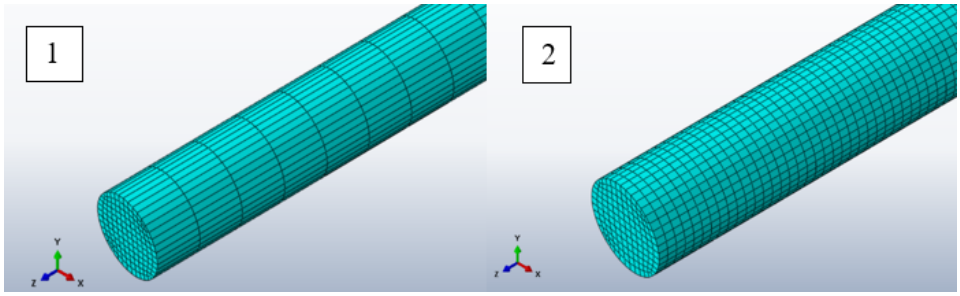

Figure 5.12: Mesh convergance: Mesh density1 (left), and mesh density2 (right) of SHPB model

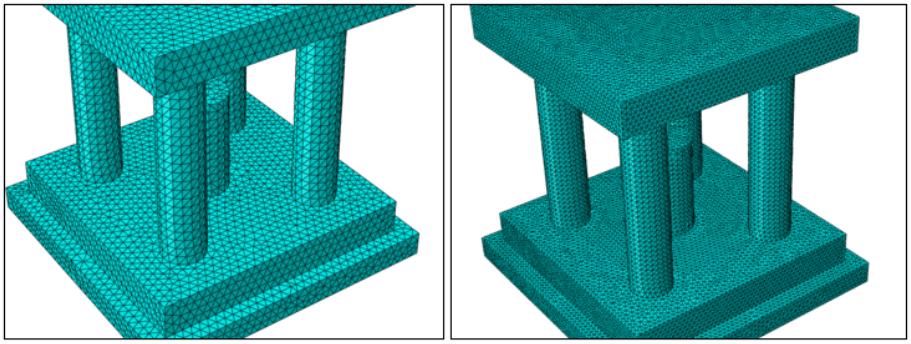

Figure 5.13: Mesh convergance: whole model in FEM using low mesh denisity (left), high mesh density (right)

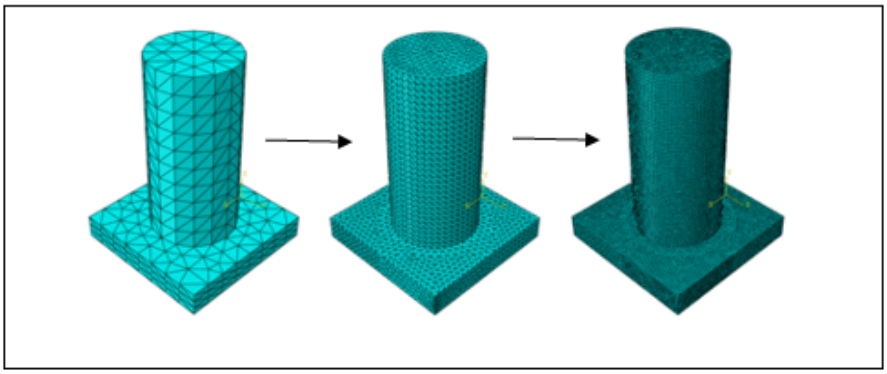

Figure 5.14: Mesh convergance: just sample model in FEM using low mesh density and high mesh density (from left to right)

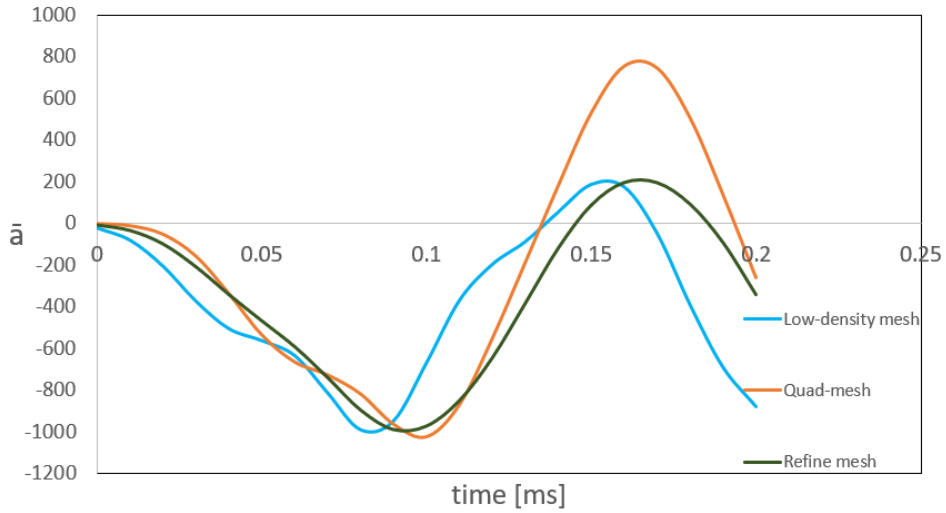

Figure 5.15: Mesh convergance studies of two different mesh densites and quadratic element related to accelaration $\bar{a}$

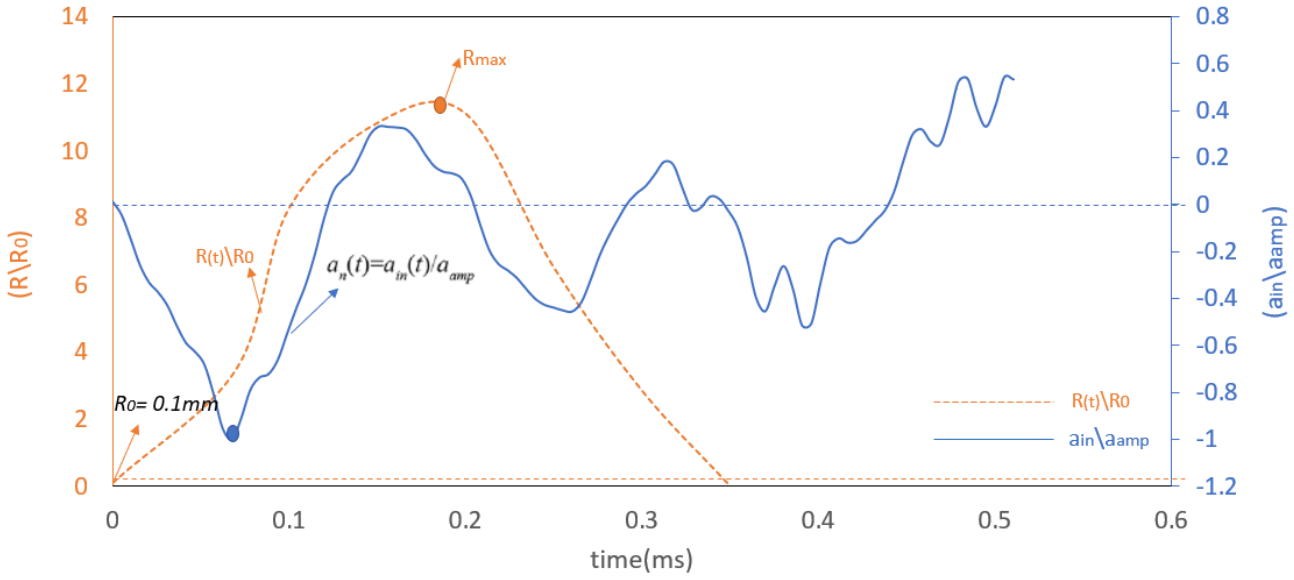

Figure 5.16: The relation between R/R_0 to normalized $\bar{a}$ for a 0.3% agarose sample

Cuvette holder drawing

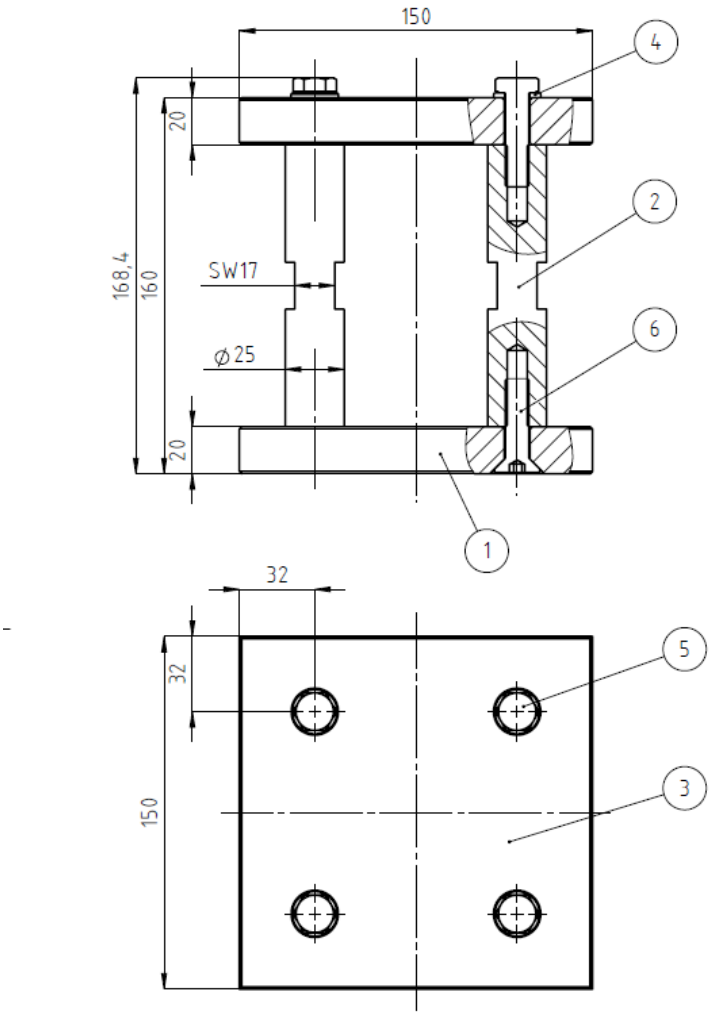

Figure 5.17: Assembly of the whole cuvette holder

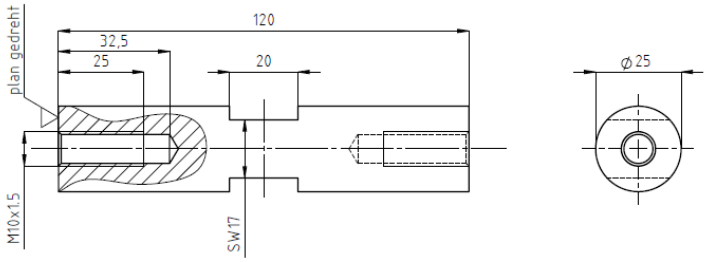

Figure 5.18: Technical drawing of the vertical cylindres

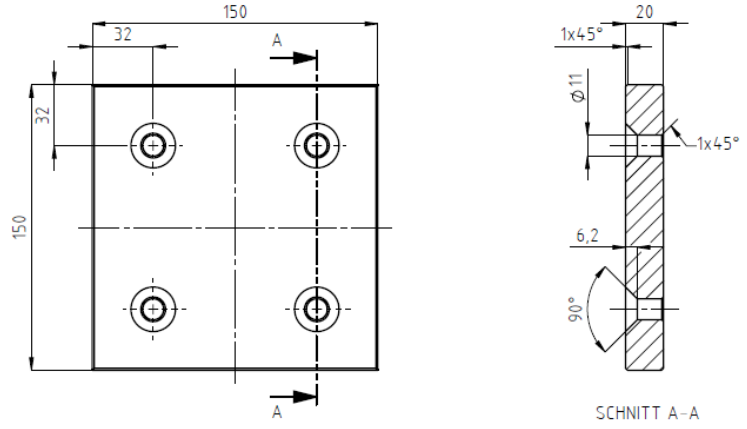

Figure 5.19: Technical drawing of the plate

Bibliography

[1] Hugo, K., Lam, L.: The impact of 3D printing implementation on stock returns: A contingent dynamic capabilities perspective, International Journal of Operations & Production Management (2019).

[2] Wang, X., Jiang, M.: 3D printing of polymer matrix composites: A review and prospective. Composites Part B: Engineering J (2017).

[3] Crivello, J., James V.: Photopolymer Materials and Processes for Advanced Technologies. Chemistry of Materials Chem. Mater. 26.1 (2014).

[4] Fromlabs: The Ultimate Guide to Stereolithography (SLA) 3D Printing (Updated for 2020). Retrieved (2020).

[5] Formlabs. Url: https://formlabs.com/de. Accessed 22.02.2020

[6] Jandt, K., Sigusch, W.: Future perspectives of resin-based dental materials. Dental materials journal, Volume 25, Issue 8, 1001-1006, (2009).

[7] Bonyar, A., Santha, H.: 3D Rapid prototyping Technology (RPT) as a powerful tool in microluidic development. Procedia Engineering 5, 291-294, (2010).

[8] Ruamario, J., Sergio, F.: Structure–Property Relation of Epoxy Resin with Fique fibers: Dynamic Behavior Using Split-Hopkinson Pressure Bar and Charpy Tests: Minerals, Metals and Materials Series. Springer, Cham (2019).

[9] Zhao, X., Wang, S.: Thermal, mechanical properties and morphology of epoxy resins modified with light pyrolysis natural rubber. wiley Periodicals (2017).

[10] Roberson, D., Perez, A.: Comparison of stress concentrator fabrication for 3D printed polymeric izod impact test specimens, Additive manufacturing Journal,1-11 (2015).

[11] Sabbagh, J., Leloup, G.: Dynamic and static moduli of elasticity of resin based materials. Dental Materials 18, 64-71, (2002).

[12] Whiting, R., Jacobsen, P.: Dynamic mechanical properties of resin-based filling materials. J Dent Res, 59(1), 55-60, (1980).

[13] Jager, S., Balthazard, R.: Dynamic thermo-mechanical properties of various flowable resin composites. J Clin Exp Dent, 8(5), 534–539 (2016).

[14] Marghalani, Y.: Resin-Based Dental Composite Materials. Springer, cham, (2016)

[15] Ferracane, L., Pfeifer, S.: Microstructural Features of Current Resin Composite Materials. Curr Oral Health Rep, 1: 205, (2014).

[16] Hong, H., Hu, M.: Dynamic Mechanical Behavior of Hierarchical Resin Honeycomb by 3D Printing, Polymers Journal, 13(1):19, (2021).

[17] Rua, J., Buchely, M.: Structure–Property Relation of Epoxy Resin with Fique Fibers: Dynamic Behavior Using Split-Hopkinson Pressure Bar and Charpy Tests,Green Materials Engineering. The Minerals, Metals & Materials Series, Springer, Cham (2019).

[18] Kolsky, H.: Stress waves in solids. Dover Books on Physics, New York (1963).

[19] Chen, W., Song, B.: Split Hopkinson bar, design, testing and application. Springer (2011).

[20] Owens, A., Tippu, H.: A tensile split Hopkinson bar for testing particulate polymer composite under elevated rates of loading. Exp. Mech. 49, 799–811, (2009).

[21] Weinberg, K., Khosravani, M., Thimm, B., Reppel, T., Bogunia, B., Aghayan, S., Nötzel, R.: Hopkinson-Bar experiments as a method to determine impact properties of brittle and ductile materials. *GAMM-Mitteilungen* 41 (2): 1-15 (2018).

[22] Weinberg, K., Khosravani, M.: On the tensile resistance of UHPC at impact. Eur. Phys. J. Spec. Top. 227:167-177, (2018).

[23] Hopkinson, B.: A method of measuring the pressure produced in the detonation of high explosives or by the impact of bullets. in Proceedings of the Royal Society of London, pp. 437–456, (1914).

[24] Chen, W., Zhou, B.: Constitutive Behavior of Epon 828/T-403 at Various Strain Rates. Mechanics of Time-Dependent Materials 2, 103–111 (1998).

[25] Zhao, J., Knauss, W.: Applicability of the time–temperature superposition principle in modeling dynamic response of a polyurea. Mech Time-Depend Mater 11, 289–308 (2007).

[26] Abaqus Standard user manual, Dessault Systems, (2019).

[27] Hong, Y., Sarntinoranont, M.: Localized Tissue Surrogate Deformation due to Controlled Single Bubble Cavitation.J Experimental Mechanics.56:97–109 (2016)

[28] Kang, W., Raphael, M.: Acceleration-induced pressure gradients and cavitation in soft biomaterials. Sci Rep 8, 15840 (2018).

[29] Hopfes, T., Wang, Z.: Collapse dynamics of bubble pairs in gelatinous fluids. Elsevier. Experimental Thermal and Fluid Science J (2019).

[30] Shahab, S., Kasra, M.: Design and construction of a novel measurement device for mechanical characterization of hydrogels: A case study. J Plos One (2021).

[31] Salati, M., Khazai, J.: Agarose-Based Biomaterials: Opportunities and Challenges in Cartilage Tissue Engineering. Polymers J (2020).

[32] Veroni, E., Tschon, M.: Agarose Gel as Biomaterial or Scaffold for Implantation Surgery: Characterization, Histological and Histomorphometric Study on Soft Tissue Response. Connective Tissue Research J (2012).

[33] Lake, S., Hald, E.: Collagen-agarose co-gels as a model for collagen-matrix interaction in soft tissues subjected to indentation. J Biomed Mater Res A (2011).

[34] El Sayed, T., Mota, A.: Biomechanics of traumatic brain injury. ElsevierJ, Comput. Methods Appl. Mech. Engrg (2008).

[35] Bigle, E.: Volumetric MRI Findings in Mild Traumatic Brain Injury (mTBI) and Neuropsychological Outcome. Springer. Neuropsychol Rev (2021).

[36] Wardlaw, A., Goeller, J.: Cavitation as a Possible Traumatic Brain Injury (TBI) Damage Mechanism. IFMBE proceedings 32:34-37 (2010).

[37] Adhikari, U., Goliaei, A.: Nanobubbles, cavitation, shock waves and traumatic brain injury. J Phys. Chem. Chem. Phys (2016).

[38] Marsh, J., Bentil, S.: Cerebrospinal Fluid Cavitation as a Mechanism of Blast-Induced Traumatic Brain Injury: A Review of Current Debates, Methods, and Findings. Frontiers in Neurology J (2021).

[39] Rutter, B., Song, H.: Shock Wave Physics as Related to Primary Non-Impact Blast-Induced Traumatic Brain Injury, Military Medicine J, 601–609 (2021).

[40] Sankin, G., Teslenko, V.: Two-threshold cavitation regime. Dokl. Phys. 48, 665–668 (2003).

[41] Brennen, C.: Cavitation in medicine. Interface Focus J (2015).

[42] Pishchalnikov, Y., Sapozhnikov, O.: Cavitation Bubble Cluster Activity in the Breakage of Kidney Stones by Lithotripter Shock Waves. J Endourol (2003).

[43] Kerstin Weinberg, Michael Ortiz. Kidney damage in extracorporeal shock wave lithotripsy: a numerical approach for different shock profiles. *Biomechanics and Modeling in Mechanobiology*, 8(4):285–299, (2009).

[44] Wolfrum, B.: Cavitation and shock wave effects on .biological systems. Doctral dissertation. University of Gottingen (2004).

[45] A. Vogel, W. Hentschel, J. Hozfuss.: Cavitation bubble dynamics and acoustic transient generation in ocular surgery with pulsed Neodymium:YAG lasers. Ophthalmology, 93 (1986).

[46] Dimitriadis, E., Horkay, F.: Determination of elastic moduli of thin layers of soft material using the atomic force microscope. Biophys J 82, 2798–2810 (2002).

[47] Raub, C., Putnam, A.: Predicting bulk mechanical properties of cellularized collagen gels using multiphoton microscopy. Acta Biomater 6, 4657–4665 (2010).

[48] Moreno-Arotzena, O., Meier, J.: Characterization of Fibrin and Collagen Gels for Engineering Wound Healing Models. J Materials 8, 1636–1651 (2015).

[49] Kang, W., Chen, Y.: Characterization and detection of acceleration-induced cavitation in soft materials using a drop-tower-based integrated system. Rev Sci Instrum 88 (2017).

[50] Zimberlin, J., Sanabria-DeLong, N.: Cavitation rheology for soft materials. J Soft Matter 3, 763–767(2007).

[51] Kundu, S., Crosby, A.: Cavitation and fracture behavior of polyacrylamide hydrogels. J Soft Matter 5, 3963–3968 (2009).

[52] Gaudron, R., Warnez, M.: Bubble dynamics in a viscoelastic medium with nonlinear elasticity. J Fluid Mech. 766 (2015).

[53] Estrada, J., Barajas, C.: High strain-rate soft material characterization via inertial cavitation. J Mech Phys Solids 112, 291–317 (2018).

[54] Kang, W., Adnan, A.: Cavitation nucleation in gelatin: Experiment and mechanism. Acta Biomater(2017).

[55] Normand, V., Lootens, D.: New insight into agarose gel mechanical properties. J Biomacromolecules 1, 730–738 (2000).

[56] Kwon, J., Subhash, G.: Compressive strain rate sensitivity of ballistic gelatin. J Biomech 43, 420–425 (2010).

[57] Soza, G.: Determination of the elasticity parameters of brain tissue with combined simulation and registration. Int J Med Robot1, 87–95 (2005).

[58] Budday, S., Nay, R.: Mechanical properties of gray and white matter brain tissue by indentation. J Mech Behav Biomed 46, 318–330 (2015).

[59] Gozna, E., Marble, A.: Mechanical properties of the ascending thoracic aorta of man. Cardiovasc Res 7, 261–265 (1973).

[60] Sinibaldi, G., Occhicone, A.: Laser induced cavitation: Plasma generation and breakdown shockwave. J Physics of Fluids 31, 103302 (2019).

[61] Ohl, S., Klaseboer, E.: Bubbles with shock waves and ultrasound: a review. Interface Focus Vol. 5,5 (2015).

[62] Maimbourg, G., Houdouin, A.: Inside/outside the brain binary cavitation localization based on the lowpass filter effect of the skull on the harmonic content. Physics in Medicine and Biology J (2018).

[63] Arvanitis, C., Clement, G.: Transcranial Assessment and Visualization of Acoustic Cavitation: Modeling and Experimental Validation. IEEE Trans Med Imaging (2016).

[64] Miansari, M., Mehta, M.: Inducing Mild Traumatic Brain Injury in C. elegans via Cavitation-Free Surface Acoustic Wave-Driven Ultrasonic Irradiation. Scientific Reports J (2019).

[65] Bustamante, M., Singh, D.: Polymeric Hopkinson Bar-Confinement Chamber Apparatus to Evaluate Fluid Cavitation. Experimental Mechanics J (2018).

[66] Valtorta, D., Mazza, E.: Dynamic measurement of soft tissue viscoelastic properties with a torsional resonator device. J Med. Image Anal. 9, 481–490 (2005).

[67] Domke, J., Radmacher, M.: Measuring the Elastic Properties of Thin Polymer Films with the Atomic Force Microscope. J Langmuir 14, 3320–3325 (1998).

[68] Lauterborn, W.: High-speed photography of laser-induced breakdown in liquids. Appl. Phys. Lett., 21 (1972).

[69] Vogel, A., Lauterborn, W.: Time-resolved particle image velocimetry used in the investigation of cavitation bubble dynamics. Appl. Optics, 29 (1988).

[70] Vogel, A., Lauterborn, W: Optical and acoustic investigations of the dynamics of laser-produced cavitation bubbles near a solid boundary. J. Fluid Mech. 206 (1989).

[71] Philipp, A., Delius, M.: Interaction of lithotripter-generated shock waves with air bubbles. J. Acoust. Soc. Am., 93 (1993).

[72] Lauterborn, W., Kurz, T.: Experimental and theoretical bubble dynamics. Adv. Chem. Phys., 110 (1999).

[73] Aghayan, S., Bieler, S., Weinberg, K.: Determination of the high-strain rate elastic modulus of printing resins using two different split Hopkinson pressure bars. Mech Time-Depend Mater (2021).

[74] McNaught, A., Wilkinson, A.: IUPAC. Compendium of Chemical Terminology, 2nd ed. (the "Gold Book").Blackwell Scientific Publications, Oxford (1997).

[75] Polyvision Inc: https://www.polyvisions.com/polymer-resin/. Accessed 25.06.2022.

[76] Ko, D., Gyak, K.: Emerging Microreaction Systems Based on 3D Printing Techniques and Separation Technologies. Journal of Flow Chemistry. Volume 7: Issue 3-4 (2017).

[77] Takenaga, S.; Schneider, B.; Erbay, E.: Fabrication of biocompatible lab-on-chip devices for biomedical applications by means of a 3D-printing process. Phys. Status Solidi A (2015).

[78] Pham, T., Kim, P.: Three-Dimensional SiCN Ceramic Microstructures via Nano-Stereolithography of Inorganic Polymer Photoresists. Adv. Funct. Mater. 16, 1235–1241 (2016).

[79] Bauer, W.: Methacrylic Acid and Derivatives". Ullmann's Encyclopedia of Industrial Chemistry. Weinheim: Wiley-VCH (2002).

[80] Peters, E.: Plastics: Thermoplastics, Thermosets, and Elastomers. Handbook of Materials Selection, New York: John Wiley & Sons, Inc., pp. 363–365 (2006).

[81] Grote, D., Park, S.: Dynamic behavior of concrete at high strain rates and pressure: I. experimental characterization, Int. J. Impact Eng. 25 869–886 (2001).

[82] Owens, A,. Tippur, H.: tensile split Hopkinson bar for testing particulate polymer composite under elevated rates of loading, Exp. Mech. 49 799–811 (2009) .

[83] Zhu, W,. Niu, L.: Dynamic Brazilian test of rock under intermediate strain rate: Pendulum hammer-driven SHPB test and numerical simulation, Rock Mech.Rock Eng. 48 (2015) 1867–1881.

[84] Dai, F., Huang, S.: Some fundamental issues in dynamic compression and tension tests of rock using split Hopkinson pressure bar. Rock. Mech. Rock. Eng. 43, 657–666, (2010).

[85] Gorham, D.: Specimen inertia in high strain-rate compression. Journal of Physics D: Applied Physics 22 (12), (1989).

[86] Ravichandran, G., Subhash, G.: Critical appraisal of limiting strain rates for compression testing of ceramics in a Split Hopkinson pressure bar. J. Am. Ceram. Sco. 77, 263–267, (1994).

[87] Janiszewski,J., Buzantowicz, W.: Correction Procedure of Wave Signals for a Viscoelastic Split Hopkinson Pressure Bar. Problems of Mechatronics journal, 7, 1 (23), 17-30, (2016).

[88] Biler, S., Weinberg, K.: Signal corretion for testing soft materials in PMMA Split-Hopkinson pressure bars to be subm.

[89] Weinberg, K., Aghayan, S.: A variational model of bubble cavitation in soft gels and its experimental validation. submitted to Mechanics of Materials (2022).

[90] Jussila, J., Leppaniemi, A: Ballistic skin simulant. Forensic Sci Int 150, 63-71 (2005).

[91] Wen, Y., Xu, C.: Rie bullet penetration into ballistic gelatin. J Mech Behav Biomed 67,40-50 (2017).

[92] Riahi, R. Yang, Y.: Advances in wound-healing assays for probing collective cell migration. J Lab Autom. 59-65 (2012).

[93] Bryant, S,. Cuy, J.: Photo-patterning of porous hydrogels for tissue engineering. Biomaterials J. 2978-2986 (2006).

[94] Choi, J., Kang, D.: Thin, Soft, Skin-Mounted Microfluidic Networks with Capillary Bursting Valves for Chrono-Sampling of Sweat.J Adv. Healthcare Mater. 6 (2017).

[95] Di, J., Yao, S.: Stretch-Triggered Drug Delivery from Wearable Elastomer Films Containing Therapeutic Depots. ACS Nano 9, 9407-9415 (2015).

[96] Kang, W., Giraldo-Vela, J.: Microfluidic device for stem cell differentiation and localized electroporation of postmitotic neurons. J Lab on a Chip 14, 4486-4495 (2014).

[97] Nathamgari, S., Dong, B.: Isolating single cells in a neurosphere assay using inertial microfluidics. J Lab Chip 15, 4591-4597 (2015).

[98] Bilston, L.: Brain Tissue Mechanical Properties. Biomechanics of the Brain. Biological and Medical Physics, Biomedical Engineering. Springer (2011)

[99] Wardlaw, A., Goeller, J.: Cavitation as a Possible TBI Damage Mechanism. 26th Southern Biomedical Engineering Conference SBEC. IFMBE proceedings (2010).

[100] Blausen Medical: https://blausen.com/pages/sitesecurityaccess.aspx. Accessed 25.05.2022.

[101] Purves, D.: Neuroscience (5th ed.). Sunderland, MA: Sinauer associates.P 742 (2012).

[102] Adams, J,. Graham, D.: Diffuse brain damages in non-missile head injury, in: Recent Advances in Histopathology (1984).

[103] Perles, S., Rewcastle, N.: Shear injuries of the brain, Can. Med. Assoc. J. 96. 577–582 (1967).

[104] Strich, S.: Diffuse degeneration of cerebral white matter in severe dementia following head injury, J. Neurol. Neurosurg. Psychiatry 19. 163–185 (1956).

[105] Hoffman, A.: Hydrogels for biomedical applications. Ann N Y Acad Sci. 944:62–73 (2001).

[106] Peppas, N., Bures, P., Leobandung, W.: Hydrogels in pharmaceutical formulations. Eur J Pharm Biopharm. 50:27–46 (2000).

[107] Zhu, J.: Design properties of hydrogel tissue-engineering scaffolds. Expert Rev Med Devices.;8(5):607-626 (2011).

[108] Ifkovits, J., Burdick, J.: photopolymerizable and degradable biomaterials for tissue engineering applications. Review, Tissue Eng.13(10):2369–2385 (2007).

[109] Nguyen, T., West, J.: Photopolymerizable hydrogels for tissue engineering applications. Biomaterials. 23(22):4307–4314 (2002).

[110] El-Sherbiny, I., Yacoub, M.: Hydrogel scaffolds for tissue engineering: Progress and challenges. Glob Cardiol Sci Pract. 2013(3):316-342 (2013).

[111] Guenet, J.: Thermoreversible gelation of polymers and biopolymers. New York: Academic Press (1992).

[112] Zhu, J.: Bioactive modification of poly(ethylene glycol) hydrogels for tissue engineering. Biomaterials. 31(17):4639–4656 (2010).

[113] Geckil, H., Xu, F.: Engineering hydrogels as extracellular matrix mimics. Nanomedicine. 5(3):469–484 (2010).

[114] Hunt, N., Grover, L.: Cell encapsulation using biopolymer gels for regenerative medicine. Biotechnol Lett. 32(6):733–742 (2010).

[115] Schneide, G., English, A,.:. The effect of hydrogel charge density on cell attachment. Biomaterials. 25(15):3023–3028 (2004).

[116] Hejcl, A., Sedy, J.: HPMA-RGD hydrogels seeded with mesenchymal stem cells improve functional outcome in chronic spinal cord injury. Stem Cells Delvelop 19(10) 1535–1546 (2010).

[117] Woerly, S., Pinet, E.: Spinal cord repair with PHPMA hydrogel containing RGD peptide (NeuroGel) Biomaterials.22(10):1095–1111 (2001).

[118] Sawhney, A., Pathak, C.: Bioerodible hydrogels based on photopolymerized poly(ethylene glycol)-co-poly(α-hydroxy acid) diacrylate macromers. Macromolecules. 26(4) 581–587 (1993).

[119] Clapper, J., Skeie, J.: Development and characterization of photopolymerizable biodegradable materials from PEG–PLA–PEG block macromonomers. Polymer.48(22) 6554–6564 (2007).

[120] Hern, D., Hubbell, J.: Incorporation of adhesion peptides into nonadhesive hydrogels useful for tissue resurfacing. J Biomed Mater Res. 39(2) 266–276 (1998).

[121] Lutolf, M., Hubbell, J.: Synthetic biomaterials as instructive extracellular microenvironments for morphogenesis in tissue engineering. Nat Biotechnol. 23(1):47–55 (2005).

[122] Ma, P.: Biomimetic materials for tissue engineering. Adv Drug Deliver Rev. 60(2) 184–198 (2008).

[123] Chen, R., Hunt, J.: Biomimetic materials processing for tissue-engineering processes. J Mater Chem. 17(38) 3974–3979 (2007).

[124] Besant, W.: Hydrostatics and Hydrodynamics. Deighton Bell, Cambridge (1859).

[125] Castro, A.: Lagrangian tracking of the cavitaion bubble. Dissertation. Brno University of Technology (2019)

[126] Keller, J., Miksis, M.: Bubble oscillations of large amplitude. J. Acoust. Soc. Am.68 628-633 (1980).

[127] Wu, C., Roberts, P.: Shock-wave propagation in a sonoluminescing gas bubble. Phys. Rev. Lett. 70, 3424-3427 (1993).

[128] Vuong, V., Szeri, A.: Sonoluminescence and di®usive transport. Physics of Fluids, 8 2354-2364 (1996).

[129] Lohse, D., Brenner, M.: Sonoluminescing air bubbles rectify argon. Phys. Rev. Lett., 78 1359-1362 (1997).

[130] Yasui, K.: Alternative model of single-bubble sonoluminescence. Phys. Rev. E, 56. 6750-6760 (1997).

[131] Herring, C.: Theory of the pulsations of the gas bubble produced by an underwater explosion. Underwater explosion research (1949).

[132] Gilmore, F.: The growth or collapse of a spherical bubble in a viscous compressible liquid. California Institute of Tech Engineering Report No. 26-4 26, 4, 1–40 (1952).

[133] Voss, M.: Numerische, theoretische und experimentelle Untersuchungen zur Kavitationsblasendynamik. Dissertation, Georg-August-UniversitÄat zu Gaottingen, (2002).

[134] Doinikov, A., Boukaz, A.: Review of shell models for contrast agent microbubbles," IEEE Trans. Ultrason. Ferroelectr. Freq. Control 58(5), 981–993 (2011).

[135] Mehrem, A.: Theoretical study of the microbubble dynamics under the action of ultrasound fields. Dissertation. Univertisy of Valencia (2013).

[136] Gaudron, R., Warnez, M.: Bubble dynamics in a viscoelastic medium with nonlinear elasticity. J Fluid Mech. 766 (2015).

[137] Fu, Y., Haotian, L.: Size-dependent inertial cavitation of soft materia. Elsevier. Journal of the Mechanics and Physics of Solids (2020).

[138] C. Truesdell and W Noll. *The Non-Linear Field Theories of Mechanics. In Flügge, S.: Handbuch der Physik. Volume III/3.* Springer-Verlag, Berlin, (1965).

[139] J. M. Ball. Discontinuous equilibrium solutions and cavitation in nonlinear elasticity. *Philosophical Transactions of the Royal Society of London. Series A, Mathematical and Physical Sciences*, 306:557 – 611, 1982.

[140] Weinberg, K., Bohme, T.: Condensation and Growth of Kirkendall Voids in Intermetallic Compounds: Components and Packaging Technologies. IEEE Transactions on Components and Packaging Technologies (2009).

[141] Aghayan, S., Weinberg, K.: Experimental and numerical investigation of dynamic cavitation in agarose gel as a soft tissue simulant. *Mechanics of Materials, to appear*, (2022).

[142] Aghayan, S., Weinberg, K., Marvi-Mashhadi, M.: Numerical investigations on the volume-pressure gradient of acceleration-induced cavitation in soft agarose gel. in preparation

[143] Chesterman, W.: The dynamics of small transient cavities. Proc Phys Soc 65. 846–858 (1952) .

[144] Hansson, I., Kedrinskii, V.: On the dynamics of cavity clusters. J Phys D Appl Phys 15. 1725–1734 (1982).

[145] Overton, G., Williams, P.: The influence of cavitation history and entrained gas on liquid tensile strength. J Phys D Appl Phys 17.979–987 (1984).

[146] Sekisui Alveo AG, Switzerland, Product catalogue PSS version9/00/HH/FA.https://www.sekisuialveo.com/en/company (2020).

[147] Williams, P., Williams, P.: Pressure–tension cycles induced by dynamic stressing and cavitation in liquids. J Phys D Appl Phys 29.1904–1909 (1996).

[148] Trevena, D.: Cavitation and the generation of tension in liquids. J Phys D Appl Phys 17.2139–2164 (1984).

[149] Couzens, D., Trevena, D.: Tensile failure of liquids under dynamic stressing. J Phys D Appl Phys 7.2277–2287 (1974).

[150] Sedgewick, S., Trevena, D.: Limiting negative pressure of water under dynamic stressing. J Phys D Appl Phys 9.1983–1190 (1976).

[151] Kenner, V.: The propagation of compressive and tensile waves in a fluid column. Int J Mech Sci 20.373–383 (1978).

[152] Rasband, W.S., ImageJ, U. S. National Institutes of Health, Bethesda, Maryland, USA, https://imagej.nih.gov/ij/, 1997-2018.

[153] Weinberg, K., Bohme, T.: Mesoscopic Modeling for Continua with Pores: Application in Biological Soft Tissue. Journal of Non-Equilibrium Thermodynamics (2008).

[154] Kim, C., Choi, W.: Cavitation nucleation and its ductile-to-brittle shape transition in soft gels under translational mechanical impact. Acta Biomaterialia Journal, 160-173 (2022).

[155] Ushikubo, F., Furukawa, T.: Evidence of the existence and the stability of nanobubbles in water. J Colloid Surface A 361, 31–37 (2010).

[156] Wilson, C., Hall, T.: Comparative study of the dynamics of laser and acoustically generated bubbles in viscoelastic media. Phys. Rev. E 99 (2019).

[157] Rodriguez-Perez, M., Hidalgo, F. Measuring the time evolution of the gas pressure in closed cell polyolefin foams produced by compression moulding Polymer testing (2009).

List of Figures

List of Tables